2012

Terahertz Imaging for Cancer Detection

Benjamin A. St. Peter
University of Massachusetts Amherst

TERAHERTZ IMAGING FOR CANCER DETECTION

A Thesis Presented

by

BENJAMIN ST. PETER

Submitted to the Graduate School of the
University of Massachusetts Amherst in partial fulfillment
of the requirements for the degree of

MASTER OF SCIENCE IN ELECTRICAL AND COMPUTER ENGINEERING

September 2012

Electrical and Computer Engineering

TERAHERTZ IMAGING FOR CANCER DETECTION

A Thesis Presented

by

BENJAMIN ST. PETER

Approved as to style and content by:

Sigfrid Yngvesson, Advisor

Paul Siqueira, Advisor

Christopher Salthouse, Member

Christopher V. Hollot, Department Chair
Electrical and Computer Engineering

To the art of knowing when to persist

ACKNOWLEDGMENTS

This project would not have been possible without funding from The National Institutes of Health and the National Cancer Institute (1R21CA143660-01A1).

Many thanks to my committee members, Drs. Yngvesson, Siqueira, and Salthouse. My advisor, Dr. Siqueira, has helped me in myriad ways since my arrival at UMass. I'd like to give special thanks to Dr. Yngvesson, the leader of this project, whose knowledge and patient guidance have made me a better engineer and maybe even a better person. Also, thanks to Dr. Patrick Kelly for our long discussions during weekly radiometry meetings.

Thanks to our collaborators at The University of Massachusetts Medical School and especially to Dr. Ashraf Khan in the pathology department.

Thanks to the students and recent graduates who helped in various ways with this project: Martin Muthee, Tomas Broka, Ric Zannoni, Enrique Carrion, and Jorge Salazar.

ABSTRACT

This project evaluates the ability of terahertz (THz) radiation to differentiate cancerous from non-cancerous human breast lumpectomy and mastectomy tissue. This is done by aiming a narrow-band THz beam at medical samples and measuring reflected power. THz images of specimens from Breast Conservation Surgery (BCS) were created using a gas laser source and mechanical scanning. The design and characterization of this system is discussed in detail. The images were correlated with optical histological micrographs of the same specimens and discrimination values of more than 70% were found for five of the six samples using Receiver Operating Characteristic (ROC) analysis.

TABLE OF CONTENTS

Page

ACKNOWLEDGMENTS . . . . . **iv**

ABSTRACT . . . . . **v**

LIST OF TABLES . . . . . **ix**

CHAPTER

1. INTRODUCTION **1**

2. MEASUREMENT APPARATUS **3**

2.1 Laser Source and Modulator 3
2.2 Beam Splitter 4
2.3 Focusing Elements 7

2.3.1 Initial Design using the Gaussian Beam Telescope Method 7
2.3.2 Evaluation using Ray Transfer Matrices 11

2.4 Sample Cover 15

2.4.1 Mylar 15
2.4.2 Quartz of 1.9113mm 16
2.4.3 Quartz of 0.475mm 22
2.4.4 Quartz of Random Thickness 22

2.5 Sample Holder 24

2.5.1 Machined Acrylic 24
2.5.2 Design with a Calibration Basin 25

2.6 Detectors 26

2.6.1 Pyroelectric Detector 26
2.6.2 Bolometer 27

2.7 Lock-In Amplifiers and Data Capture . . . 28
2.7.1 Discrete-Position Measurements . . . 28
2.7.2 Continuous-Velocity Measurements . . . 32
2.8 Calibration . . . 33
2.8.1 Dual Detector Method . . . 33
2.8.2 Ethanol Solution Method . . . 36
2.9 Resolution . . . 38
2.10 Post-Processing . . . 44
2.10.1 Technique and Calculations . . . 44
2.10.2 Animation . . . 49
3. SPECIAL TOPICS . . . 50
3.1 Quartz Thickness from Transmission Measurements . . . 50
3.1.1 RIKEN Quartz . . . 50
3.1.2 Quartz of 0.475mm . . . 52
3.1.3 Quartz of 1.9113mm . . . 55
3.2 Attenuation Constants from Transmission Measurements . . . 56
3.3 Logistics and Practical Medical Sample Concerns . . . 61
3.4 Surface Roughness Compensation . . . 63
4. RESULTS . . . 66
4.1 Non-Medical Samples and Phantoms . . . 66
4.2 Individual Medical Sample Results . . . 67
4.2.1 Sample 2B . . . 68
4.2.2 Sample 7A . . . 69
4.2.3 Sample 8A . . . 73
4.2.4 Sample 9A . . . 76
4.2.5 Sample 10A . . . 79
4.2.6 Sample 11A . . . 82
4.2.7 Sample 12A . . . 85
4.3 Combined Medical Sample Results . . . 88
5. CONCLUSIONS . . . 91
5.1 Contributions of this Project . . . 91
5.2 Evaluation of System Capability . . . 91

5.3 Future Work Suggestions 93

APPENDICES

A. MECHANICAL DEFLECTION OF THE SAMPLE COVER 95
B. PRELIMINARY SIMULATOR 96
C. REFRACTIVE INDEX DISTRIBUTIONS 98
D. HISTOLOGY SLIDES 102

BIBLIOGRAPHY 115

LIST OF TABLES

Table **Page**

2.1 Details of Focusing Element Layout 10

2.2 Quartz Properties for Schematic Model 19

2.3 Refractive Index and Power Reflectivity by Calibration Fluid and Tissue Type 37

3.1 Surface Roughness by Grit 64

4.1 Mean Values of Cancerous and Non-Cancerous Pixel Refractive Indices 90

5.1 ROC Discrimination 92

CHAPTER 1

INTRODUCTION

This project evaluates the ability of terahertz (THz) radiation to differentiate cancerous from non-cancerous human breast lumpectomy and mastectomy tissue. This is done by aiming a narrow-band THz beam at medical samples and measuring reflected power. Cancerous regions are more reflective, possibly because they contain more water. As shown in Table 2.3, there was already evidence that different tissue types reflect different amounts of THz power.

Our work is funded by the National Institutes of Health (1R21CA143660-01A1) and is in collaboration with The University of Massachusetts Medical School in Worcester. The goal of the NIH proposal was to design and use a prototype THz device to assess excised samples after Breast Conservation Surgery (BCS). In BCS, surgeons remove tissue until surfaces of excised flesh appear not to contain cancer. Afterward, if histologists do not find a margin of healthy tissue around the excised samples, a repeat surgery is necessary. More than 20% of procedures leave positive margins which require repeat surgeries [Jac08]. An operating room device for quick assessment of tissue margins would reduce the number of operations while enabling surgeons to be more conservative with excisions.

THz has advantages over X-rays because it is non-ionizing and, as determined with Time Domain Spectroscopy (TDS), has greater contrast between tissue types [PMLF$^+$07]. Non-ionizing radiation is favorable because it does not have enough energy to dam-

age molecules in living cells by removing electrons. Imaging with a narrow-band THz source, sometimes known as Frequency Domain THz Imaging (FDTI), has an advantage over TDS because forthcoming generations of FDTI cameras could use technologies such as those described by Öjefors et al. to be compact enough for practical operating room use [OPLR09].

Terahertz imaging has potential for the detection of breast cancer and also skin, cervical, and colon cancers [CFSPM12]. Research has been done with THz pulsed imaging using commercially available time domain systems, including application of techniques from taking a ratio of two points on the time-domain response [FWJL$^+$06] to using support vector machines (SVM) and principal component analysis (PCA) [FPP$^+$12]. However, THz imaging performance lags behind other imaging modalities such as MRI, Raman spectroscopy, and confocal microscopy. It is thought that combining THz imaging with other imaging techniques might make it a competitive tool to aide in cancer diagnosis. A example of this, albeit at optical frequencies, is the work of Patel et al., which combines dye-enhanced macroscopic polarization imaging with multimodal confocal microscopy for the detection of breast cancer [PKW$^+$12].

CHAPTER 2

MEASUREMENT APPARATUS

The apparatus consists primarily of a THz laser source and a series of optical elements for focusing the beam onto a sample and then focusing the reflected beam onto a detector. A computer records detector output while positioning the sample with two motorized platforms. Images are created by calculating refractive index based on reflected power and mapping it to a color scale.

2.1 Laser Source and Modulator

THz radiation is in the far infrared (FIR) region and may be generated with a laser system. The system available to this project was originally constructed for radio astronomy at the South Pole [GYN+03]. It is a cascade of two lasers which is capable of operation at one of many frequencies, depending on gas selection and adjustment of laser tube lengths. The output of a CO_2 laser enters an FIR laser tube which contains difluoromethane gas. The wavelength of the CO_2 laser is approximately 10μm and the power is 30W. The combination of approximately 85mTorr difluoromethane with 9P10 tuning of the CO_2 laser creates a 650μW beam with a frequency of 1.8912743THz[Dou89] and polarization perpendicular to the optics table. Proximate verification of that frequency was made with a Michelson interferometer. Polarization was tested by rotating a grating of thin and uniformly-aligned wires until the beam was most severely attenuated.

The FIR laser is modulated by diverting the CO_2 beam path with an acousto-optic

modulator (AOM). This type of modulator works by allowing the compression and rarefaction of sound waves to effectively change refractive index within a transparent material. It may be operated as a Raman-Nath device, which has many diffracted orders, or as a Bragg device, which concentrates most of the power into the zeroth and first orders. The Bragg configuration is preferred for application as a modulation switch and is achieved when $L < \Lambda^2/\lambda$, where L is the interaction length between the laser beam and sound field, Λ is the sound wavelength, and λ is the laser wavelength [Int]. For maximum efficiency of a Bragg device, the incident laser beam must make an angle of incidence with the sound field of $\theta_B = \lambda/(2\Lambda)$. It is best to use the first-order diffraction beam, which, unlike the zeroth-order beam, allows none of the laser to pass when no sound wave is applied.

2.2 Beam Splitter

The laser beam was made normal to the sample in consideration of potential future in-vivo applications and for avoidance of birefringence effects in the crystal sample cover. Since incident and reflected beams occupy the same space, normal incidence requires a beam splitter. Our beam splitter is oriented at 45 degrees and is made of 25μm Mylar, which has a refractive index of 1.79 [Zha05].

As shown in Figure 2.4 on page 10, the beam is reflected by the beam splitter, reflected by the sample, then transmitted through the beam splitter on its way to the detector. Minimization of beam splitter losses therefore becomes maximization of $A * B$, such that $A = (1 - B)$, where A and B are reflected and transmitted power. The solution is $A = B$ for a best possible efficiency of 25%.

The two air/surface boundaries of the Mylar sheet may be considered as an etalon,

which is two parallel reflective surfaces that create an interferometric effect by trapping radiation.

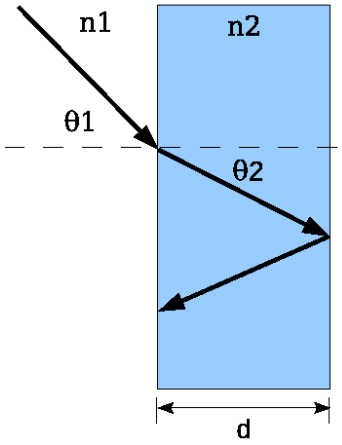

Figure 2.1: Fabry-Pérot Etalon

The transmission coefficient, T, was calculated as follows, where F is the coefficient of finesse – a measure of the peakedness of transmission as a function of wavelength (analogous to Q-factor in the field of electronics) [Gol98]:

$$T = \left[1 + F \sin^2\left(\frac{\phi}{2}\right)\right]^{-1}, \tag{2.1}$$

$$F = \frac{4|\Gamma|^2}{(1 - |\Gamma|^2)^2}. \tag{2.2}$$

Equations 2.1 and 2.2 were derived using an infinite series to account for multiple reflections. Fresnel's equation was used to determine the reflection coefficient for Equation 2.2, where θ and n are the angles and refractive indices as labeled in Figure 2.1:

$$\Gamma_\perp = \left|\frac{n_1 \cos\theta_1 - n_2 \cos\theta_2}{n_1 \cos\theta_1 + n_2 \cos\theta_2}\right|. \tag{2.3}$$

In Equation 2.1, ϕ represents the phase difference between successive surface reflections.

$$\phi = \phi_2 - \phi_1, \tag{2.4}$$

where ϕ_2 accounts for phase lag in the n_2 material between entry and exit points and ϕ_1 accounts for the phase lead necessary before incoming and outgoing beams are aligned to interfere.

$$\phi_2 = k_2 \cdot RPL, \tag{2.5}$$

where k_2 is the wavenumber $(2\pi n_2/\lambda_0)$ and RPL is return path length, which is the sum of the magnitudes of the two vectors in the n_2 material. ϕ_2 can be expanded by applying trigonometry to Figure 2.1:

$$\phi_2 = \left(\frac{2\pi n_2}{\lambda_0}\right)\frac{2d}{\cos\theta_2}. \tag{2.6}$$

ϕ_1 is zero if the beam is normally incident upon the n_2 material. Otherwise, it is the wavenumber multiplied by the distance between the beam entry and exit points shown in Figure 2.1, multiplied by $\sin\theta_1$:

$$\phi_1 = \frac{2\pi n_1}{\lambda_0}(2d\tan\theta_2)\sin\theta_1. \tag{2.7}$$

Snell's Law may be used to account for refraction and express θ_1 in terms of θ_2 or vice versa:

$$\frac{\sin\theta_1}{\sin\theta_2} = \frac{n_2}{n_1}. \tag{2.8}$$

Defining n_1 as the refractive index of free space ($n_1 = 1$), equations 2.4, 2.6, 2.7, and 2.8 may be combined for a refined expression of phase difference:

$$\phi = \left(\frac{4\pi d}{\lambda_0}\right)\sqrt{{n_2}^2 - \sin^2\theta_1}. \tag{2.9}$$

Figure 2.2 shows that T is 73% when 25μm Mylar is used to make a beam splitter oriented at 45 degrees. The efficiency is then $73\%(1 - 73\%) = 19.7\%$ as opposed to the optimal value of 25% as discussed above. The figure shows that increasing θ_1 could provide a transmission coefficient closer to the 50% target.

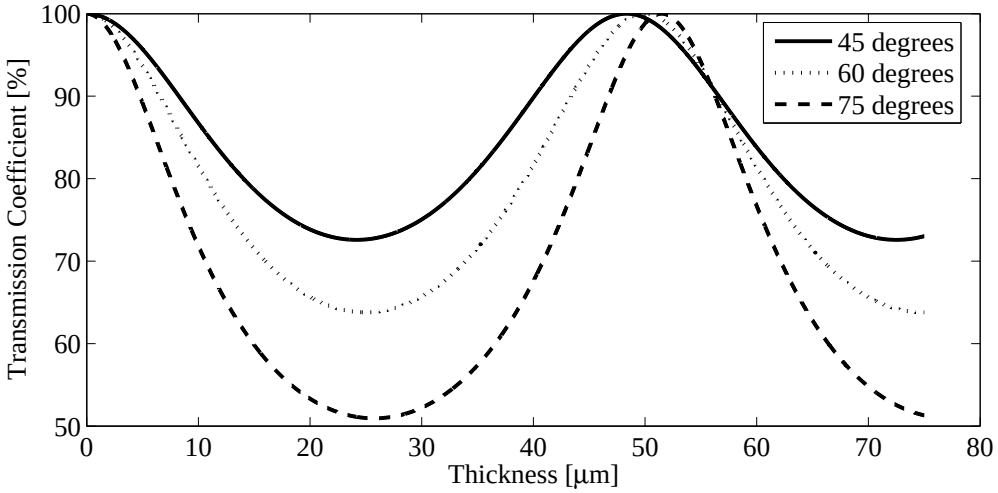

Figure 2.2: Etalon or Fabry-Pérot Effect of the Mylar Beam Splitter at 1.89THz

The reason for the periodic dips in Figure 2.2 is that maximum reflection occurs when there is maximum constructive interference at the material boundary between n_1 and n_2, which is when phase difference corresponds to $\lambda/2 + N\lambda$. The first minimum will therefore occur when ϕ equals π. Equation 2.9 can be rearranged to solve for d, producing a value which can be verified against the figure:

$$d = \phi \left(\frac{\lambda_0}{4\pi}\right) \frac{1}{\sqrt{{n_2}^2 - \sin^2\theta_1}} = \pi \left(\frac{159\mu\text{m}}{4\pi}\right) \frac{1}{\sqrt{1.79^2 - \sin^2\frac{\pi}{4}}} = 24.2\mu\text{m}. \qquad (2.10)$$

2.3 Focusing Elements

The layout of focusing elements was designed in the same way that Gaussian beam telescopes are designed. To do this, mirrors were regarded as lenses of infinitesimal thickness. The design was evaluated using ray transfer matrices.

2.3.1 Initial Design using the Gaussian Beam Telescope Method

A Gaussian beam telescope is a telescope in which the sum of the focal lengths between any two focusing elements is equal to the distance between those elements

[Gol98]. The utility of such a system is made clear with a derivation of back focal length (BFL).

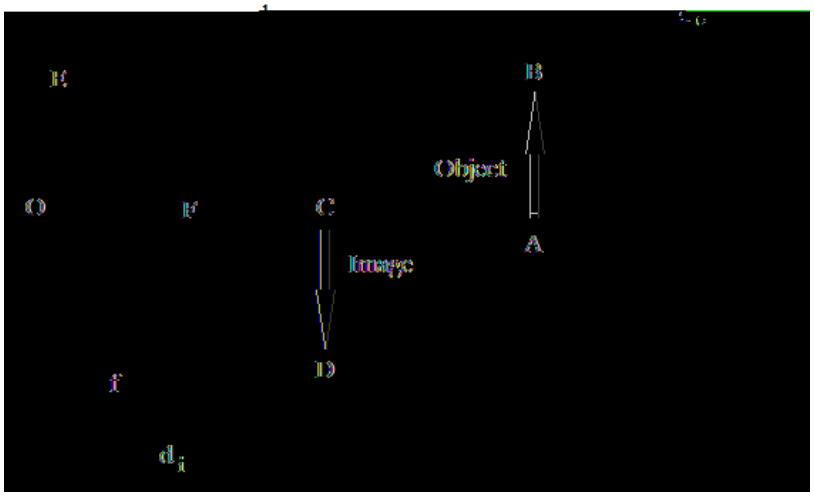

Figure 2.3: Basic Lens Scenario

In Figure 2.3, OFE and CFD are similar triangles by the angle-angle rule. Side ratios of those similar triangles are equal and may be expressed in terms of image distance and focal length:

$$\frac{\text{CD}}{\text{OE}} = \frac{\text{CF}}{\text{OF}} = \frac{d_\text{i} - f}{f}. \tag{2.11}$$

AOB and COD are also similar angles by the angle-angle rule. Side ratios are then equal to a ratio of image distance to object distance:

$$\frac{\text{CD}}{\text{AB}} = \frac{\text{CO}}{\text{AO}} = \frac{d_\text{i}}{d_\text{o}}. \tag{2.12}$$

Because EB is parallel to OA, we know AB=OE. Equations 2.11 and 2.12 may be combined to create an equation relating f, d_o, and d_i:

$$\frac{\text{CD}}{\text{AB}} = \frac{d_\text{i} - f}{f} = \frac{d_\text{i}}{d_\text{o}}, \tag{2.13}$$

$$\frac{1}{f} = \frac{1}{d_\text{o}} + \frac{1}{d_\text{i}}. \tag{2.14}$$

Because there was no accounting for the effects of light passing through lens material beyond that of ideal focusing behavior, it may be said that the equation is valid only for infinitesimally thin lenses. In fact, Equation 2.14 is commonly known as the Thin Lens Formula.

Supposing an arrangement of 2 lenses, the distance between the 2nd lens and the focal point between those lenses would be the distance between lenses minus the focal length of the first lens. That distance can replace d_{o} in a Thin Lens Formula treatment of the 2nd lens:

$$\frac{1}{f_2} = \frac{1}{d_{\mathrm{between}} - f_1} + \frac{1}{d_{\mathrm{i}}}. \tag{2.15}$$

d_{i} now corresponds to the distance from the second lens to the focal point of the lens combination. This is commonly known as back focal length (BFL):

$$\mathrm{BFL} = \frac{f_2(d_{\mathrm{between}} - f_1)}{d_{\mathrm{between}} - (f_1 + f_2)}. \tag{2.16}$$

Here it can be seen that BFL is infinite if the sum of focal lengths is equal to the distance between lenses. Such setups are afocal and sometimes referred-to as Gaussian beam telescopes or Newtonian telescopes [Sie86]. Following this rule vastly simplified design because knowing focal points only required consideration of the previous element.

A basic representation of the final design is shown in Figure 2.4, where non-focusing flat mirrors are unlabeled. Although this design began with the Gaussian beam telescope concept, small adjustments have been made such that the distance between elements is not always equal to the sum of their focal lengths. Elements m_1 through

m_5 are curved mirrors with specifications given in Table 2.1. A photograph is provided in Figure 2.5.

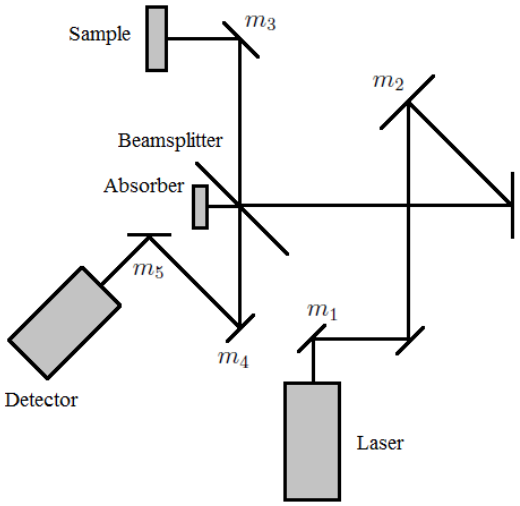

Figure 2.4: Focusing Element Layout

Label	Position [mm]	Focal Length [mm]	Description
m_1	75	75	Off-Axis Paraboloidal Mirror
m_2	912	762	Spherical Mirror
m_3	1674	89	Off-Axis Paraboloidal Mirror
	1763		Sample
m_3	1852	89	Off-Axis Paraboloidal Mirror
m_4	2267	326	Off-Axis Paraboloidal Mirror
m_5	2450	75	Off-Axis Paraboloidal Mirror
	2500		Detector

Table 2.1: Details of Focusing Element Layout

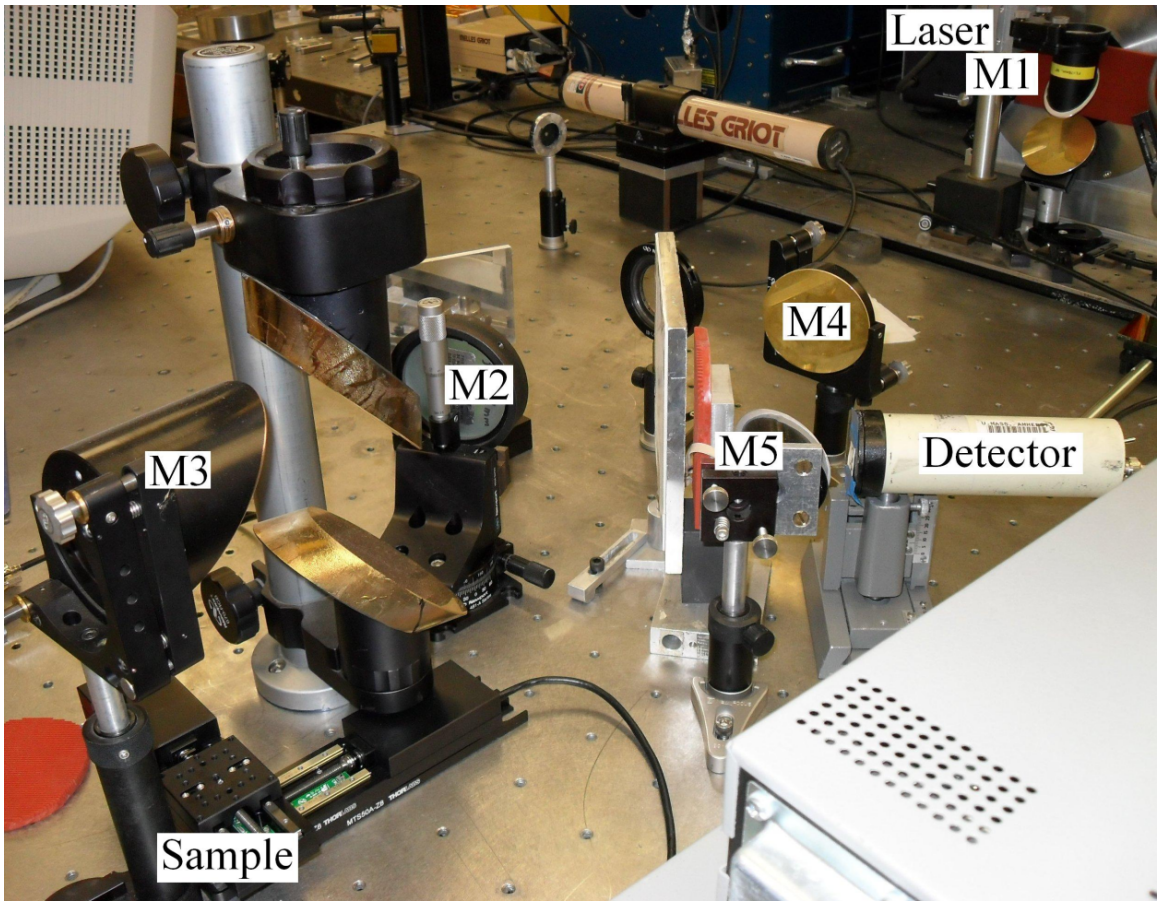

Figure 2.5: Photograph of Focusing Element Layout

2.3.2 Evaluation using Ray Transfer Matrices

Ray transfer matrices were used to find Gaussian beam width for all points along the beam path. Gaussian beam optics uses the paraxial approximation to avoid a full treatment of the diffraction of electromagnetic waves and is commonly used in THz setups [ZX09]. A paraxial ray is a ray which forms only small angles with the axis of propagation so that simplifying approximations such as $\sin\theta \approx \theta$, $\tan\theta \approx \theta$, and $\cos\theta \approx 1$ may be used.

First-order ray transfer matrices were applied with an iterative technique using the complex beam parameter, which is a combination of two beam dispersion parameters,

beam width and beam radius. Beam width follows from the definition of electric field strength in a Gaussian beam, described by

$$|E| = |E_0|e^{-r/w}, \tag{2.17}$$

where r is distance from the axis of propagation, E_0 is field magnitude at $r = 0$, and w is beam width for that particular point along the axis [Gol98]. When distance from the axis equals the beam width, the field strength is therefore reduced by a factor of e. At the focal plane, beam width is referred-to as beam waist and denoted w_0.

As axial distance from the focal point increases, beam width also increases. The equiphase wavefront may be thought-of as a patch on the surface of a sphere of radius R. This radius is called the Gaussian beam radius and is the second beam dispersion parameter. A beam with infinite beam radius would have a planar wavefront.

The two dispersion parameters are aggregated into a value, q, called the complex beam parameter. R, w, and q are functions of z, where z is position along the axis of propagation:

$$\frac{1}{q} \equiv \frac{1}{R} - j\frac{\lambda}{w^2\pi}. \tag{2.18}$$

Ray transfer matrices, sometimes called ABCD matrices, are used in iterative calculations of q as shown in (2.19), where Q is a normalization constant [Sie86]:

$$\begin{bmatrix} q_{\mathrm{n}} \\ 1 \end{bmatrix} = Q \begin{bmatrix} A & B \\ C & D \end{bmatrix} \begin{bmatrix} q_{\mathrm{n}-1} \\ 1 \end{bmatrix}. \tag{2.19}$$

Two equations follow from the matrix multiplication:

$$q_{\mathrm{n}} = QAq_{\mathrm{n}-1} + QB, \tag{2.20}$$

$$1 = QCq_{\mathrm{n}-1} + QD. \tag{2.21}$$

Dividing (2.20) by (2.21) allows for cancellation of the unknown constant:

$$q_{\mathrm{n}} = \frac{Aq_{\mathrm{n}-1} + B}{Cq_{\mathrm{n}-1} + D}. \tag{2.22}$$

Thin lenses and free space may be represented as ABCD matrices with d as distance and f as focal distance [Gol98]:

$$M_{\mathrm{vacuum}} = \begin{bmatrix} 1 & d \\ 0 & 1 \end{bmatrix}, \tag{2.23}$$

$$M_{\mathrm{thinLens}} = \begin{bmatrix} 1 & 0 \\ \frac{1}{f} & 1 \end{bmatrix}. \tag{2.24}$$

The combination of transfer matrices for our setup is as shown in (2.25), where identity matrices for non-focusing elements have been excluded:

$$M = \begin{bmatrix} 1 & d_5 \\ 0 & 1 \end{bmatrix} \begin{bmatrix} 1 & 0 \\ \frac{-1}{f_{\mathrm{m5}}} & 1 \end{bmatrix} \begin{bmatrix} 1 & d_4 \\ 0 & 1 \end{bmatrix} \begin{bmatrix} 1 & 0 \\ \frac{-1}{f_{\mathrm{m4}}} & 1 \end{bmatrix} \dots \begin{bmatrix} 1 & d_1 \\ 0 & 1 \end{bmatrix} \begin{bmatrix} 1 & 0 \\ \frac{-1}{f_{\mathrm{m1}}} & 1 \end{bmatrix} \begin{bmatrix} 1 & d_0 \\ 0 & 1 \end{bmatrix}. \tag{2.25}$$

Iterative calculations are seeded by knowing beam width at the source and setting initial beam radius to infinity. Using a Gaussian function, transmitted power may be expressed in terms of beam width and aperture radius, a [Sie86]:

$$P = \frac{2}{\pi w^2} \int_0^a 2\pi r e^{-2r^2/w^2} \, \mathrm{d}r = 1 - e^{-2a^2/w^2}. \tag{2.26}$$

By evaluation of (2.26), more than 99% of Gaussian beam power is found to pass through a hole of diameter $d = \pi w$ [Sie86]. The initial beam width is then approximately 4mm/π for our 4mm circular aperture.

Real-valued beam width and radius of curvature may be extracted from the complex beam parameter:

$$w(z) = \sqrt{\left| \frac{\lambda}{\pi \, \mathfrak{Im}\{1/q(z)\}} \right|}, \tag{2.27}$$

$$R(z) = \mathfrak{Re}\{q(z)\}. \tag{2.28}$$

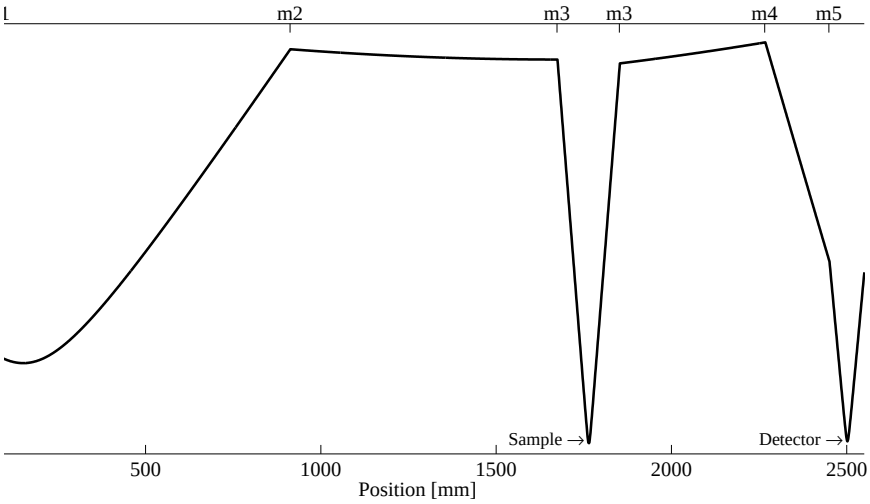

Figure 2.6: Beam Width by Position

In Figure 2.6, the maximum beam width is about 13mm. The largest mirror must therefore have a diameter of at least π(13mm) $\approx$ 4cm. Figure 2.6 also shows that beam widths at the detector and sample are about 600μm. A more careful treatment of beam width at the sample is provided in Section 2.9.

The beam is collimated only at the focal plane, before which it is converging and after which it is diverging. The axial range over which the beam may be considered reasonably collimated is known as the Rayleigh range [Dem03],

$$z_{\mathrm{R}} = \frac{\pi {w_0}^2}{\lambda}. \tag{2.29}$$

Using (2.29), acceptable margin of error for sample placement along the beam axis is $\pm$7mm.

2.4 Sample Cover

Because the system measures reflected power, it cannot distinguish between rough reflective surfaces and flat absorptive surfaces. For this reason, it is desirable to flatten samples with a material which is reasonably transparent to THz. Mylar and quartz covers were tested. The cover chosen for medical measurements was 1.9113mm single-crystal z-cut quartz.

2.4.1 Mylar

Available mylar thicknesses were 6μm and 25μm. Every attempt was made to keep the plastic taut over the sample, including heat-shrinking. Even so, bulges persisted as shown in Figures 2.7 and 2.8.

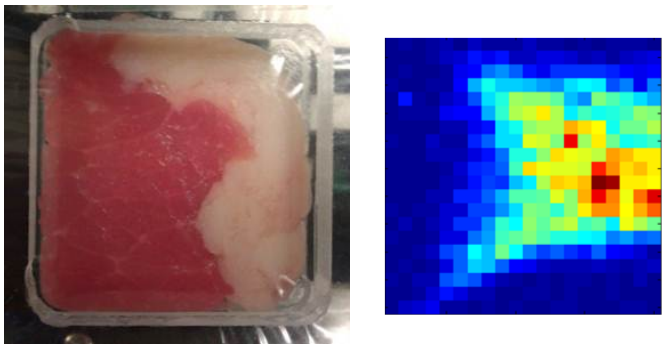

(a) Photo (b) THz

Figure 2.7: Mylar (6μm) on Beef

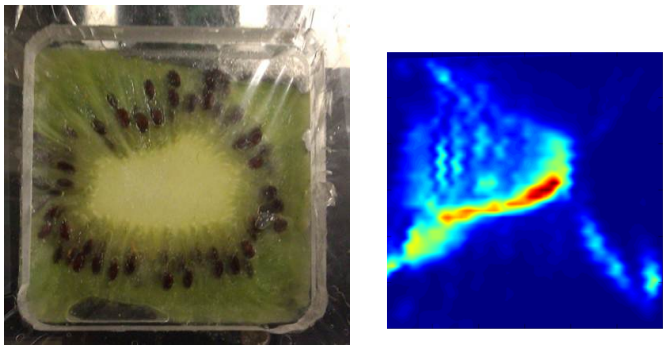

(a) Photo (b) THz

Figure 2.8: Mylar (6μm) on Kiwi

2.4.2 Quartz of 1.9113mm

The rigidity of quartz gives it an advantage over Mylar. It has a tensile modulus of more than 70N/m^2, meaning that more than 2.5N of force would be required for a 1μm deflection at our dimensions (see Appendix A). Also, it has a Moh's hardness of 7, making it difficult to scratch [Opt]. To replace Mylar, a quartz plate was characterized as follows:

1. Separate power reflectivity measurements were made for air and water using quartz covers as shown in Figure 2.9. The difference between those measurements was 14.5dB.

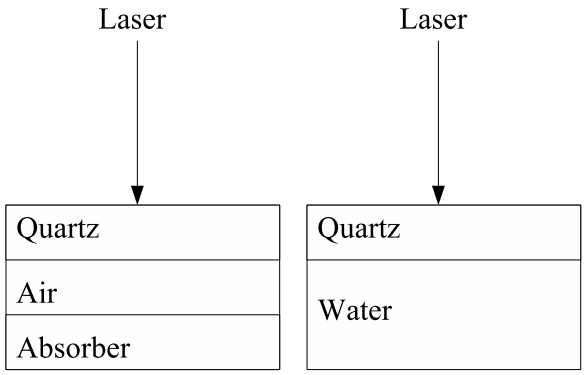

Figure 2.9: Air and Water Measurement

Each of the two measurement values was an average of 100 measurements at a single spatial point, taken according to the general measurement description given in Section 2.7.1. Standard deviations for air and water power reflectivity were 0.0024% and 0.089%.

2. Simulations were run for air (n=1) and water (n=2), plotting power reflectivity as a function of cover thickness. The refractive index value for water was calculated as explained in Section 2.8.2. The 14.5dB difference found in (1) corresponded to cover thicknesses of 1.9128mm+Nλ/2 and 1.9113mm+Nλ/2, where λ is 159μm.

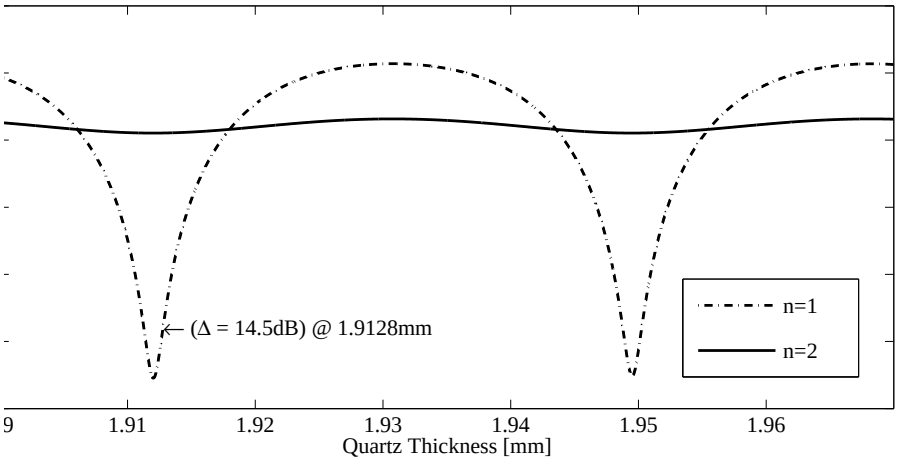

Figure 2.10: Thickness from $\Delta|\Gamma^2|$

Although thickness could have been any of several periodic values, 1.9113mm and 1.9128mm were closest to an approximate measurement made with a micrometer. This approximate thickness might also have been found using the interferometric technique described in Section 3.1.

3. Diffraction effectively attenuates the beam as it passes through the cover. From simulation, which does not consider diffractive losses, power reflectivity was 11.22% for covered water. This value, which is equal to -9.5dB, can be seen

in Figure 2.10 for n=2 at the relevant thicknesses. From measurement, which necessarily includes diffractive losses, power reflectivity was 4.40%. The ratio of these reflectivities, 2.55, may be regarded as a correction factor.

4. For quartz thicknesses of 1.9113mm and 1.9128mm, $|\Gamma_{\text{coveredSample}}|^2$ was determined from simulation for a range of relevant refractive indices (see Table 2.3 on page 37). The result was virtually identical for both thicknesses and is shown in Figure 2.11. Because there would be virtually no performance difference between a 1.9113mm cover and a 1.9128mm cover, the thickness is arbitrarily regarded as 1.9113mm for ease of communication. Before using the mapping of Figure 2.11, measured power reflectivities must be multiplied by the correction factor.

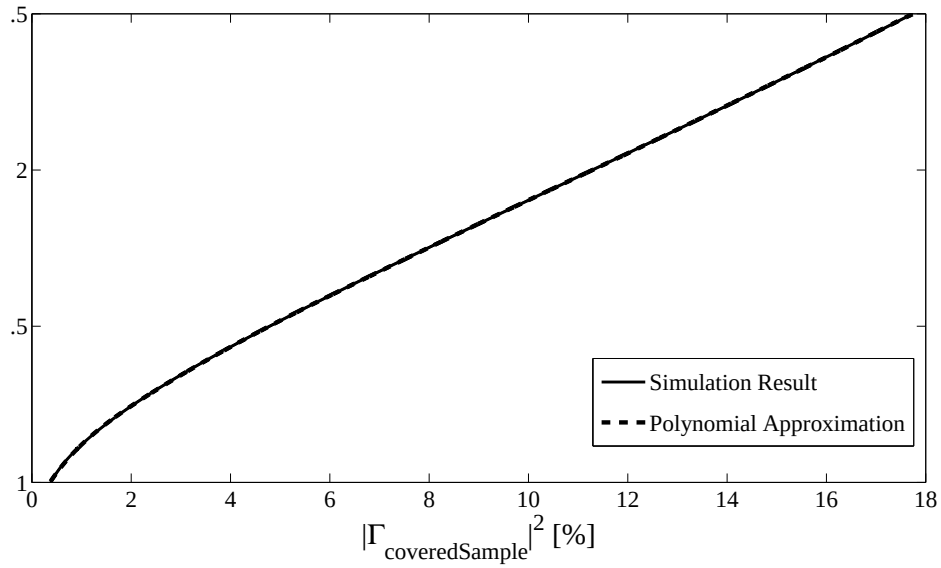

Figure 2.11: Mapping between $|n_{\text{sample}}|$ and $|\Gamma_{\text{coveredSample}}|^2$

All simulations were based on the schematic of Figure 2.12. The leftmost component represents air above the sample cover, the middle component represents the sample

cover, and the rightmost component represents the sample. Schematic parameters are defined in Table 2.2.

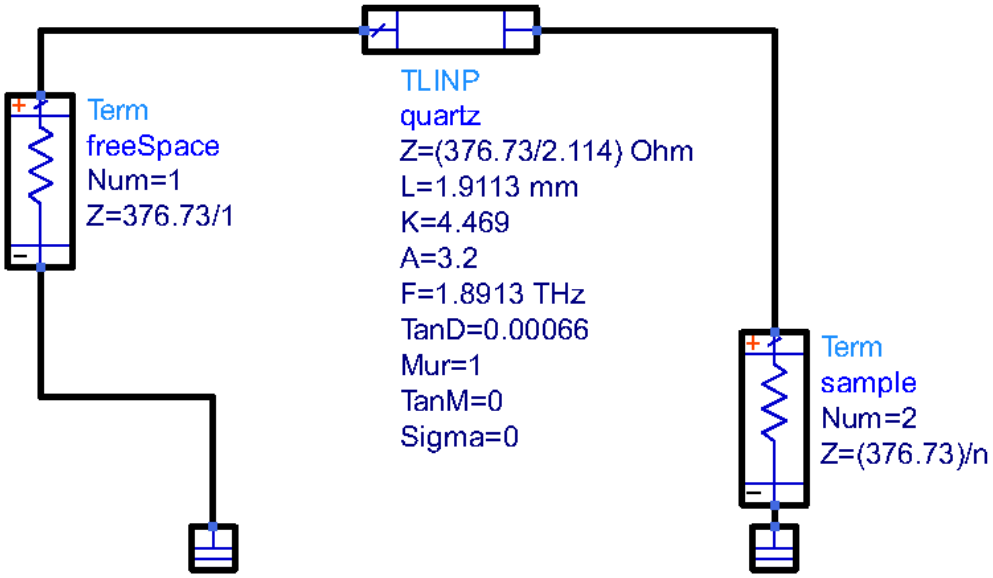

Figure 2.12: Agilent ADS Simulation Model

Property	Description
Z	Impedance [Ω]
L	Physical Length
K	Dielectric Constant
A	Attenuation Constant [dB/m]
F	Frequency
TanD	Loss Tangent
Mur	Relative Magnetic Permeability [H/m]
Sigma	Conductivity [S/m]

Table 2.2: Quartz Properties for Schematic Model

Applying $n = \sqrt{\varepsilon_\mathrm{r}}$ to the definition of impedance demonstrates why Z is expressed as a ratio of free-space impedance to refractive index for each component of Figure 2.12:

$$\eta \equiv \sqrt{\frac{\mu}{\varepsilon}} = \sqrt{\frac{\mu_0 \mu_\mathrm{r}}{\varepsilon_0 \varepsilon_\mathrm{r}}} \approx \sqrt{\frac{\mu_0}{\varepsilon_0 \varepsilon_\mathrm{r}}} = \frac{\sqrt{\mu_0/\varepsilon_0}}{\sqrt{\varepsilon_\mathrm{r}}} = \frac{\eta_0}{n} \approx \frac{376.73\Omega}{n}. \tag{2.30}$$

The effective dielectric constant, K (a.k.a. ε_r), must be known by the simulator to account for electrical path length differences. The relation between refractive index and wavelength is similar to the relation between refractive index and impedance:

$$\lambda = \frac{v_\mathrm{p}}{f} = \left(\frac{v_\mathrm{p}}{c}\right)\frac{c}{f} = \left(\frac{1}{n}\right)\lambda_0. \tag{2.31}$$

To demonstrate the importance of these changes in electrical path length, consider that a material of the same physical length could be either $\lambda/2$ or $\lambda/4$ depending on whether refractive index were 1 or 2. The design of a preliminary simulator, which does not consider electrical path length differences, is in Appendix B.

As shown in Figure 2.13, distance between periodic points of maximum transmission is 37.5μm. This can be verified as a half-wavelength by evaluation of (2.31). Refractive index was taken from Bréhat et al., who reported n for quartz of $2.114 + \mathrm{j}7 \cdot 10^{-4}$ at 1.89THz.

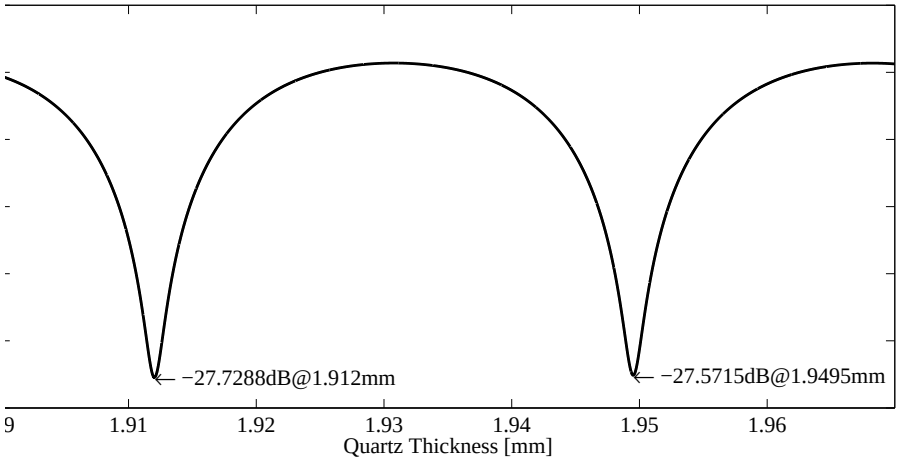

Figure 2.13: Periodic Points of Minimum Reflectivity

Dielectric constant, K, is the square of refractive index. It can be used to approximate loss tangent:

$$\tan\delta \equiv \frac{\varepsilon'' + (\sigma/\omega)}{\varepsilon'} \approx \frac{\varepsilon_{\mathrm{r}}''}{\varepsilon_{\mathrm{r}}'}, \tag{2.32}$$

$$\frac{\varepsilon_{\mathrm{r}}''}{\varepsilon_{\mathrm{r}}'} = \frac{\mathrm{Im}(n^2)}{\mathrm{Re}(n^2)} = \frac{2.96 \cdot 10^{-3}}{4.469} = 0.00066. \tag{2.33}$$

The attenuation parameter, A (a.k.a. α), may be calculated from loss tangent using (2.34) as derived in Section 3.2:

$$\alpha = \frac{\pi n}{\lambda_0} \tan\delta \approx \frac{\pi n}{\lambda_0} \left(\frac{\varepsilon_{\mathrm{r}}''}{\varepsilon_{\mathrm{r}}'} \right), \tag{2.34}$$

$$\frac{\pi(2.114)}{159\mu\mathrm{m}}(0.00066) = 27.6 \left[\frac{\mathrm{Np}}{\mathrm{m}} \right]. \tag{2.35}$$

The simulator required a unit conversion from the base-e Neper unit to the base-10 dB unit. In the following equations, D represents a dB quantity, N represents a Neper quantity, and A represents a ratio of field quantities:

$$[\mathrm{Np}] = \log_e(A), \tag{2.36}$$

$$[\mathrm{dB}] = 20\log_{10}(A)\,, \tag{2.37}$$

$$N\log_e A = D(20\log_{10}(A)), \tag{2.38}$$

$$D = \frac{N\log_e A}{20\log_{10} A} = \frac{N\log_e A}{20\,(\log_e A)\log_{10} e} = \left(\frac{N}{20\log_{10} e}\right), \tag{2.39}$$

$$\frac{27.6[\mathrm{Npm}^{-1}]}{20\log_{10} e} = 3.2\left[\frac{\mathrm{dB}}{\mathrm{m}}\right]. \tag{2.40}$$

At 3.2dB of loss per meter, it is evident why quartz is a material of choice for optics work. Of course, diffraction would present an additional loss.

2.4.3 Quartz of 0.475mm

The covered air and water measurements of the previous section were also made for 0.475mm quartz. Because the measured difference was about 10dB less than for the 1.9113mm quartz, it was decided to use the 1.9113mm quartz. Greater power reflectivity difference means easier sample classification.

An attempt was made to achieve a more amenable thickness by stacking 0.475mm quartz plates. However, probably due to an etalon effect between plates, the power reflectivity difference between air and water measurements was less than 1dB.

2.4.4 Quartz of Random Thickness

Quartz cover specifications are critical to the experimental setup. However, many research groups make little or no mention of the quartz cover. It is possible that luck has been on their side.

The cumulative distribution function (CDF) in Figure 2.14 shows that, given a reasonably thin quartz cover of random thickness, there is a 95% chance that power reflectivity difference between covered air and covered water measurements will be less than our value of 14.5dB. The CDF was created empirically by first calculating the difference between the $n = 1$ and $n = 2$ curves for a single period in Figure 2.10.

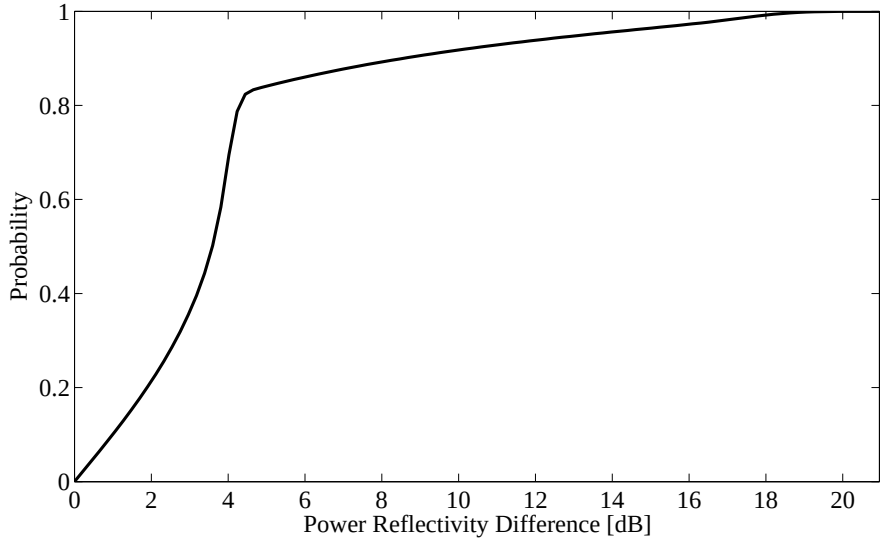

Figure 2.14: CDF

The probability density function (PDF) in Figure 2.15 shows that a 4dB difference would have been more likely.

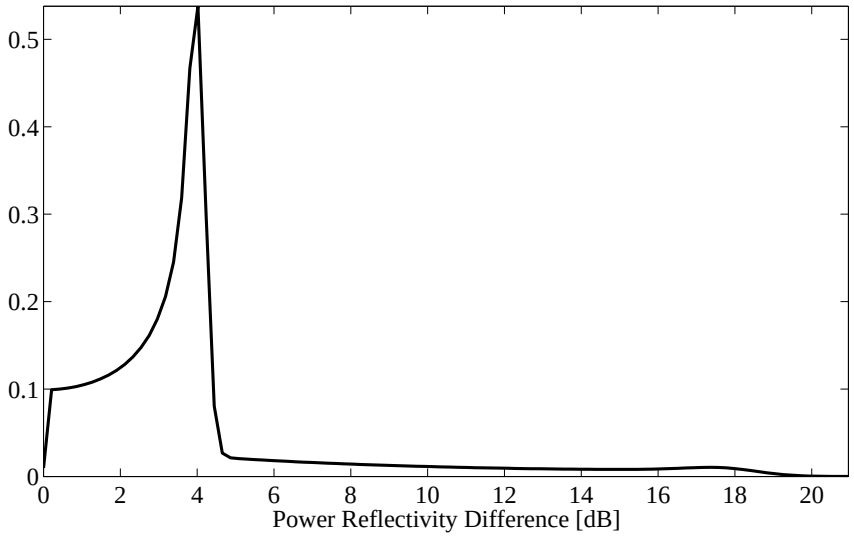

Figure 2.15: PDF

2.5 Sample Holder

2.5.1 Machined Acrylic

The present sample holder design is shown in Figure 2.16. It avoids the diffraction and meniscus concerns of the calibration basin design (see Section 2.5.2) and was relatively easy to machine. It consists of two pieces of acrylic, each approximately 6.5cm by 6.5cm by 0.5cm. The top square has a 3cm thru-hole cut from its center. The bottom piece has a 3cm square milled from its center with a depth of roughly 0.25cm. Using screws, the sample cover is tightly sandwiched between the two squares, with the sample itself pressed within the 0.25cm milled hole.

Figure 2.16: Acrylic Sample Holder

In an attempt to reduce reflections around the sample, an absorptive backing material was made at the Center for Hierarchical Manufacturing (CHM) at The University of Massachusetts in Amherst. A solution of carbon nanotubes was spun onto cardboard and dried. This absorber performed only marginally better than cardboard without nanotubes.

2.5.2 Design with a Calibration Basin

The preliminary design was created using Google Sketchup CAD software. The base is shown in Figure 2.17. Medical samples would go on the left 2cm-by-2cm pedestal and a solution of water and ethanol would go in the basin on the right to provide a calibration measurement for each row of a scanned image. The left cover would fit snugly into the groove which surrounds the pedestal and the right cover would slide onto the four pegs at the basin corners. Heights for left and right covers could be made equal by placement of appropriate washers on the pegs.

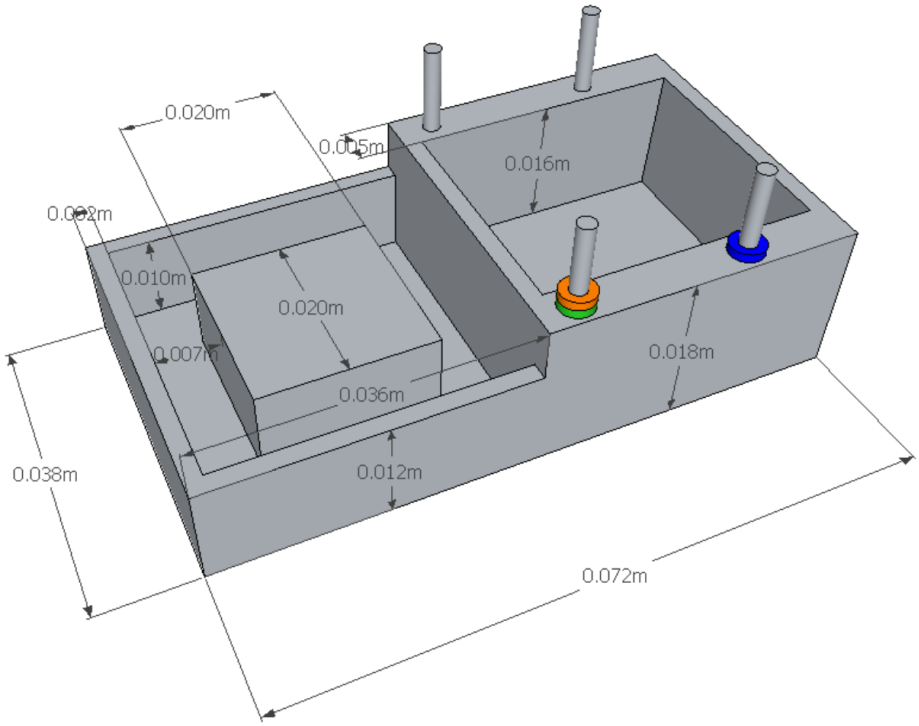

Figure 2.17: Base of Preliminary Sample Holder

In Figure 2.18, sample cover material is tinted yellow and absorber material is dark red.

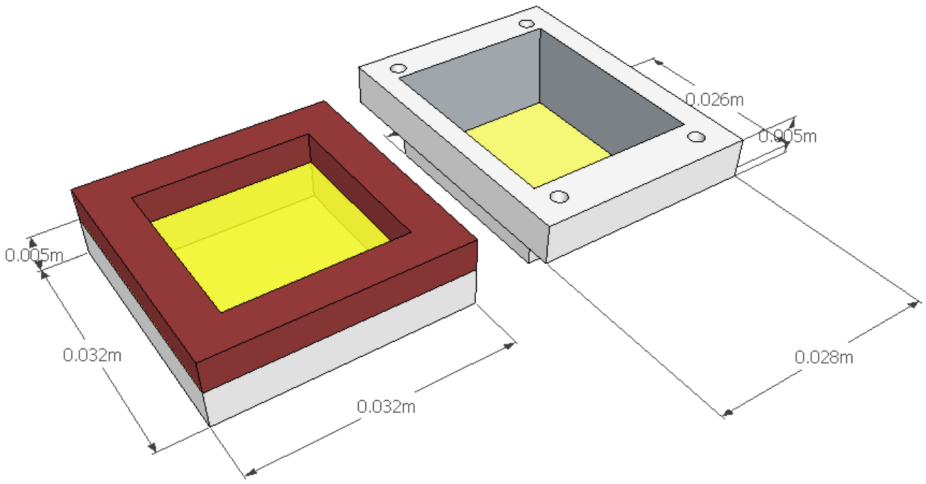

Figure 2.18: Covers for Preliminary Sample Holder

2.6 Detectors

The detectors measure laser power, which is modulated by diverting the excitory CO_2 beam with an acoustically produced diffraction grating. The diffraction grating is controlled by a 10Hz, 50% duty cycle square wave. Detector outputs, along with the square wave reference, go to lock-in amplifiers whose operation is explained in Section 2.7.1.

Measurements were initially made with only a Molectron P4-42 pyroelectric detector. Sensitivity was insufficient so it was replaced with a liquid-helium cooled bolometer. The current setup uses both detectors in the manner described in Section 2.8.1.

2.6.1 Pyroelectric Detector

The Molectron P4-42 pyroelectric detector operates by allowing radiation to heat a lithium tantalate ($LiTaO_3$) crystal. As temperature increases, crystal lattice spacings change, thus changing the polarization properties, thereby changing current flow through a transimpedance amplifier. Noise equivalent power of $90\text{nW}/\sqrt{\text{Hz}}$ is valid,

according to the datasheet, for 10Hz to 800Hz [Mol].

Measured detector response for different modulation frequencies is shown in Figure 2.19. For those measurements, water was placed in the sample location.

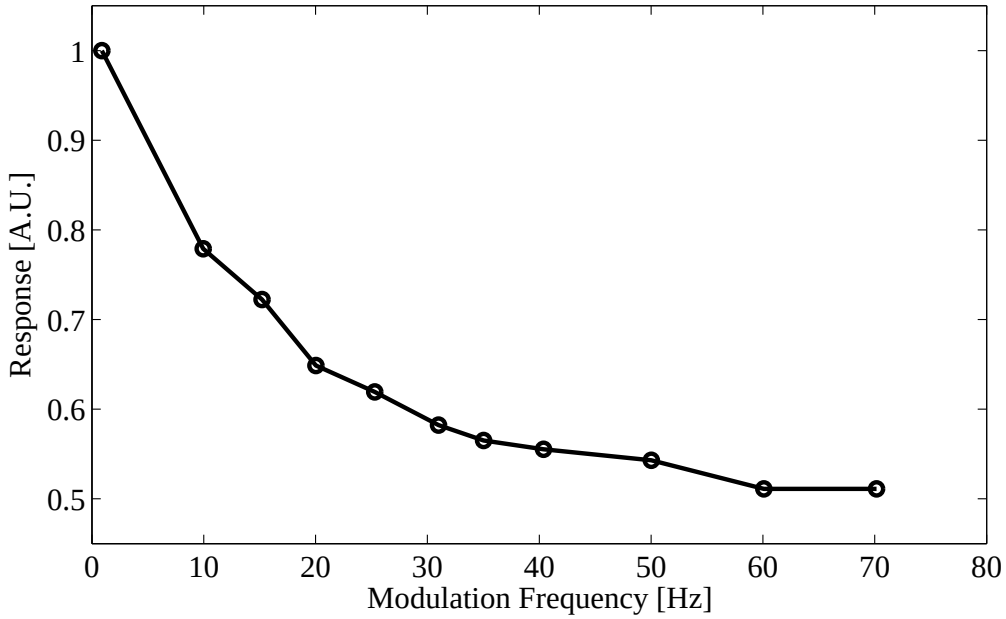

Figure 2.19: Pyroelectric Detector Frequency Response

2.6.2 Bolometer

The liquid-helium cooled bolometer, a model HDL-5 from Infrared Laboratories, is more sensitive than the pyroelectric detector and has a noise equivalent power of approximately $1\text{pW}/\sqrt{\text{Hz}}$. It works by allowing signals to heat a bulk silicon resistor. This detector exhibits a $1/f$ frequency response as shown in Figure 2.20.

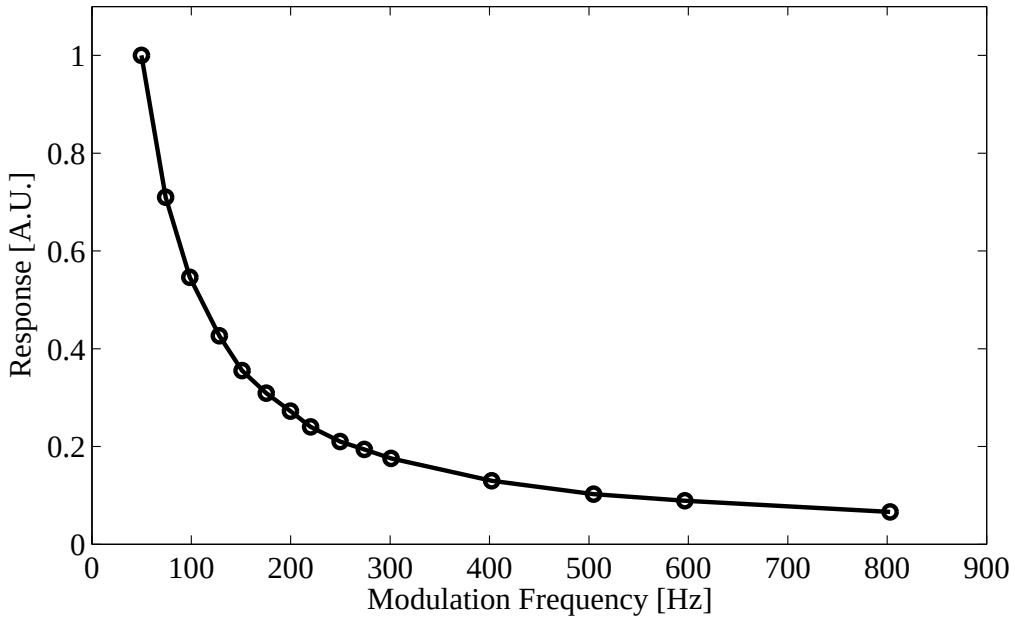

Figure 2.20: Bolometer Detector Frequency Response

For highest detector response, it seems reasonable to use the lowest practical modulation frequency for both detectors. However, below a certain modulation frequency, waveforms from the detectors contain high frequency components and variance increases. A good balance for the pyroelectric detector is 10Hz. Although the bolometer operates best at modulation frequencies of 50Hz or more, 10Hz was chosen to accommodate the lesser of the two detectors.

2.7 Lock-In Amplifiers and Data Capture

2.7.1 Discrete-Position Measurements

Each of the two detectors is connected to a separate lock-in amplifier. In this section, the terms *lock-in* and *lock-in amplifier* are used interchangeably. For an explanation of the role of each detector, see Section 2.8.1.

While reading values from the lock-in, the computer controls two motorized plat-

forms which position the sample. These movements cause samples to be measured in the chronological order shown in Figure 2.21. The number of rows, number of columns, and spatial intervals between pixels are all variable. Generally, 2cm square images are made at 1mm intervals.

13	14	15	16
12	11	10	9
5	6	7	8
4	3	2	1

Figure 2.21: Chronological Order of Measured Pixel Positions

The lock-in which connects to the bolometer has a time constant of 0.5s. The lock-in which connects to the pyroelectric detector has a time constant of 1s. These values were chosen qualitatively by monitoring signal volatility. They also fall within reasonable quantitative bounds because each time constant contains at least 5 modulation cycles and each pixel measurement has a duration of at least 5 time constants (5s).

Lock-in amplifiers use phase sensitive detection to achieve narrow bandwidths [Sta]. The noise introduced by any amplifier is

$$V_{\text{noise}} = G(NSD)\sqrt{BW}, \tag{2.41}$$

where NSD is noise spectral density in units of $\text{V}/\sqrt{\text{Hz}}$, BW is amplifier bandwidth, and G is voltage gain.

The advantage of using a lock-in amplifier can be put into context by comparing a lock-in setup to a low-noise amplifier (LNA) and low-pass filter combination. Assuming noise spectral density and gain to be the same for both setups, the performance difference is a function of bandwidth difference. At a 10Hz modulation frequency, the bandwidth of an LNA with a Q=10 bandpass filter would be 10Hz/10 = 1Hz. To calculate bandwidth for the lock-in, we start with the general differential equation for a first-order linear time invariant system,

$$\frac{\mathrm{d}V}{\mathrm{d}t} + \frac{1}{\tau}V = g(t), \tag{2.42}$$

where $V(t)$ is the time-dependent voltage output and $g(t)$ is a sinusoidal forcing function. This is an approximation because, as described in the previous section, detector output is not exactly sinusoidal. A convenient forcing function,

$$g(t) = \mathrm{A}e^{\mathrm{j}\omega t}, \tag{2.43}$$

contains real and imaginary sinusoidal functions rather than a single sinusoid. Later, this will be accounted-for by taking the magnitude. A first step in solving for $V(t)$ is the multiplication of both sides by an unknown integrating factor, $\mu(t)$:

$$\mu(t)\frac{\mathrm{d}V}{\mathrm{d}t} + \mu(t)\frac{1}{\tau}V = \mu(t)\mathrm{A}e^{\mathrm{j}\omega t}. \tag{2.44}$$

The integrating factor is defined in such a way that the left side of (2.44) will assume the form of the product rule:

$$\mu(t) \equiv \frac{\mu'(t)}{1/\tau}, \tag{2.45}$$

$$\mu(t)\frac{\mathrm{d}V}{\mathrm{d}t} + \mu'(t)V = (\mu(t)V(t))'. \tag{2.46}$$

The product rule form is substituted into (2.44) and both sides are integrated to find an expression for $V(t)$:

$$(\mu(t)V(t))' = \mu(t)\mathrm{A}e^{\mathrm{j}\omega t}, \tag{2.47}$$

$$\int (\mu(t)V(t))'\mathrm{d}t = \int \mu(t)\mathrm{A}e^{\mathrm{j}\omega t}\mathrm{d}t, \tag{2.48}$$

$$V(t) = \frac{\int \mu(t)\mathrm{A}e^{\mathrm{j}\omega t}\mathrm{d}t + \mathrm{C}}{\mu(t)}. \tag{2.49}$$

The chain rule is used to rearrange the $\mu(t)$ definition and substitute the derivative of a natural logarithm:

$$(g\,(f(t)))' = (g'\,(f(t))) \cdot f'(t) \implies (\ln \mu(t))' = \left(\frac{1}{\mu(t)}\right)\mu'(t), \tag{2.50}$$

$$\mu(t) \equiv \frac{\mu'(t)}{1/\tau} \implies (\ln \mu(t))' = \frac{1}{\tau}. \tag{2.51}$$

Both sides are integrated to find an expression for the integrating factor:

$$\int (\ln \mu(t))'\,\mathrm{d}t = \int \frac{1}{\tau}\mathrm{d}t, \tag{2.52}$$

$$\mu(t) = e^{\int (1/\tau)\mathrm{d}t + \mathrm{D}} = \mathrm{E}e^{t/\tau}. \tag{2.53}$$

Substitutions are made for $\mu(t)$, C/E is replaced by V_0, and the definite integral is evaluated:

$$V(t) = \frac{\int \mathrm{E}e^{t/\tau}\mathrm{A}e^{\mathrm{j}\omega t}\mathrm{d}t + \mathrm{C}}{\mathrm{E}e^{t/\tau}}, \tag{2.54}$$

$$V(t) = \mathrm{A}e^{-t/\tau}\int_0^t e^{t'(1/\tau + \mathrm{j}\omega)}\mathrm{d}t' + \mathrm{V}_0 e^{-t/\tau}, \tag{2.55}$$

$$V(t) = \mathrm{V}_0 e^{-t/\tau} + \frac{\mathrm{A}e^{-t/\tau}}{1/\tau + \mathrm{j}\omega}\left(e^{t/\tau}e^{\mathrm{j}\omega t} - 1\right), \tag{2.56}$$

$$V(t) = \mathrm{V}_0 e^{-t/\tau} + \frac{\mathrm{A}}{1/\tau + \mathrm{j}\omega}\left(e^{\mathrm{j}\omega t} - e^{-t/\tau}\right). \tag{2.57}$$

The steady-state response is the response as time goes to infinity:

$$V_\infty(t) = \frac{\mathrm{A}e^{\mathrm{j}\omega t}}{1/\tau + \mathrm{j}\omega}, \tag{2.58}$$

$$|V_\infty(t)| = \mathrm{A}\frac{1}{\sqrt{(1/\tau)^2+\omega^2}} = \mathrm{A}\tau\frac{1}{\sqrt{1+(\omega\tau)^2}}. \tag{2.59}$$

The half-power point will occur where the field response is $1/\sqrt{2}$. From inspection of (2.59), this will happen when $\omega\tau = (2\pi f_{3\mathrm{dB}})\tau = 1$. The half-power frequency is therefore

$$f_{3\mathrm{dB}} = \frac{1}{2\pi\tau}. \tag{2.60}$$

The bandwidth is defined as the frequency range from from 0Hz to $f_{3\mathrm{dB}}$:

$$BW = f_{3\mathrm{dB}} - 0\mathrm{Hz} = \frac{1}{2\pi\tau}. \tag{2.61}$$

For the bolometer time constant of 0.5s, bandwidth is 0.32Hz. The noise power is therefore about 3 times less for the lock-in setup than for the LNA and filter combination.

2.7.2 Continuous-Velocity Measurements

Instead of moving the motorized platform at discrete intervals, the sample was moved at a constant velocity for each horizontal sweep. These measurements were made when the bolometer, which can operate at high modulation frequencies, was the only detector in the system.

Considerable experimentation was done for determination of optimal platform velocity, time constant, and modulation frequency. One acceptable combination was 1mm/s, 20ms, and 50Hz. Improper combinations caused image artifacts such as that shown in Figure 2.22. For this example, the time constant was too large, causing smearing of what should have appeared as a rectangle. Examples of continuous-velocity measurements with appropriate settings may be seen in Figures 2.8, 2.38, and 4.3.

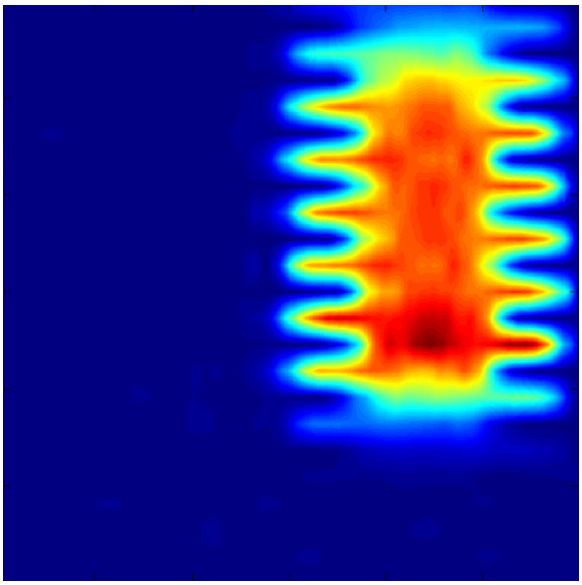

Figure 2.22: Time Constant Artifact

2.8 Calibration

2.8.1 Dual Detector Method

Frequent calibration was necessary because of laser source fluctuations. To calibrate a single-detector system, the sample holder of Section 2.5.2 was designed with a side basin for calibration liquid.

The presently employed method instead uses two detectors for continuous calibration. For convenience, *pyroelectric detector* and *pyro* are used interchangeably in this section. Near the output aperture of the laser source, a 25μm beam splitter diverts half the beam to be focused onto the pyroelectric detector. For this, a 150mm off-axis paraboloidal mirror (OAP) was placed 700mm after the laser aperture and the pyro was placed 200mm after the OAP. The beam splitter is placed between elements m_1 and m_2 of the original setup as shown in Figure 2.23. Beam width is shown in Figure 2.24.

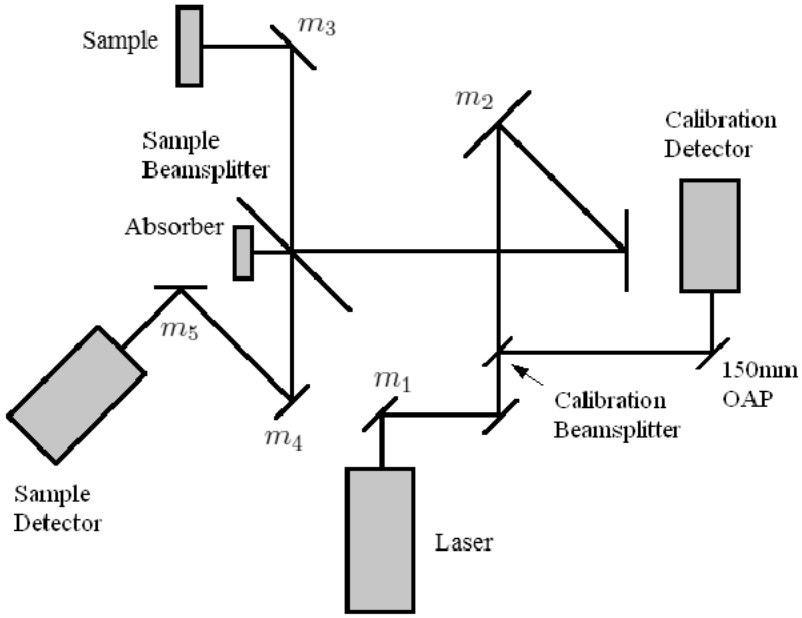

Figure 2.23: Element Layout Updated with Calibration Branch

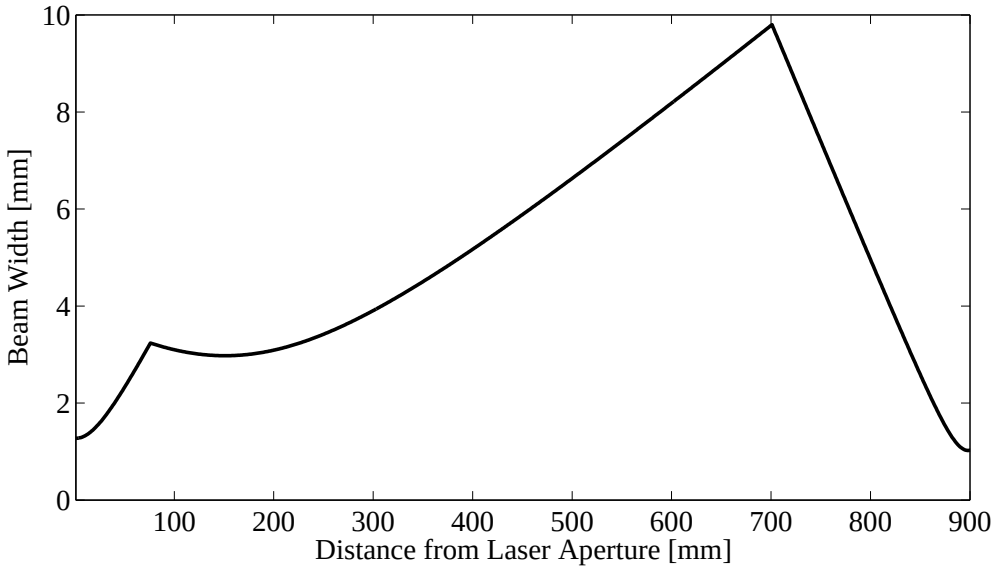

Figure 2.24: Beam Width from Laser to Calibration Detector

Power of the laser source, S, is attenuated by $G_{\text{laserToPyro}}$ along its path to the pyro detector, which has a response of G_{pyro}. Power reported by the pyro, P, can be calculated with

$$P = SG_{\text{laserToPyro}}G_{\text{pyro}}. \tag{2.62}$$

The power of the laser source, S, is attenuated by $G_{\text{laserToSample}}$ along its path to the sample, where sample power reflectivity may be denoted as R. The power is then attenuated by $G_{\text{sampleToBolometer}}$ along its path to the bolometer, which has a response of $G_{\text{bolometer}}$. The power reported by the bolometer, B, is calculated with

$$B = SG_{\text{laserToSample}}RG_{\text{sampleToBolometer}}G_{\text{bolometer}}. \tag{2.63}$$

S cancels when a ratio of B and P is taken. The remaining gain terms may be aggregated into a constant, Q, as in

$$\frac{B}{P} = R\left(\frac{G_{\text{laserToSample}}G_{\text{sampleToBolometer}}G_{\text{bolometer}}}{G_{\text{laserToPyro}}G_{\text{pyro}}}\right) = RQ. \tag{2.64}$$

Q may be determined by evaluating $B/(PR)$ for a sample of known R. Silicon is used, which has $R = 0.299$. [JMY+00].

After solving for Q with a calibration measurement, the silicon may be replaced with any sample of interest. Sample power reflectivity follows from evaluation of $B/(PQ)$. Because Q contains only system constants, re-calibration is unnecessary. It should be mentioned that what has been referred-to as a sample in this section, except for the silicon sheet, was a combination of a sample material and a quartz cover. To compensate for cover effects, additional calculations are necessary as described in Section 2.4.

Figure 2.25 shows a measurement (Sample 7A) in which laser power decreased. Without two-detector calibration, the result would not have been useful.

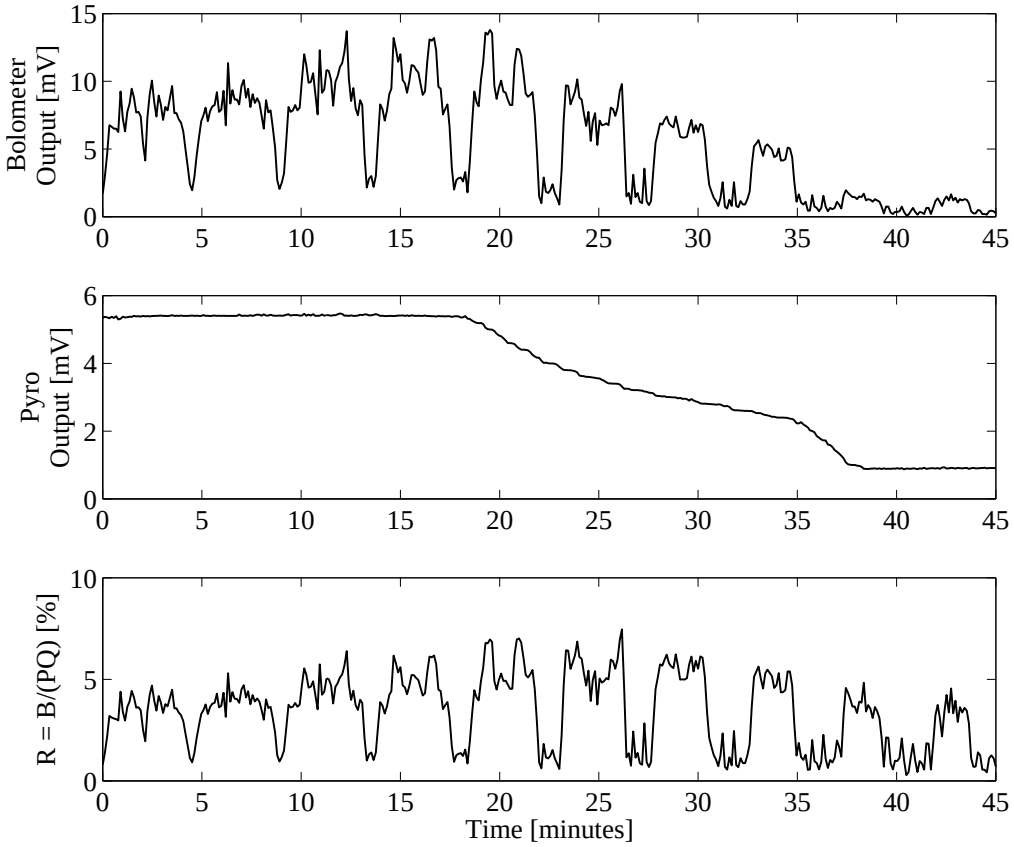

Figure 2.25: Laser Power Changing During Measurement

2.8.2 Ethanol Solution Method

The system can be calibrated by measuring a material of known reflectivity. Power reflectivity of water was calculated by using the Double Debye Model as described by Jepsen et al. [JMM07]. In this model, τ_1 and τ_2 are relaxation times, ε_s is static dielectric constant, and ε_∞ and ε_1 are parameters indicating the amount of coupling between the relaxation mode and electric field:

$$\varepsilon_\mathrm{r}(\omega) = \varepsilon_\infty + \frac{\varepsilon_\mathrm{s} - \varepsilon_1}{1 - j\omega\tau_1} + \frac{\varepsilon_1 - \varepsilon_\infty}{1 - j\omega\tau_2}. \tag{2.65}$$

For a laser frequency of 1.89THz, the relative electrical permittivity is $3.80 - \mathrm{j}1.48$ from evaluation of (2.65). With $|\varepsilon_\mathrm{r}| = \sqrt{3.80^2 + 1.48^2} = 4$, power reflectivity may be calculated as

$$|\Gamma_\mathrm{water}|^2 = \left(\frac{\sqrt{|\varepsilon_\mathrm{r}|} - 1}{\sqrt{|\varepsilon_\mathrm{r}|} + 1}\right)^2 = \left(\frac{2-1}{2+1}\right)^2 = \frac{1}{9}. \tag{2.66}$$

Jepsen et al. has a similar treatment for ethanol [JMM07]. The Triple Debye Model,

$$\varepsilon_\mathrm{r}(\omega) = \varepsilon_\infty + \frac{\varepsilon_\mathrm{s} - \varepsilon_1}{1 - j\omega\tau_1} + \frac{\varepsilon_1 - \varepsilon_2}{1 - j\omega\tau_2} + \frac{\varepsilon_2 - \varepsilon_\infty}{1 - j\omega\tau_3}, \tag{2.67}$$

evaluates to a dielectric constant of 2.09, which is equivalent to a refractive index of 1.45 or a power reflectivity of 3.32%. The expected power reflectivities for human tissues were calculated using dielectric properties as measured by Ashworth et al. [APMP+09]. Values for all these materials are shown in Table 2.3.

	|n|	$\|\Gamma\|^2$
Water	2.00	11.1%
Carcinoma	1.97	10.7%
Fibrous Tissue	1.85	8.9%
Adipose Tissue	1.57	4.9%
Ethanol	1.45	3.3%

Table 2.3: Refractive Index and Power Reflectivity by Calibration Fluid and Tissue Type

To make frequent calibration measurements, the calibration fluid should have a reflectivity similar to that of the medical samples. Water, with a power reflectivity of more than 11%, is more reflective than medical samples at 1.89THz. However, solutions of water and ethanol can be mixed to produce a better calibration fluid because ethanol reflects less than water and because power reflectivity has a near-linear relationship

with ethanol concentration [JMM07]. To verify this, power reflectivity measurements were made of different ethanol concentrations.

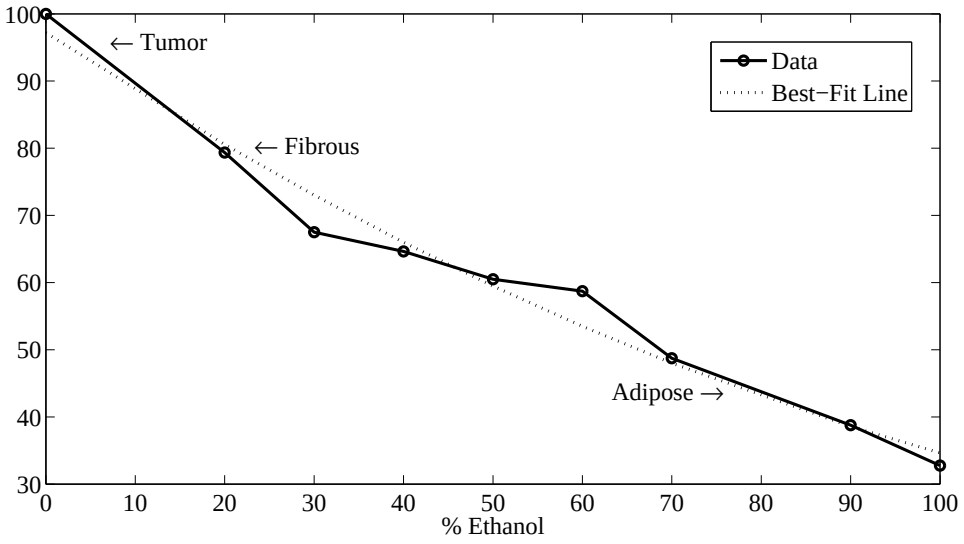

Figure 2.26: Ethanol Reflectivity and Corresponding Tissue Types at 1.89THz

The preliminary measurements of Figure 2.26 were made with a single-detector version of our measurement setup. The system no longer uses this ethanol solution method. Using liquids was messy and error-prone due to measurement imprecision and surface tension effects. Instead, the method of Section 2.8.1 is used.

2.9 Resolution

The THz beam is cropped by a circular aperture as it exits the laser source. The resulting far-field diffraction pattern, known as an Airy disk, is shown in Figure 2.27.

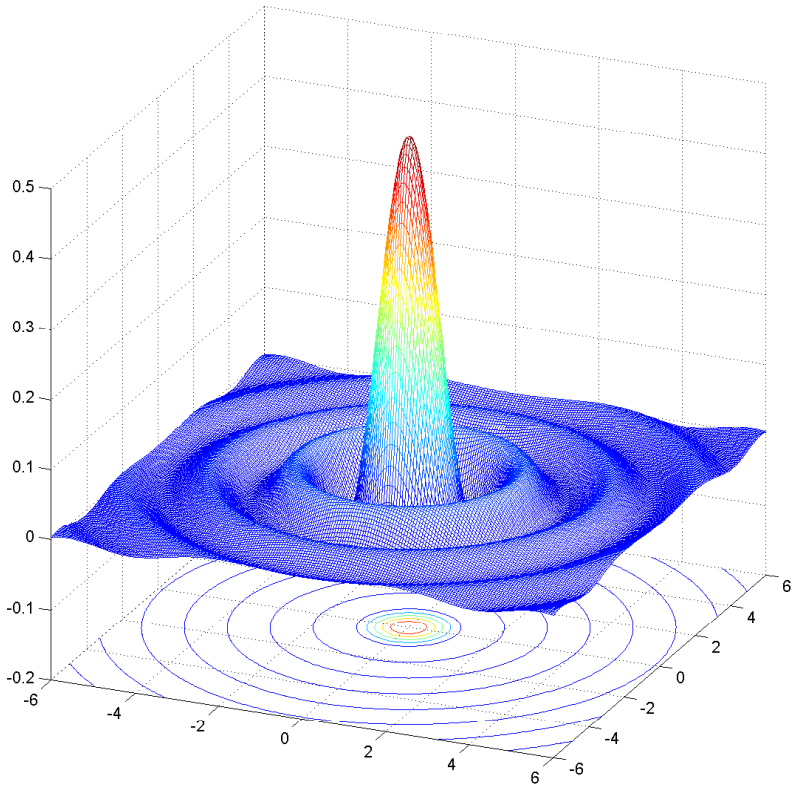

Figure 2.27: System Beam Field Pattern (Airy Disk)

The central cross-section of an Airy disk is sometimes called a jinc function, so-named for its similarity to the sinc function. It is written as

$$\text{jinc}(z) \equiv \frac{J_1(z)}{z}, \tag{2.68}$$

where $J_1(z)$ is a first-order Bessel function of the first kind. Bessel functions are employed because they solve an expression for field amplitude in a plane, known as the general Huygens' integral [Sie86].

The resolution is sometimes defined as the distance from the center of an Airy disk to

its first null. If the centers of two identical Airy disks were closer than that distance, they would no longer be resolvable. This is known as the Rayleigh criterion.

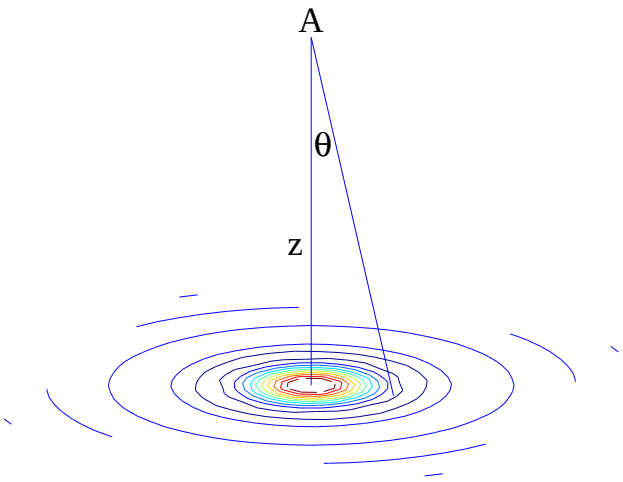

Figure 2.28: Far-Field Diffraction

In Figure 2.28, A is the aperture location and z is the distance from the aperture to the projection. The half-angle, θ, may be approximated by

$$\theta \approx \frac{1.22\lambda}{D}, \tag{2.69}$$

where D is the aperture diameter [Sie86]. A solution is found for the resolution, r, by applying trigonometry to Figure 2.28 and using $\tan\theta \approx \theta$, such that

$$r = z\tan\theta \approx z\theta \approx z\left(\frac{1.22\lambda}{D}\right). \tag{2.70}$$

In our setup, z is also the focal length, f, of a focusing mirror. It is worth noting that f/D is the definition of *f-number*, a commonly used term in optics and photography.

The beam width radius at A is about 13mm as shown in Figure 2.6. The focal length of the mirror over the sample is 89mm as shown in Table 2.1. Resolution can be calculated as

$$r \approx f\left(\frac{1.22\lambda}{D}\right) = 89\text{mm}\left(\frac{(1.22)159\mu\text{m}}{2(13\text{mm})}\right) = 665\mu\text{m}. \tag{2.71}$$

Some error has been introduced because Gaussian beam optics was used to find the 13mm beam width but this treatment uses Airy disk diffraction.

A simple resolution metric is the distance between 10% power and 90% power in a unit step measurement. For this, a gold mirror was masked with absorptive tape to create a reflective section in a 20mm line measurement. The length of this section was 5.1mm for the horizontal measurement and 5mm for the vertical. The discrepancy is a result of the tape strips not being perfectly parallel. Figures 2.29 and 2.30 show the resolution to be about 1.8mm for both cases. This is larger than the 1mm interval of the motorized platform (see Section 2.7.1), so the system therefore oversamples with regard to the point spread function (PSF). As empirically determined from the data of Figure 2.27, the power within a 1mm pixel is about 75% of beam power.

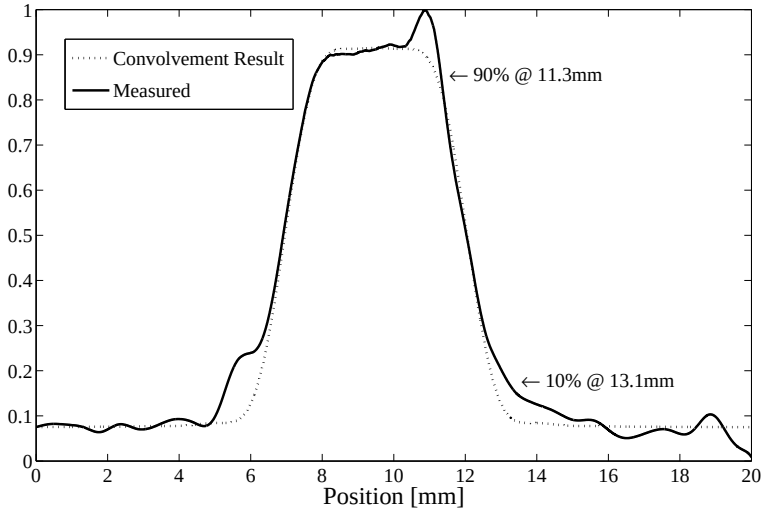

Figure 2.29: Horizontal Resolution Measurement

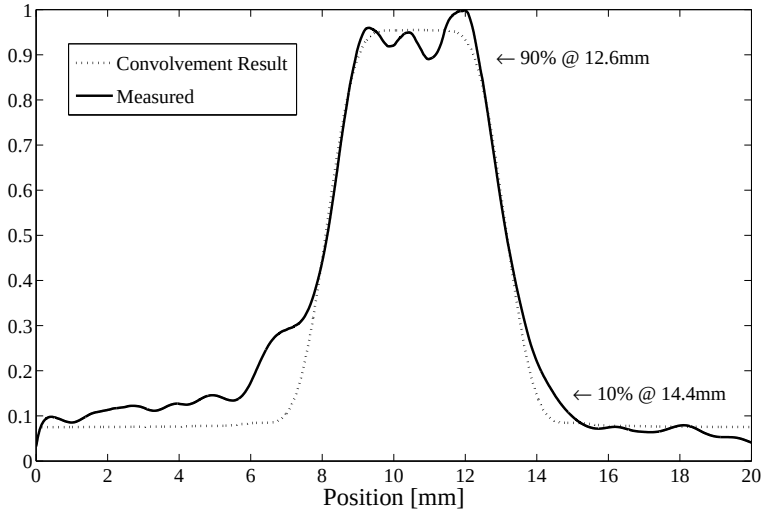

Figure 2.30: Vertical Resolution Measurement

Another way of determining resolution is to consider that the measured power reflectivity result is the convolution of a squared Airy disk cross section with a single rectangular pulse. The squared Airy disk cross section was stretched and compressed along the horizontal axis until the convolution result resembled the measured data.

The final convolvement results are shown in Figures 2.29 and 2.30. Discrepancies between the measurements and the fit curves could be due to the sample not being a perfectly reflective stripe, excitation of higher-order modes in the FIR laser tube, or the beam having diffracted in an unexpected way. According to Siegman, a center coupling hole in an FIR tube can introduce higher-order Hermite-Gaussian modes [Sie86].

The power distribution is the area-normalized square of the Airy disk. To match the 10% to 90% resolution value of 1.8mm, power within the resolution beam width would be 85% of total beam power. Figure 2.31 applies to both the horizontal and vertical scans.

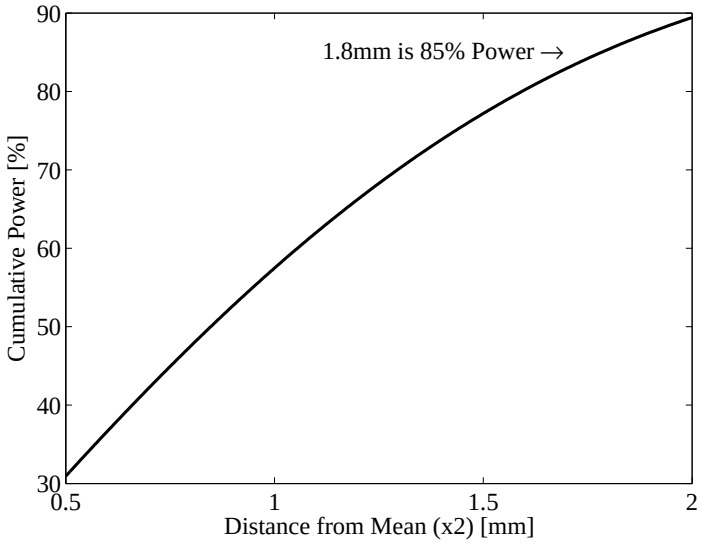

Figure 2.31: Cumulative Power in the Airy Disk of Figure 2.27

2.10 Post-Processing

2.10.1 Technique and Calculations

Refractive index is calculated from THz measurements as described in Section 2.8.1. Next, a projective planar transformation is applied to an optical photograph for image superposition as shown in Figure 2.32, accounting for variations in orientation and position of the optical camera. For the projective transformation, six corresponding points were chosen between the optical and THz images. Most of the image processing was done with Matlab and the Image Processing Toolbox. Sample 7A is used as an example in this section.

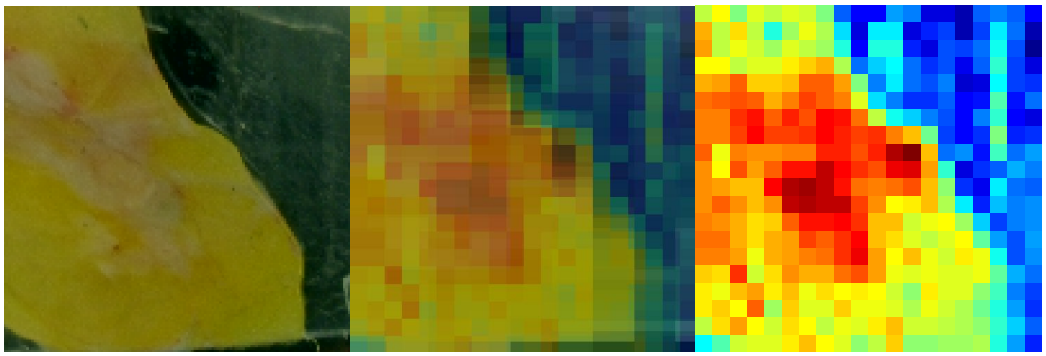

(a) Optical (b) Optical and THz (c) THz

Figure 2.32: Superimposed Optical and THz Images

The discrete-position measurement technique is used to produce images such as the rightmost image of Figure 2.32. Smoothened versions of these images, which can be seen in the results section and in Figure 2.33, are created with spline interpolation for aesthetics and ease of comparison with optical images. Suggestions for a more-advanced interpolation technique are provided in Section 5.3.

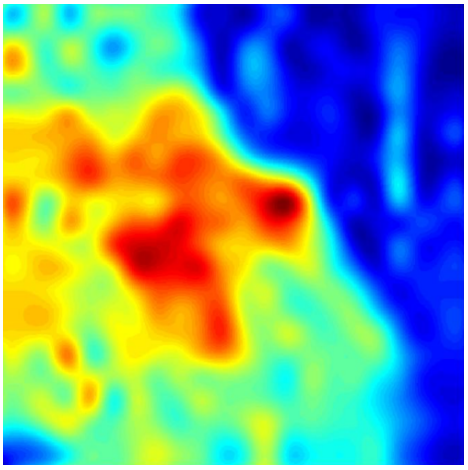

Figure 2.33: Spline Interpolation

A mask is created to exclude those pixels which are not part of the medical sample. The resolution matches the measurement grid, which is usually 20mm by 20mm.

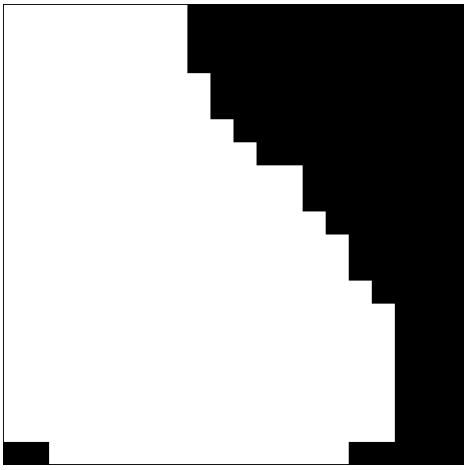

Figure 2.34: Off-Sample Mask

Cancerous regions are identified using histological micrographs which have been annotated by medical doctors. Histological micrographs are made into maps, which are made into masks. Micrographs can be seen in Appendix D. Maps and masks can be seen in the Results section and also in Figure 2.35. Cancer masks are regarded as the

true references against which THz images must be compared.

Histology maps are made manually from micrographs with assistance from GNU Image Manipulation Program (GIMP) software. Simple projective transformations, of the type utilized for mapping THz images onto optical images, would have been inadequate for correction of the multi-dimensional squashing and stretching that occurs during the histology process. Masks are made by applying a color thresholding algorithm to the maps.

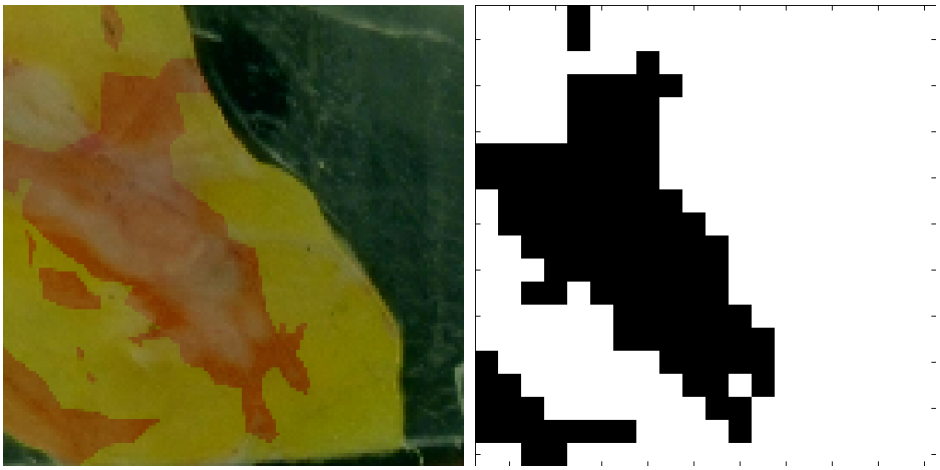

(a) Histology Map (b) Cancer Mask

Figure 2.35: Map and Mask

Because cancer is the most reflective of our tissue types, it suffices to set some limit, $n_{threshold}$, such that tissue is regarded as cancerous if $n_{measured} \geq n_{threshold}$. As this limit is varied, a succession of masks is created for comparison to the mask of Figure 2.35b.

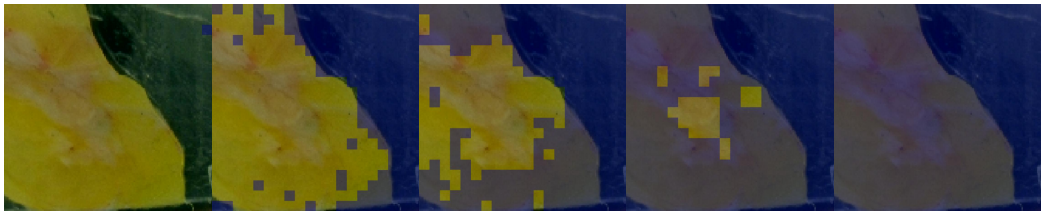

(a) $n_{thresh} = 0.98$ (b) $n_{thresh} = 1.38$ (c) $n_{thresh} = 1.46$ (d) $n_{thresh} = 1.60$ (e) $n_{thresh} = 1.71$

Figure 2.36: Varying Refractive Index Threshold

The leftmost mask of Figure 2.36 has the lowest $n_{threshold}$ and identifies every pixel as a cancerous region. By doing this, the system has coincidentally classified every cancerous pixel as cancerous and so the true positive rate is 1. In other words, the sensitivity is 1.

The rightmost mask of Figure 2.36 has the highest $n_{threshold}$ and no cancer has been identified. By doing this, the system has coincidentally classified every non-cancerous pixel as non-cancerous and so the true negative rate is 1. In other words, the specificity is 1.

It is common to illustrate sensitivity and specificity using a receiver operating characteristic (ROC) plot. The medical community requires false positive rate (FPR) along the abscissa, which is equivalent to one minus the specificity. The refractive index threshold has been mapped to a color scale.

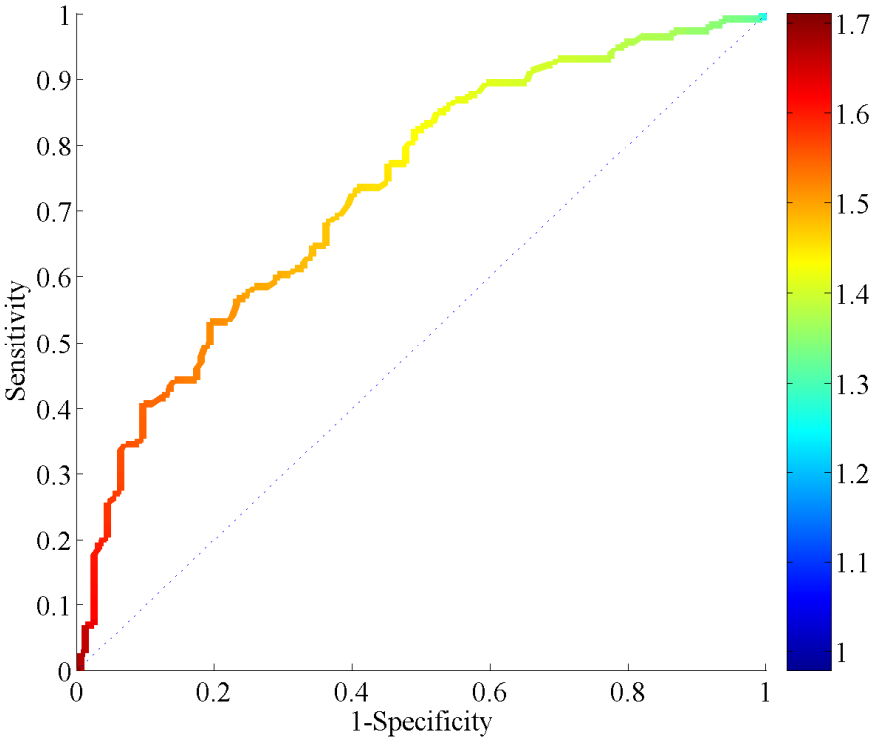

Figure 2.37: ROC with Color Mapping for $n_{threshold}$

These plots are useful when, for example, a doctor would like to know with 90% certainty that a true test result will be correct. In the case of Figure 2.37, he would know to set n_{thresh} to about 1.45 by using the color code. At that operating point, he would expect a $1 - 0.6 = 40\%$ chance of a false test result being correct. However, due to variations in refractive index values for the same tissue types across different samples, the usefulness of setting $n_{threshhold}$ using the ROC is limited.

A figure of merit for ROC plots is the area under the curve, sometimes called the discrimination. Discrimination is closer to 1 for systems having coincidentally high sensitivity and specificity.

2.10.2 Animation

Each image has a range of power reflectivity or refractive index values corresponding to a color scale. Detail can be lost when the full range is displayed. One solution is to animate, with all frames sharing the power reflectivity range lower-bound but with each subsequent frame having a higher upper-bound. A saturation color is shared by all power reflectivity values higher than the upper-bound. Figure 2.38 is an example of this, containing still-frame captures from a video. The leftmost image has the smallest range and the rightmost has the largest. In these frames, it can be seen that Capture 4 has drowned out details that were clearly visible in Capture 2.

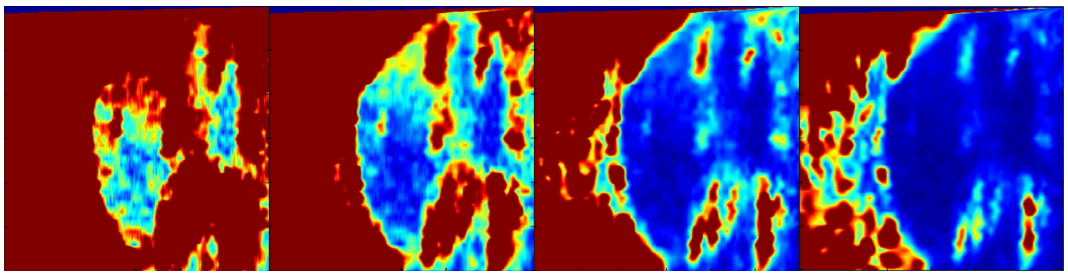

(a) Capture 1 (b) Capture 2 (c) Capture 3 (d) Capture 4

Figure 2.38: Animation Still-Frames

Still frames from the second animation technique are shown in Figure 2.36. Pixels are highlighed as the refractive index threshold is swept from identifying everything as cancerous to identifying nothing as cancerous. Animation is now seldom employed because most of their contained information can be more-easily conveyed using a color-coded ROC curve.

CHAPTER 3

SPECIAL TOPICS

3.1 Quartz Thickness from Transmission Measurements

3.1.1 RIKEN Quartz

In this section, transmission measurements made available by the RIKEN Tera-Photonics Laboratory in Japan [Lab11], are used to determine cover thickness.

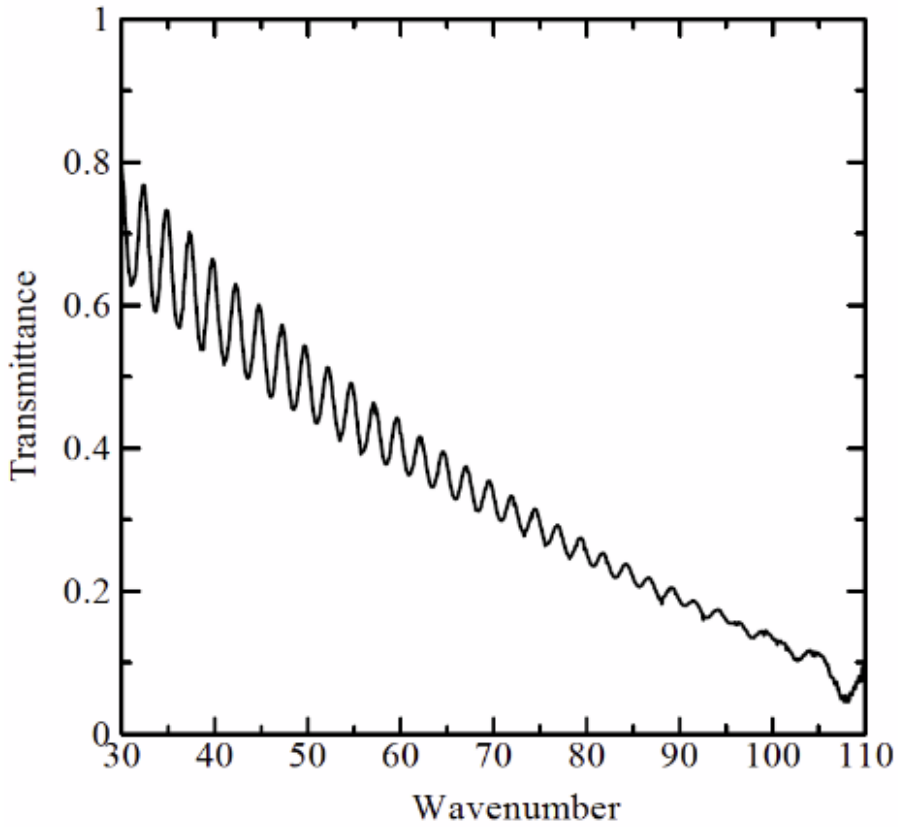

Figure 3.1: RIKEN Quartz Transmittance by Wavenumber [cm^{-1}]

Although the Tera-Photonics Laboratory listed the thickness of their quartz, this could have been determined from the transmission data itself. Peaks of Figure 3.1 correspond to frequencies for which the electrical length of the quartz is a multiple of half-wavelengths. Consider two adjacent peaks. Where T is physical quartz thickness, the first peak must satisfy the half-wavelength constraint:

$$T = N\left(\frac{\lambda_1}{2}\right) = N\left(\frac{\lambda_0/n}{2}\right) = N\left(\frac{(c/f_1)/n}{2}\right) = \frac{Nc}{2f_1 n}, \tag{3.1}$$

$$f_1 = \frac{Nc}{2nT}. \tag{3.2}$$

The second peak will be at a frequency for which the physical thickness of quartz will contain an additional half-wavelength:

$$f_2 = \frac{(N+1)c}{2nT} = \frac{Nc}{2nT} + \frac{c}{2nT}. \tag{3.3}$$

Physical thickness may be expressed in terms of frequency difference:

$$f_2 - f_1 = \frac{c}{2nT}, \tag{3.4}$$

$$T = \frac{c}{2n \bigtriangleup f}. \tag{3.5}$$

If it seems counterintuitive that resolving a thick piece of quartz is more difficult than resolving a thin piece, it may help to consider the subtle difference between f and Δf. Whereas small f would generally be easier to resolve, small Δf is just the opposite.

Equation 3.5 may now be applied to the data of Figure 3.1. The average frequency

interval between peaks is calculated and thickness is found to be close to 1mm as given by the Tera-Photonics Laboratory:

$$\Delta f = \frac{\mathrm{c}(94\mathrm{cm}^{-1} - 32.5\mathrm{cm}^{-1})}{25\,\mathrm{periods}} = 73.8\mathrm{GHz}, \tag{3.6}$$

$$T = \frac{c}{2n\Delta f} = \frac{c}{2(2.114)73.8\mathrm{GHz}} = 0.96\mathrm{mm}. \tag{3.7}$$

3.1.2 Quartz of 0.475mm

A Michelson interferometer with a broadband globar source was used to make transmission measurements, utilizing the same bolometer detector and motorized platforms as the medical setup. *Globar*, a portmanteau of *glow* and *bar*, is a thermal radiation source with behavior approximating that of a Planck black-body. This interferometric apparatus had been assembled by another student for a thesis project [Mut11].

Measurements were first taken with no quartz plate in the beam path. The mirror of the Michelson interferometer was moved 6mm at $3\mu\mathrm{ms}^{-1}$. The optical path length (OPL) therefore changed by 12mm, from which a resolution of 25GHz was obtained using

$$\Delta f = \frac{c}{\mathrm{OPL}} = \frac{3 \cdot 10^8 \mathrm{ms}^{-1}}{12\mathrm{mm}} = 25\mathrm{GHz}, \tag{3.8}$$

which follows from the fundamental relation $f = c/\lambda$, or $\triangle f = c/\triangle\lambda$. For the interferometer to measure $\triangle f$, the OPL must be at least $\triangle\lambda$.

The maximum frequency for which the result might be meaningful is one half of the sampling frequency in accordance with the Nyquist criterion:

$$\mathrm{F_s} = \left[\frac{\mathrm{samples}}{\mathrm{meter}}\right]\left[\frac{\mathrm{meters}}{\mathrm{second}}\right] = \frac{55000}{12\mathrm{mm}} \cdot \frac{3 \cdot 10^8 \mathrm{m}}{\mathrm{s}} = 1375\mathrm{THz}, \tag{3.9}$$

$$\mathrm{F_{max}} = \frac{\mathrm{F_s}}{2} = 688\mathrm{THz}. \tag{3.10}$$

From (3.10) it is clear that our 1.89THz frequency of interest would not be hampered by the sampling rate. The precise power spectrum of the globar was not known and was assumed to be uniform. Atmospheric attenuation of the beam was also considered to be uniform. A 103μm (2.91THz) low-pass filter was placed in front of the detector for this and all subsequent measurements. Position and power were recorded as shown in Figure 3.2.

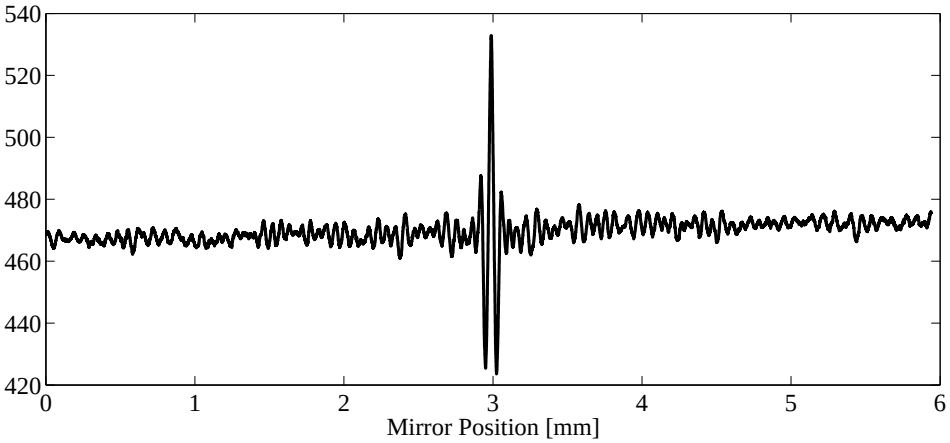

Figure 3.2: Transmission Calibration (Spatial Domain)

The 55000 samples, although somewhat evenly spaced, were not collected at constant distance intervals. To remedy this, the data were re-aligned using linear interpolation before application of a Fast Fourier Transform (FFT). The result is as shown in Figure 3.3.

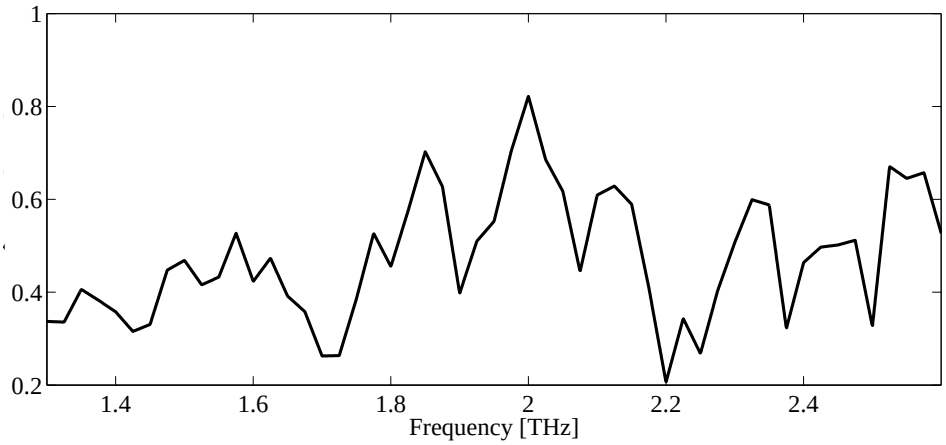

Figure 3.3: Transmission Calibration (Frequency Domain)

A quartz plate of 0.475mm was then placed in front of the detector. Using the same procedure as for the calibration measurements, the power spectrum was found as shown in Figure 3.4.

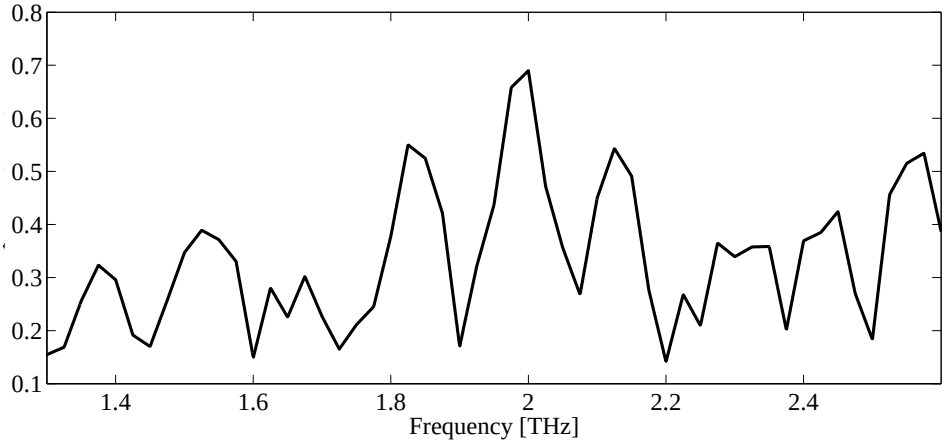

Figure 3.4: Thin Quartz Transmission

Figure 3.5 is a normalized plot created by dividing quartz transmission by empty space transmission. A low-pass filter has been applied to the result.

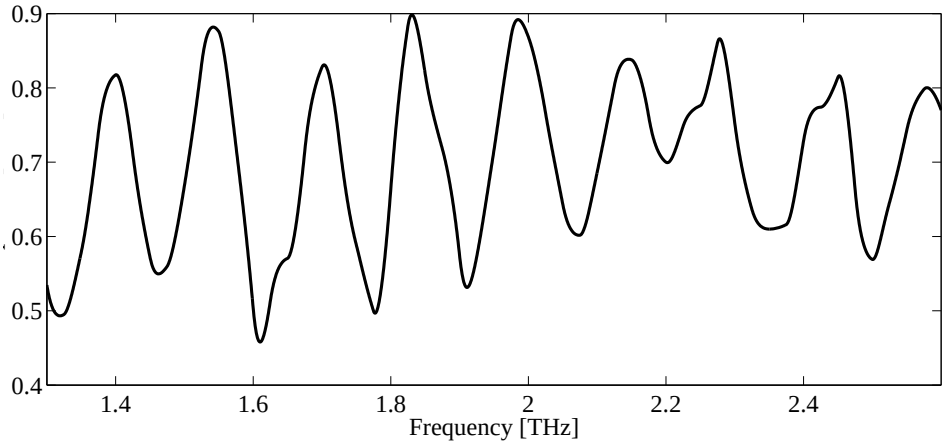

Figure 3.5: Normalized Thin Quartz Transmission

Taking the average spectral distance between amplitude maxima as 147GHz, the quartz thickness is found to be 19.0mil, which is close to the manufacturer specified value of 18.7mil (0.475mm):

$$\Delta f = \frac{2.5795\text{THz} - 1.401\text{THz}}{8\,\text{periods}} = 147\text{GHz}, \tag{3.11}$$

$$T = \frac{c}{2n\Delta f} = \frac{c}{2(2.114)147\text{GHz}} = 0.483\text{mm} = 19.0\text{mil}. \tag{3.12}$$

The spectral waveform of Figure 3.5 does not trend downward like the plot of Figure 3.1. This might be because RIKEN was measuring fused quartz, which is lossier than the single-crystal quartz of our setup.

3.1.3 Quartz of 1.9113mm

The normalized power spectrum for the quartz which would eventually become our sample cover is shown in Figure 3.6.

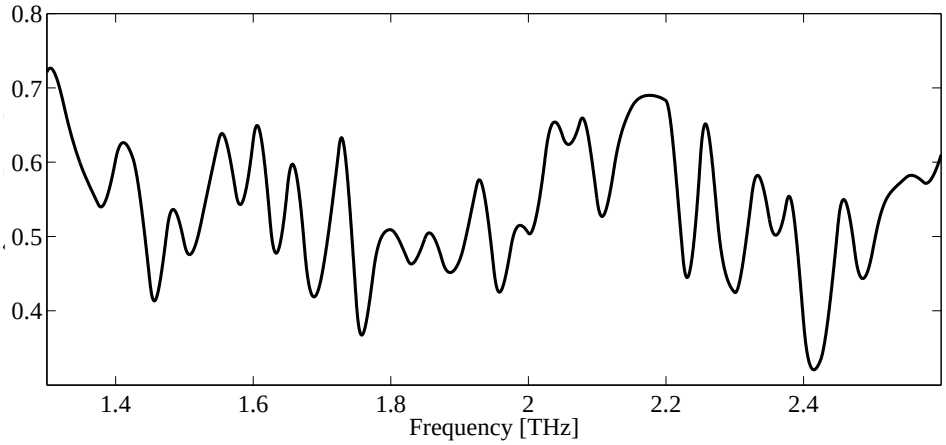

Figure 3.6: Normalized Thick Quartz Transmission

Peaks of Figure 3.6 are not periodic and so T cannot be calculated using our technique. This might be because the system's 25GHz frequency resolution is not small enough, or, equivalently, that the waveform has been effectively undersampled in the frequency domain. Knowing the thickness to be roughly 2mm, the required resolution is

$$\Delta f = \frac{c}{2nT} = \frac{c}{2(2.114)0.002} = 35.5\text{GHz}. \tag{3.13}$$

From (3.13), system resolution should not be a problem. However, true resolution may be higher than 25GHz due to practical considerations such as non-perfect normal incidence of the beam onto the quartz plate, which can produce an effect known as Fabry-Pérot walkoff [Gol98].

3.2 Attenuation Constants from Transmission Measurements

Section 2.4.2 approximates loss tangent as the ratio of imaginary to real dielectric constant according to the values of Bréhat et al. [BW97]. The derivations of this section were created before realizing that refractive index was available in the THz literature as a complex value. In this section, transmission measurements of 1mm quartz, as made available by the RIKEN Tera-Photonics Laboratory in Japan [Lab11], are used

in the derivation of attenuation constants. The RIKEN data is as shown in Figure 3.1 on page 50.

The transmission data were adapted to match input parameters of Agilent ADS software, which accepts an attenuation parameter, α, in dimensions of decibels per meter. This adaptation begins with the complex propagation constant, γ, a solution to the fundamental wave equation:

$$\bigtriangledown^2\bar{\mathbf{E}} - \gamma^2\bar{\mathbf{E}} = 0, \tag{3.14}$$

$$\gamma \equiv \mathrm{j}k = \mathrm{j}\frac{2\pi}{\lambda_{\mathrm{eff}}} = \mathrm{j}\frac{\omega}{v_{\mathrm{p}}} = \mathrm{j}\omega\sqrt{\mu\varepsilon}. \tag{3.15}$$

Real and imaginary parts of permittivity are separated for a refactoring of γ:

$$\varepsilon \equiv \varepsilon' + \mathrm{j}\varepsilon'', \tag{3.16}$$

$$\gamma = \mathrm{j}\omega\sqrt{\mu\varepsilon} = \mathrm{j}\omega\sqrt{\mu}\sqrt{\varepsilon' + \mathrm{j}\varepsilon''} = \mathrm{j}\omega\sqrt{\mu\varepsilon'}\sqrt{1 + \mathrm{j}\frac{\varepsilon''}{\varepsilon'}}. \tag{3.17}$$

$\sqrt{1 + \mathrm{j}\varepsilon''/\varepsilon'}$ may be approximated by the first two terms of its binomial series when $\varepsilon' \gg \varepsilon''$ [Ula01, page 278]. The appropriate binomial series expansion [Coo49] is

$$(1+x)^{\psi} = 1 + \psi x + \frac{\psi(\psi-1)}{2!}x^2 + \ldots \tag{3.18}$$

$$\therefore \left(1 + \mathrm{j}\frac{\varepsilon''}{\varepsilon'}\right)^{\frac{1}{2}} \approx 1 + \left(\frac{1}{2}\right)\left(\mathrm{j}\frac{\varepsilon''}{\varepsilon'}\right) = 1 + \mathrm{j}\frac{\varepsilon''}{2\varepsilon'}. \tag{3.19}$$

The complex propagation coefficient is now segregated into real and imaginary parts where the real part is attenuation constant:

$$\gamma \approx \mathrm{j}\omega\sqrt{\mu\varepsilon'}\left(1 + \mathrm{j}\frac{\varepsilon''}{2\varepsilon'}\right) = \mathrm{j}\omega\sqrt{\mu\varepsilon'} - \omega\sqrt{\mu\varepsilon'}\left(\frac{\varepsilon''}{2\varepsilon'}\right), \tag{3.20}$$

$$\alpha = |\mathrm{Re}\{\gamma\}| \approx \omega\sqrt{\mu\varepsilon'}\left(\frac{\varepsilon''}{2\varepsilon'}\right). \tag{3.21}$$

Refinements are made by substitution of wavenumber, $k_0 = \omega/c$, and refractive index, $n \approx \sqrt{\varepsilon_\mathrm{r}'}$, where $\varepsilon = \varepsilon_\mathrm{r}\varepsilon_0$. Also, for quartz, $\mu \approx \mu_0$:

$$\alpha \approx \omega\sqrt{\mu\varepsilon'}\left(\frac{\varepsilon''}{2\varepsilon'}\right) = \frac{\omega\varepsilon_\mathrm{r}''\varepsilon_0}{2}\sqrt{\frac{\mu_0}{\varepsilon_\mathrm{r}'\varepsilon_0}} = \frac{\omega\varepsilon_\mathrm{r}''}{2}\frac{\sqrt{\varepsilon_0\mu_0}}{\sqrt{\varepsilon_\mathrm{r}'}} = \frac{\omega\varepsilon_\mathrm{r}''}{2c\sqrt{\varepsilon_\mathrm{r}'}} \approx \frac{k_0\varepsilon_\mathrm{r}''}{2n}. \tag{3.22}$$

For non-conducting media, ε_r'' is made to disappear from the formula for α:

$$\tan\delta = \frac{\varepsilon'' + (\sigma/\omega)}{\varepsilon'} \approx \frac{\varepsilon_\mathrm{r}''}{\varepsilon_\mathrm{r}'}, \tag{3.23}$$

$$\varepsilon_\mathrm{r}'' \approx \varepsilon_\mathrm{r}'\tan\delta \approx n^2\tan\delta, \tag{3.24}$$

$$\alpha \approx \frac{k_0\varepsilon_\mathrm{r}''}{2n} \approx \frac{k_0(n^2\tan\delta)}{2n} = \frac{k_0 n}{2}\tan\delta = \frac{\pi}{\lambda_\mathrm{eff}}\tan\delta. \tag{3.25}$$

The solution for loss tangent begins with the characteristic loss equation, where C is field amplitude as a function of z. This is a variation of the Beer-Lambert Law, which states that there is a logarithmic dependence between transmissivity and absorption coefficient:

$$C = C_0 e^{-\alpha z} = C_0 e^{-\left(\frac{\pi}{\lambda_\mathrm{eff}}\tan\delta\right)z}, \tag{3.26}$$

$$\tan\delta = -\frac{\lambda_\mathrm{eff}}{\pi z}\ln\left(\frac{C}{C_0}\right). \tag{3.27}$$

The RIKEN data provides transmittance as a function of wavenumber, κ, requiring conversion from effective wavelength. κ differs by the traditional wavenumber, k, by a factor of $2\pi n$:

$$\kappa \equiv \frac{1}{\lambda_0}, \tag{3.28}$$

$$\lambda_\mathrm{eff} = \frac{\lambda_0}{n} = \frac{1}{n\kappa}. \tag{3.29}$$

Loss tangent may now be expressed with known values, replacing C/C_0 with transmittance, T:

$$\tan\delta = \frac{-\lambda_{\text{eff}}}{\pi z}\ln(T) = \frac{-\ln(T)}{\pi n\kappa z}. \tag{3.30}$$

The attenuation constant has dimensions of [Np/m] but must be [dB/m] for the simulator. The correction constant, as already derived in Section 2.4.2, is

$$D = N\left(\frac{1}{20\log_{10} e}\right). \tag{3.31}$$

The expression for attenuation coefficient in terms of known values is

$$\alpha = \left(\frac{1}{20\log_{10} e}\right)\left(\frac{k_0 n}{2}\right)\left(\frac{-\ln(T)}{\pi n\kappa z}\right)\left[\frac{\text{dB}}{\text{m}}\right] \tag{3.32}$$

$$= \left(\frac{2\pi\kappa n}{40\log_{10} e}\right)\left(\frac{-\ln(T)}{\pi n\kappa z}\right) = \frac{-\ln T}{z\,(20\log_{10} e)}. \tag{3.33}$$

Numerical values may now be assigned to the variables. Quartz is uniaxially anisotropic, meaning that the crystal structure has an axis of symmetry with no equivalent axis in the perpendicular plane. Because of this, parallel and perpendicular components of incident radiation encounter slightly different indices of refraction called ordinary and extraordinary [Nye57]. Typically one would need to consider both refractive indices in an effect known as birefringence. However, by using a narrow incident laser beam parallel to the axis of symmetry (z-direction) of z-cut quartz, we may consider only the ordinary refractive index. According to Bréhat et al., ordinary refractive index for quartz at 1.89THz and 300K is approximately 2.114 [BW97]. At 1.89THz, κ is 63.29cm^{-1} and T is 0.35 when z is 1mm. The loss tangent and attenuation constant may now be evaluated:

$$\tan(\delta) = \frac{-\ln(0.35)}{\pi(2.114)(6329)10^{-3}} = 0.0250, \tag{3.34}$$

$$\alpha = \frac{-\ln 0.35}{10^{-3}\,(20\log_{10} e)} = 121\left[\frac{\mathrm{dB}}{\mathrm{m}}\right]. \tag{3.35}$$

There is a discrepancy between loss tangent as calculated here and loss tangent as calculated in Section 2.4.2. This is likely because the Tera-Photonics Laboratory was measuring fused quartz and Bréhat et al. were measuring single-crystal quartz. Because of the experimental results of Section 3.1, our quartz is believed to be single-crystal.

Loss tangent has been calculated from a single point on the transmission plot. However, (3.30) suggests that the trend of the transmission curve might also yield that information. Transmission may be expressed as an exponential equation, where $b = -\pi n z \tan\delta$:

$$T = A\mathrm{e}^{b\kappa_\mathrm{i}} = \mathrm{e}^{a}\mathrm{e}^{b\kappa_\mathrm{i}}. \tag{3.36}$$

A least squares method may be used to solve for a and b. First, a natural logarithm is applied to both sides:

$$\ln T = a + b\kappa_\mathrm{i}. \tag{3.37}$$

Error is minimized by taking derivatives with respect to a and b:

$$\mathrm{SquaredError} = \sum(\ln T_\mathrm{measured} - \ln T_\mathrm{model})^2 = \sum(\ln T_\mathrm{i} - (a + b\kappa_\mathrm{i}))^2, \tag{3.38}$$

$$\frac{\mathrm{d(SquaredError)}}{\mathrm{d}a} = 2\sum((-1)(\ln T_\mathrm{i} - a - b\kappa_\mathrm{i})) = 0, \tag{3.39}$$

$$\sum \ln T_\mathrm{i} = \mathrm{N}a + b\sum \kappa_\mathrm{i}, \tag{3.40}$$

$$\frac{\mathrm{d(SquaredError)}}{\mathrm{d}b} = 2\sum((-\kappa_\mathrm{i})(\ln T_\mathrm{i} - a - b\kappa_\mathrm{i})) = 0, \tag{3.41}$$

$$\sum \kappa_\mathrm{i} \ln T_\mathrm{i} = a\sum \kappa_\mathrm{i} + b\sum {\kappa_\mathrm{i}}^2. \tag{3.42}$$

Equations 3.40 and 3.42 are combined into a more convenient matrix notation,

$$\begin{bmatrix} a \\ b \end{bmatrix} = \begin{bmatrix} \mathrm{N} & \sum \kappa_{\mathrm{i}} \\ \sum \kappa_{\mathrm{i}} & \sum {\kappa_{\mathrm{i}}}^2 \end{bmatrix}^{-1} \begin{bmatrix} \sum \ln T_{\mathrm{i}} \\ \sum \kappa_{\mathrm{i}} \ln T_{\mathrm{i}} \end{bmatrix}. \tag{3.43}$$

Loss tangent was evaluated using a range of κ for which n would be reasonably constant. We chose to regard n as 2.114 for 50cm^{-1} to 70cm^{-1}. To create numerical data from the RIKEN graph image, software called Engauge Digitizer was used (digitizer.sourceforge.net). a and b were found to be 0.2728 and $-1.978 \cdot 10^{-4}$m. The loss tangent is

$$\tan\delta = \frac{b}{\pi n z} = \frac{-1.978 \cdot 10^{-4}\mathrm{m}}{\pi(2.114)10^{-3}\mathrm{m}} = 0.03. \tag{3.44}$$

This is comparable to the 0.025 loss tangent value from considering transmission at only a single wavenumber.

3.3 Logistics and Practical Medical Sample Concerns

Clinical samples are transported from The University of Massachusetts Medical School (UMMS) in Worcester to UMass Amherst for THz processing while preserved in the cassette of Figure 3.7 and submerged in saline solution. After measurement, the samples are placed once more in the cassette, submerged in formalin, and sent to a laboratory for histological analysis. The sample is generally in saline for 1 or 2 days before measurement. Also, the samples are refrigerated while at UMass Amherst. During measurement, the sample must be in the sample holder of Section 2.5.1 for anywhere from 45 minutes to several hours.

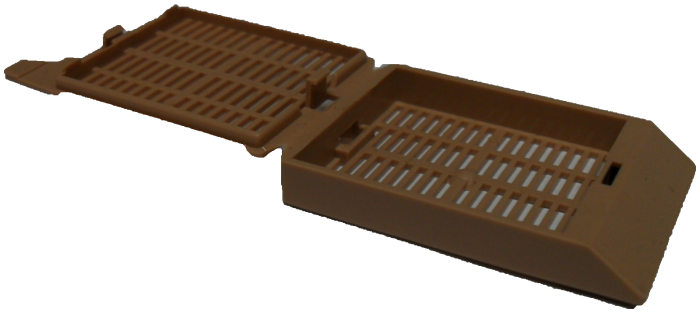

Figure 3.7: Transport Cassette

There are differences between the THz responses of fresh and necrotic tissue as documented by Png et al. [PCN+08]. Two ways of preserving samples without protein fixing are saline submersion and Hank's buffer submersion. Hank's buffer is a glucose-enriched buffer that approximates the environment that tissue would encounter in-vivo. We chose to use saline, which is commonly used at UMMS.

Too much time in saline destroys medical samples. Interestingly, the deterioration seems to happen in two opposite ways. One sample which had been in saline for more than a week turned soft and gelatinous. A similar sample, which had been in saline for the same amount of time, became harder.

One approach to the necrosis and saline problems is preservation of tissue in formalin. Formalin does what is known as cross linking of proteins, which prevents decomposition that could affect THz measurements [BG]. However, analysis of formalin-fixed samples might not be useful in regard to the eventual goal of having an operating room device.

Residual hydration is another concern. Since it is supposed that water is the biomarker, the manner in which samples are handled before THz measurement is crit-

ical to consistent measurement results. This problem is further complicated by the fact that dehydration rates vary according to tissue type, with denser tissues drying more slowly [KSKO+02]. One solution is lyophilization or freeze-drying [PCN+08]. Lyophilization preserves freshness while removing water. However, this would be impractical for the eventual goal of operating room use and difficult or impossible to use with the necessary quartz sample cover.

3.4 Surface Roughness Compensation

Because the system measures reflected power, it cannot distinguish between rough reflective surfaces and flat absorptive surfaces. There must then be some method for eliminating or compensating for surface roughness. Compensation would be difficult because different tissue types generally have different surface textures. We have chosen, instead, to use a flat and rigid cover which is transparent to THz (see Section 2.4).

This section presents a preliminary attempt to compensate for surface roughness using the Ruze equation [Ruz66]. The Ruze equation was originally applied to reflector tolerance theory. In particular, it was meant to model errors introduced by imperfect reflective elements in large antenna structures. To use this model, we consider medical sample surface aberrations as antenna element misalignments. Our application of the Ruze equation is similar to that of Cortés-Medellín and Goldsmith [CMG94] but is simpler because it does not take into account the f-number of the reflector. The Ruze equation is

$$\psi(z) = \psi_0(z) e^{-\xi^2} \left[1 + \frac{\pi \varrho^2}{A_\mathrm{p}} \sum_{n=0}^{\infty} \frac{(\xi^2)^n}{nn!} \right], \tag{3.45}$$

where $\psi(z)$ is aperture efficiency, $\psi_0(z)$ is the aperture efficiency of a perfectly smooth perfect reflector, A_p is the physical aperture of the antenna, ϱ is the correlation of the phase error distribution, ς is root mean square (RMS) height, and ξ is RMS phase error:

$$\xi = \frac{4\pi\varsigma}{\lambda}. \tag{3.46}$$

To test the effectiveness of the Ruze equation for our purpose, we used sandpaper for which surface roughness values were already available from a profilometer application note [Bel10]. The documentation included RMS height values for six different sandpaper grits. Sandpaper industry specifications are defined in ANSI B74.12. Basically, grit number is the number of holes per inch on a sieve. As grit number increases, the surface roughness decreases.

Grit	60	100	120	150	180	220
RMS Height [μm]	83.82	41.05	31.18	22.17	22.49	18.54

Table 3.1: Surface Roughness by Grit

The ratio of ψ to ψ_0 was calculated for each of the sandpaper grits by taking correlation, ϱ, as zero. By doing this, our model became the Kirchoff approximation used by Jagannathan et al., who measured beadblasted metallic surfaces [JGG09].

Measurements were taken of six aluminum slabs which had been abraded with sandpaper. The sandpaper was not measured directly because, with our system in its preliminary state, there was not enough reflected power. One hundred point-measurements were averaged from different locations on the same piece of aluminum. Measurements and calculations were compared as can be seen in Figure 3.8. There is an estimated scaling factor of 4.75 because sandpaper is made of cardboard, adhesive resin, and aluminum oxide rather than the roughened aluminum of our samples.

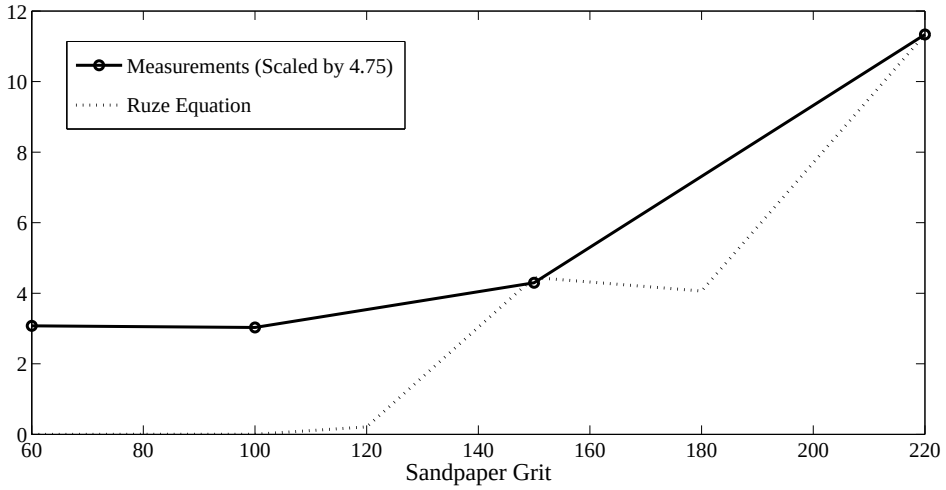

Figure 3.8: Test of Ruze Equation

Another measurement technique would be to deposit a thin layer of metal on the sandpaper surface. This would circumvent the question of whether the roughness of a marred surface is the same as that of the sandpaper used to do the marring.

CHAPTER 4

RESULTS

.

4.1 Non-Medical Samples and Phantoms

Initially, phantom materials allowed for testing and development of the system without using valuable medical samples. Although there is no reliable absolute reflectivity scale for these preliminary measurements, blue corresponds to low reflectivity and red corresponds to high reflectivity.

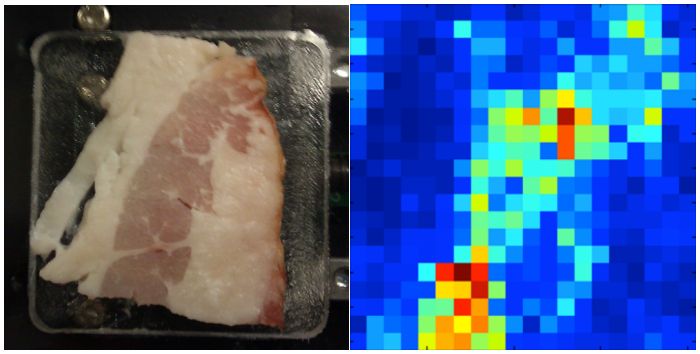

(a) Photo (b) THz

Figure 4.1: Bacon Discrete-Position Measurement

Small reflective markers were sometimes used as spatial registration tools. Below, a small piece of metal has been placed on a slice of sandwich meat. These images also show the white adipose sections reflecting less than the more-fibrous bologna sections.

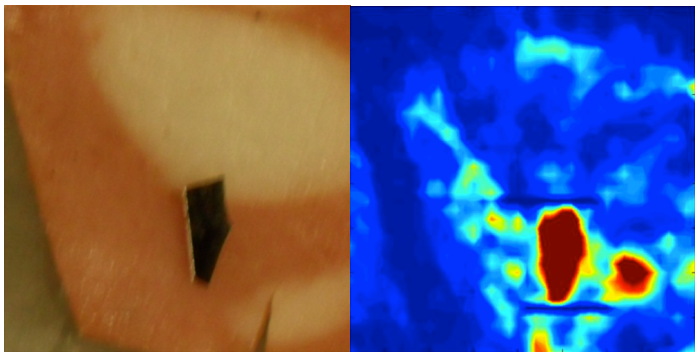

(a) Photo (b) THz

Figure 4.2: Mortadella Continuous-Velocity Measurement

Unsuccessful attempts were made to reproduce the synthetic phantoms described by Sadleir et al. [SNTT09]. Their recipes included the oil-derived TX-151 powder (formerly marketed in putty form as Super Stuff by Wham-O Toys), sucrose, agar, and salt. These phantoms were difficult to work with – drying quickly and changing size and shape as they dried.

4.2 Individual Medical Sample Results

The measurement system has been in a state of evolution throughout the project. THz results for the first four samples were not sufficient to assess cancer detection capability. However, Sample 2 is included in this section to demonstrate a typical preliminary result. It was only after these preliminary samples that the final quartz cover, dual detector setup, and mature calibration and post-processing methods were in-place. Due to problems with the chilled water supply, which is necessary for laser operation, the fifth and sixth samples spent too much time in saline and had to be wasted. Usable results began with the seventh medical sample. Only one side of each specimen received THz and histological analysis.

Sample 7 and all subsequent medical samples contained cancer. Marked and un-

marked histology slides for those samples are available in Appendix D. Image creation techniques are explained in Section 2.10.

4.2.1 Sample 2B

The bolometer was used to detect the THz beam being modulated at 111.4Hz. Continuous-velocity measurements were taken at 1mm/s with a 0.5mm distance interval between rows and a 20ms amplifier time constant. The measurement area is 20mm square. This was the typical configuration for early measurements.

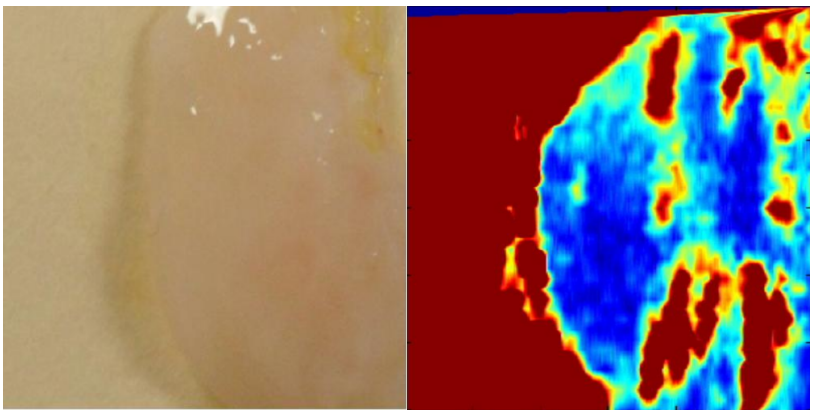

(a) Photo (b) THz

Figure 4.3: Medical Sample 2B

In Figure 4.3, the general sample shape is outlined. Although vertical striations in the THz image may suggest different tissue types, results from this and other early specimens were inconclusive.

4.2.2 Sample 7A

The mean refractive index value of cancerous pixels for Sample 7A was 1.523. From Table 2.3 on page 37, one would expect that value to be higher. One possible explanation is low sample hydration, although no note was taken of the sample being unusually dry. The minimum refractive index of 1, associated with dark blue, corresponds to air under the sample cover.

There are powerful THz reflections along the sample's right edge which do not fully correspond with carcinoma as identified by histologists. Although not easy to see in the optical image, there were strands of dense fibrous tissue throughout that region.

White regions in the optical image of Figure 4.5 are collagenous stroma, which is fibrous and therefore reflects more THz. Figure 4.6 shows that carcinoma is mostly restricted to the collagenous stroma regions.

Yellow regions in the optical image are mostly adipose tissue, which is generally less reflective than fibrous and cancerous tissues. Cancer in the lower-left adipose tissue region was not well-detected by THz, possibly because spatial resolution of the beam was too large.

The ROC plot of Figure 4.7 has a discrimination value of 72%.

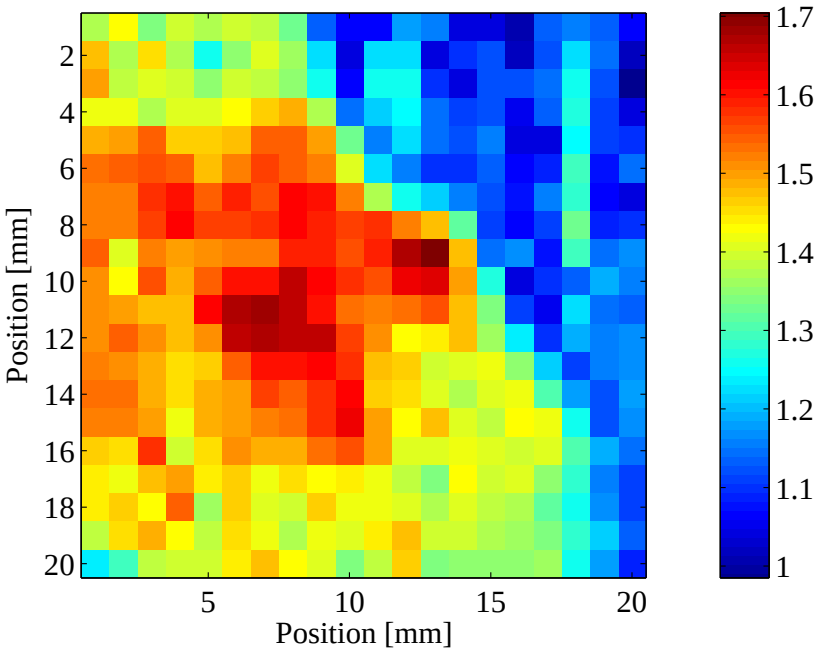

Figure 4.4: THz Image, 7A

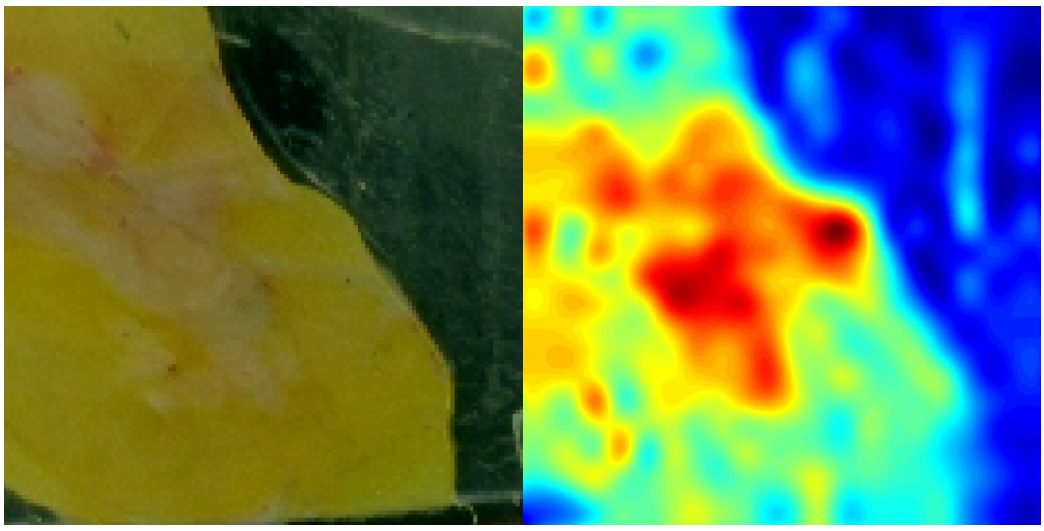

Figure 4.5: Optical and THz Comparison, 7A

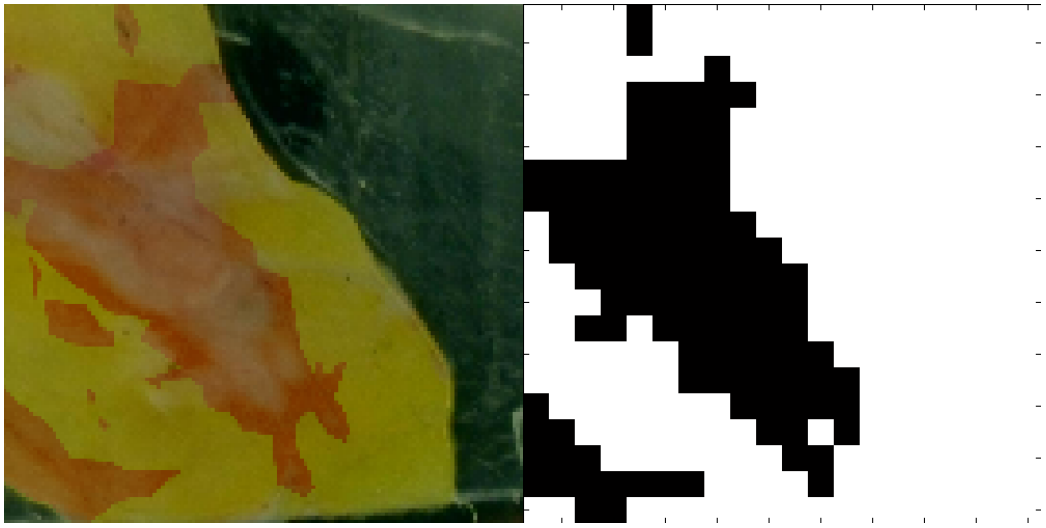

(a) Histology Map (b) Cancer Mask

Figure 4.6: Cancer Locations, 7A

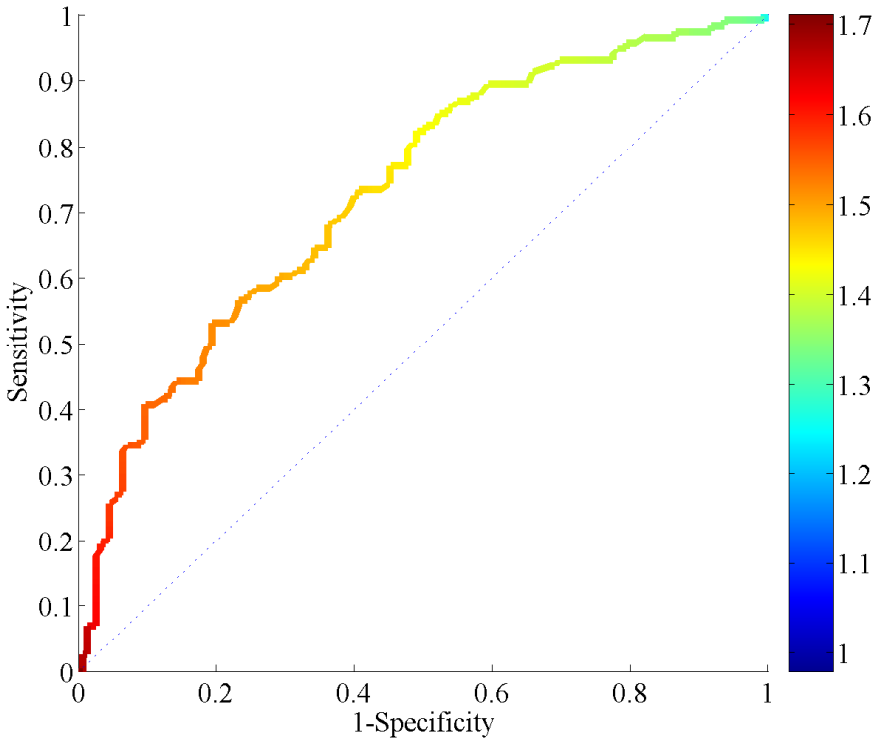

Figure 4.7: ROC colored by $n_{threshold}$, 7A

The discrimination value would have been substantially higher if not for two regions. Sensitivity would have increased if the area marked with A in Figure 4.8 had been identified as cancerous by histology. Likewise, specificity would have increased if the area marked with B in Figure 4.9 had been identified as non-cancerous by histology.

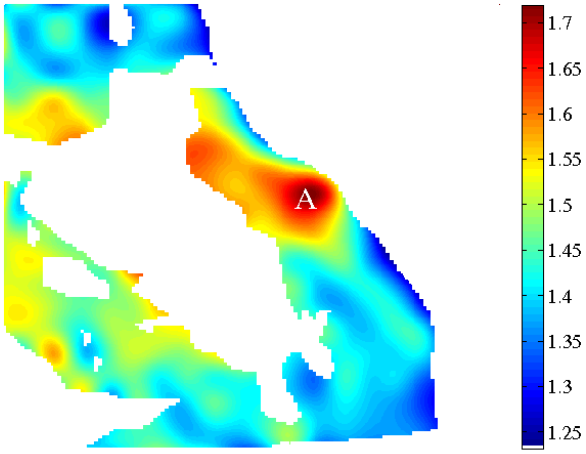

Figure 4.8: Refractive Index of Non-Cancerous Areas, 7A

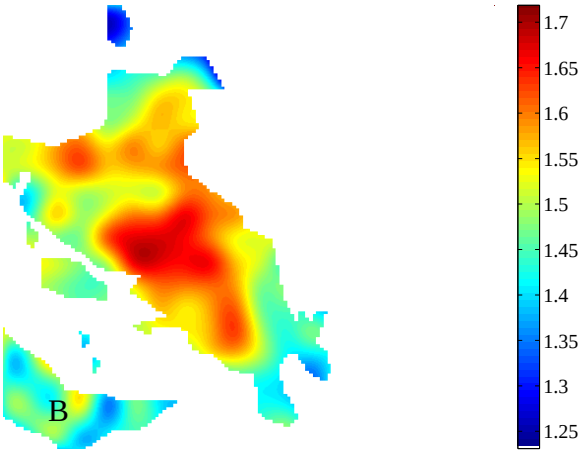

Figure 4.9: Refractive Index of Cancerous Areas, 7A

4.2.3 Sample 8A

The mean refractive index value of cancerous pixels for Sample 8A is 1.705, which is less than that of non-cancerous pixels (1.717).

As can be seen by comparing Figures 4.11 and 4.12, there are many strong THz reflections that do not correspond to carcinoma as identified by histologists.

The discrimination of the ROC plot of Figure 4.13 is 45%, which is roughly equivalent to random guessing. It is unknown why 8A was the only sample to give a discrimination value of less than 70%. One possibility is that the tissues measured by the THz setup were shaved-away during the histological micrograph preparation.

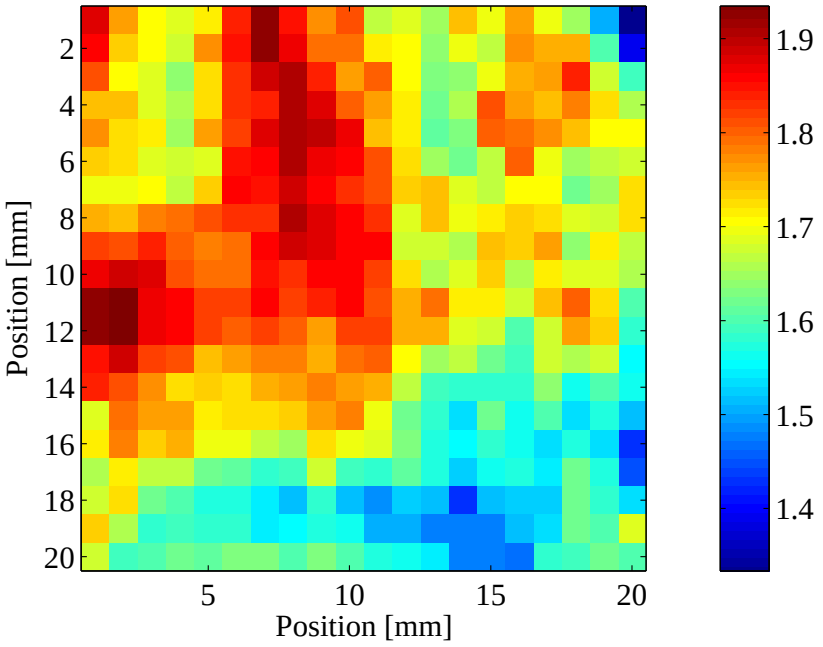

Figure 4.10: THz Image, 8A

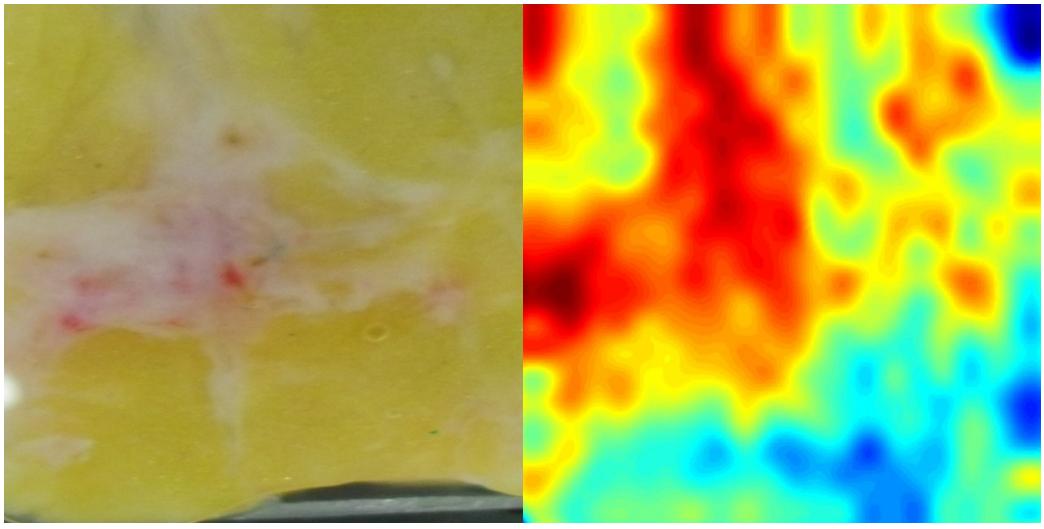

Figure 4.11: Optical and THz Comparison, 8A

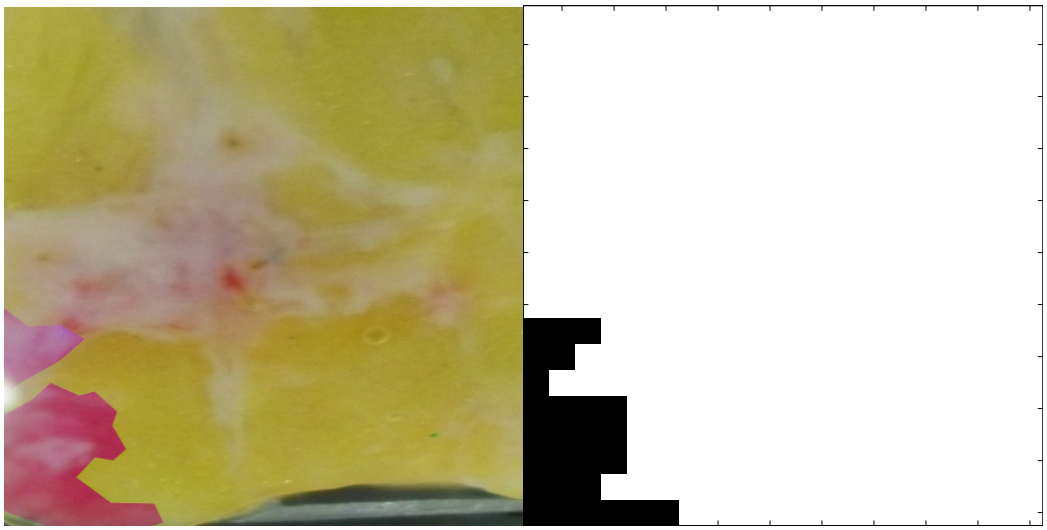

(a) Histology Map (b) Cancer Mask

Figure 4.12: Cancer Locations, 8A

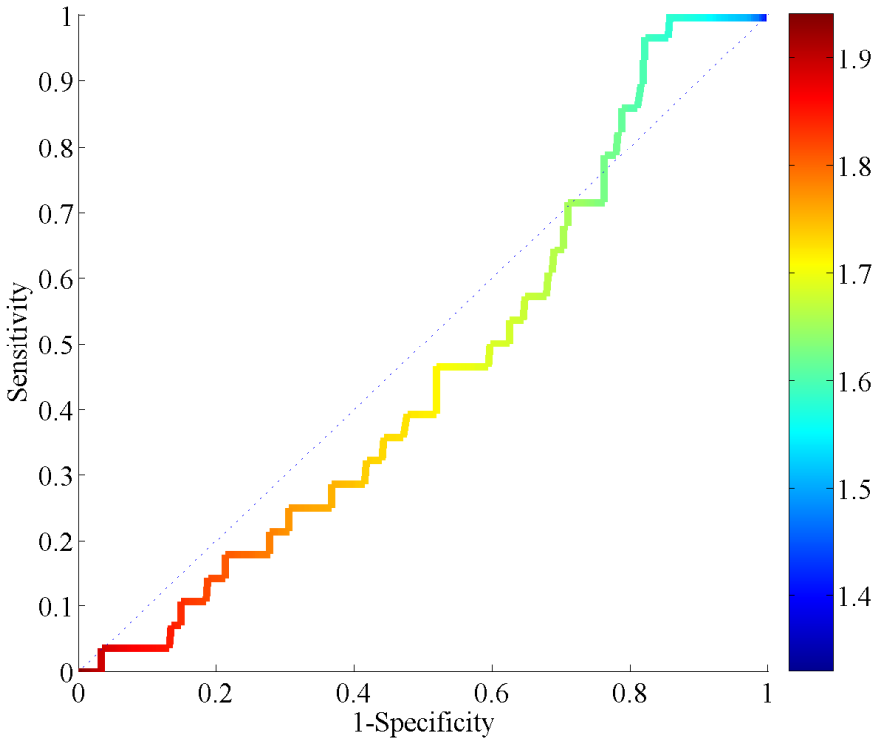

Figure 4.13: ROC colored by $n_{threshold}$, 8A

4.2.4 Sample 9A

As can be seen by comparing Figures 4.15 and 4.16, there are strong THz reflections which do not correspond to carcinoma as identified by histologists, particularly in the upper-right corner. The brown spot in the optical image was highly reflective to THz (see position (16mm, 15mm)) although it was noncancerous. The spot suggests tissue trauma such as a needle biopsy.

White regions in the optical image of Figure 4.15 are collagenous stroma, which is fibrous and therefore reflects more THz. By comparison of the left and right images of that figure, it is clear that THz reflections are high for the collagenous stroma regions, with the exception of a low-reflectivity spot near the center of the carcinoma. It is possible that the sample had peeled away from the sample cover at that location.

Yellow regions in the optical image are mostly adipose tissue, which is generally less reflective than fibrous and cancerous tissues. However, there are strong THz reflections in the adipose region of the upper-right part of the sample. The reason for this is unknown.

The discrimination of the ROC plot in Figure 4.17 is 78%.

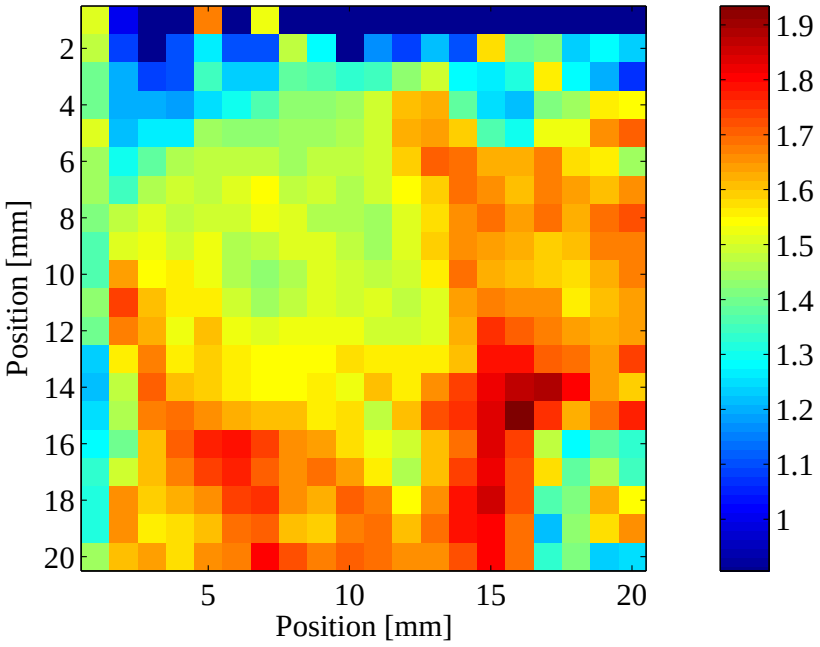

Figure 4.14: THz Image, 9A

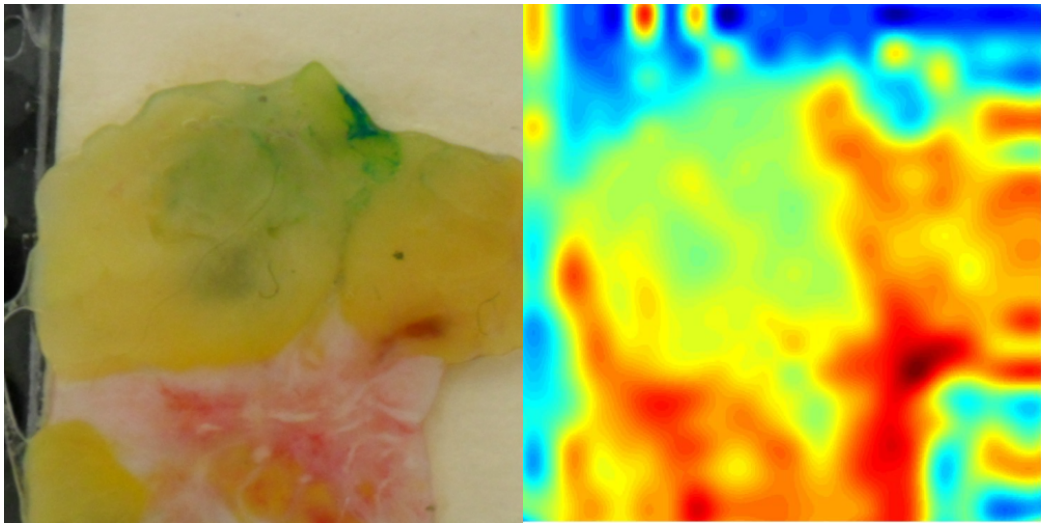

Figure 4.15: Optical and THz Comparison, 9A

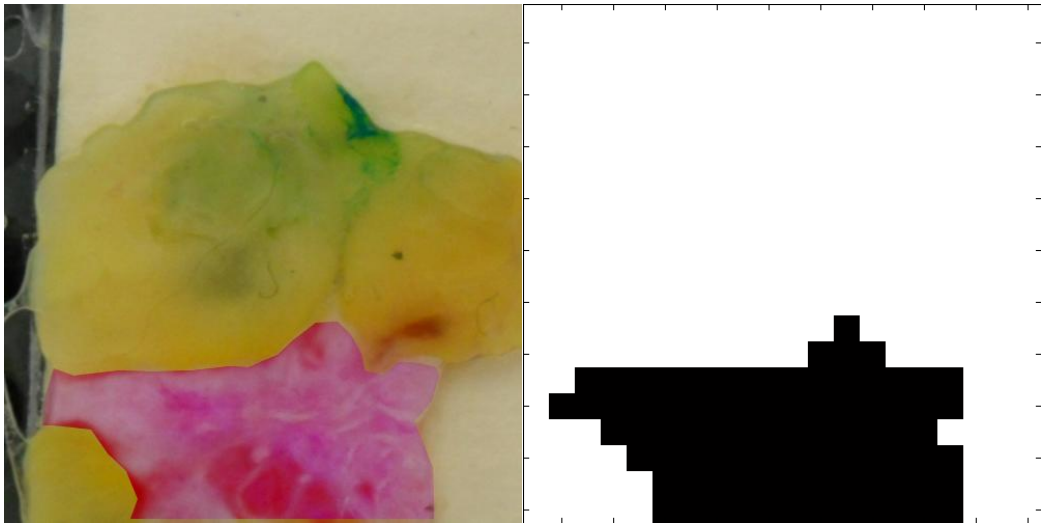

(a) Histology Map (b) Cancer Mask

Figure 4.16: Cancer Locations, 9A

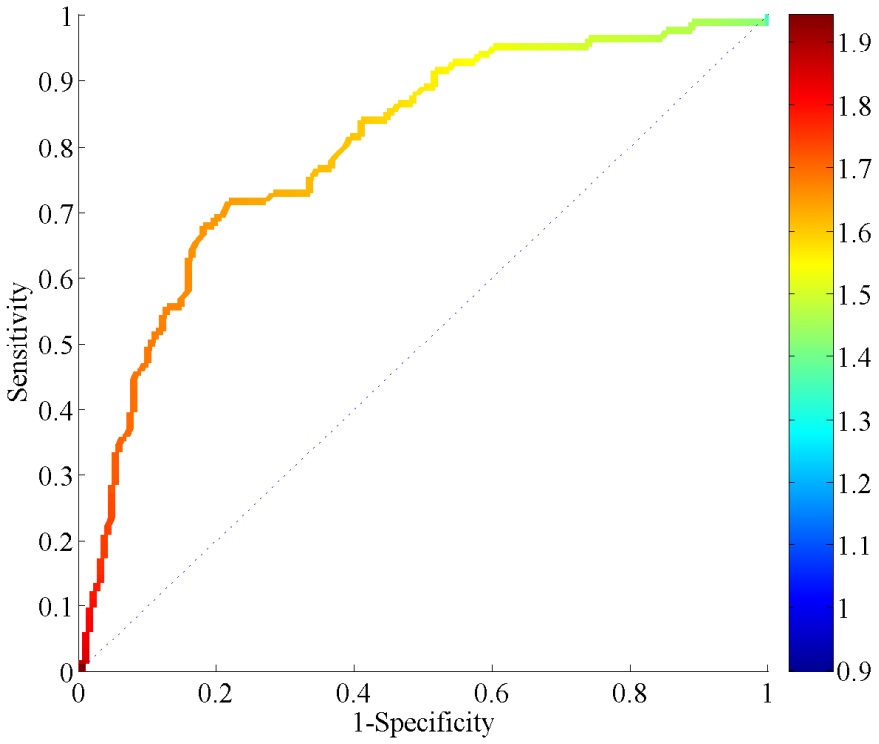

Figure 4.17: ROC colored by $n_{threshold}$, 9A

4.2.5 Sample 10A

The mean refractive index value for the cancerous pixels of Sample 10A is 1.956, which is close to the expected value of 1.97 in Table 2.3.

As shown in Figure 4.19, there are strong THz reflections in the space around the sample. This is probably due to droplets of saline clinging to the underside of the quartz cover. Another possibility might be Fabry-Pérot effects under the cover.

Yellow regions in the optical image are mostly adipose tissue. As expected, adipose regions in the lower-right clearly reflects less THz. However, a significant amount of radiation is reflected from adipose in the lower-left region.

The discrimination of the ROC plot in Figure 4.21 is 76%.

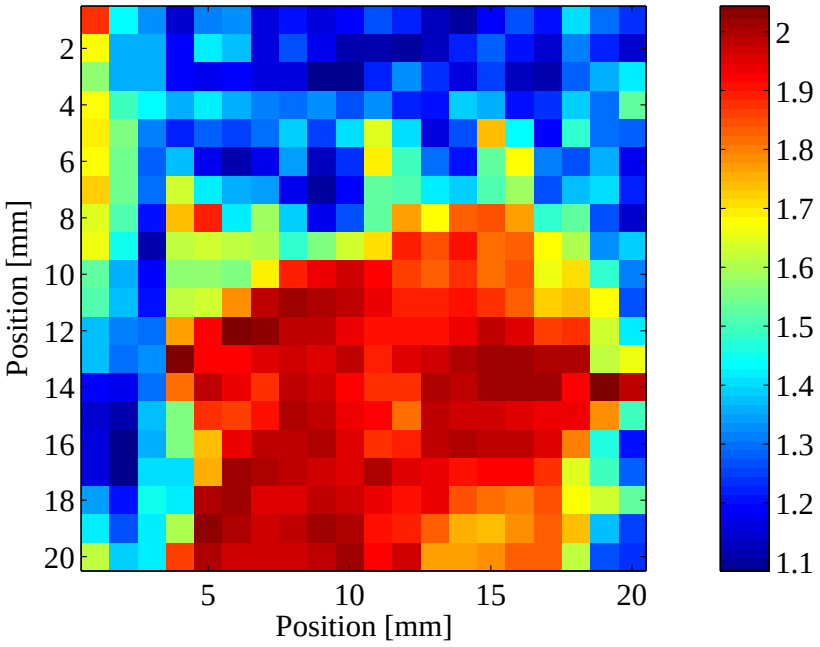

Figure 4.18: THz Image, 10A

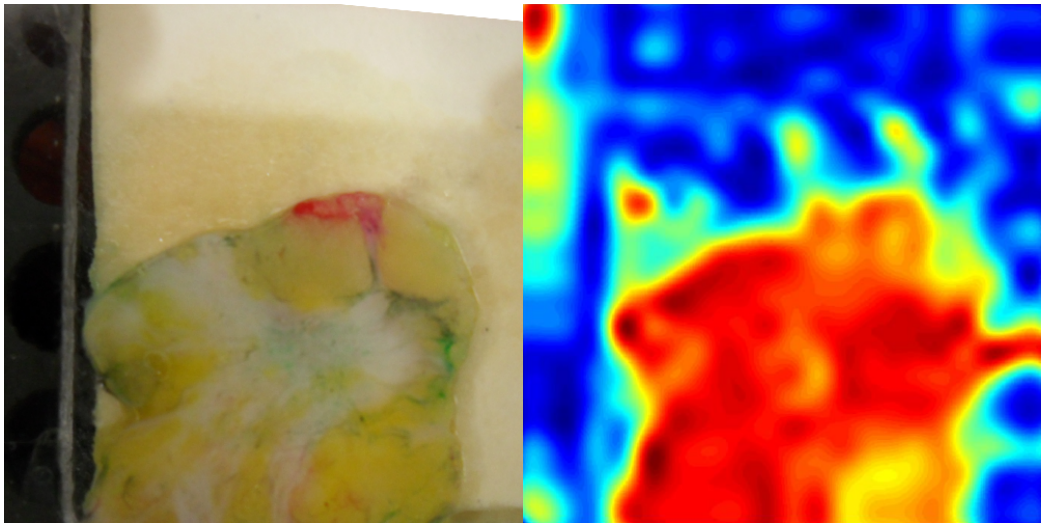

Figure 4.19: Optical and THz Comparison, 10A

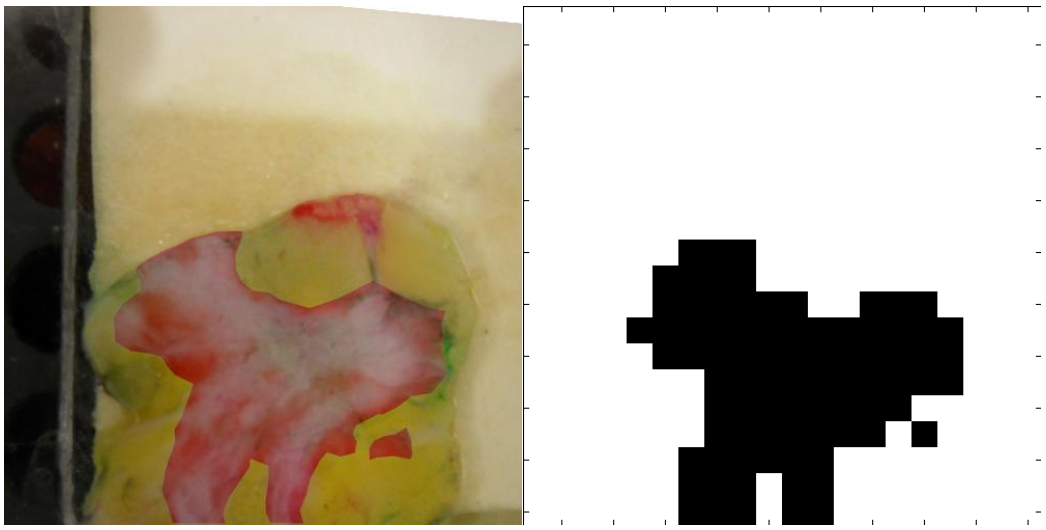

(a) Histology Map (b) Cancer Mask

Figure 4.20: Cancer Locations, 10A

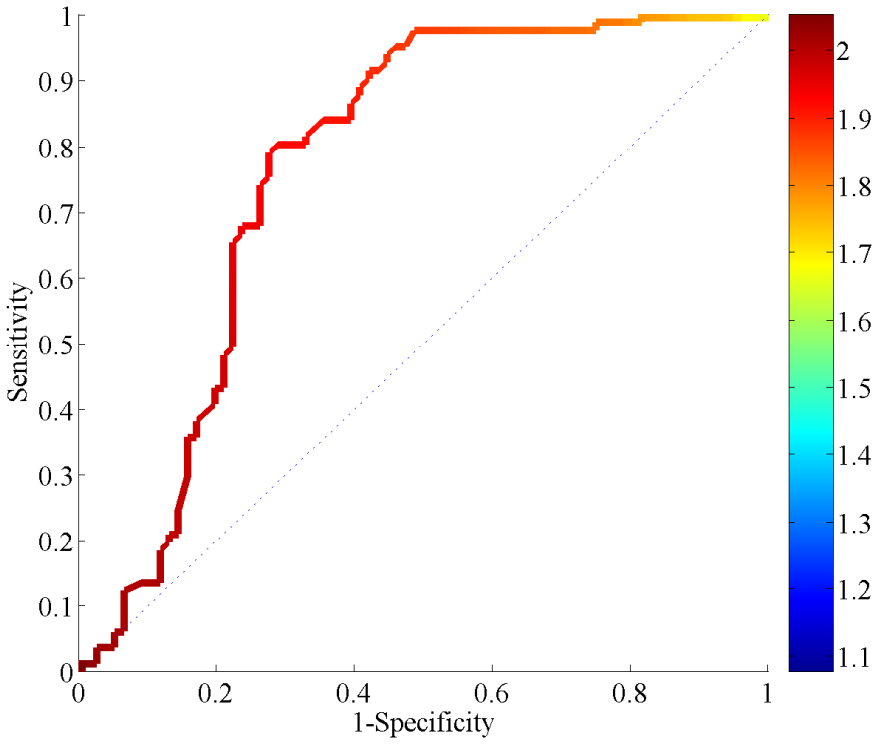

Figure 4.21: ROC colored by $n_{threshold}$, 10A

4.2.6 Sample 11A

Samples 11 and 12, unlike the previous samples, were stored in formalin for about two weeks before imaging.

The THz image, optical and THz comparison, histology map and cancer mask, and ROC for Sample 11A are shown in Figures 4.23, 4.24, 4.25, and 4.26, respectively.

The discrimination of the ROC plot of Figure 4.26 is 71%. This value would have been higher if the region labeled as *A* in Figure 4.22 had been identified as cancerous by histology.

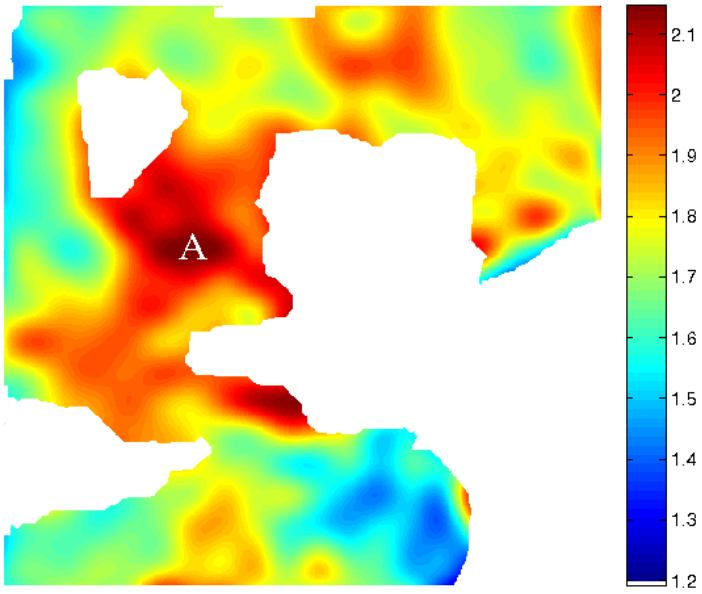

Figure 4.22: Refractive Index of Non-Cancerous Areas, 11A

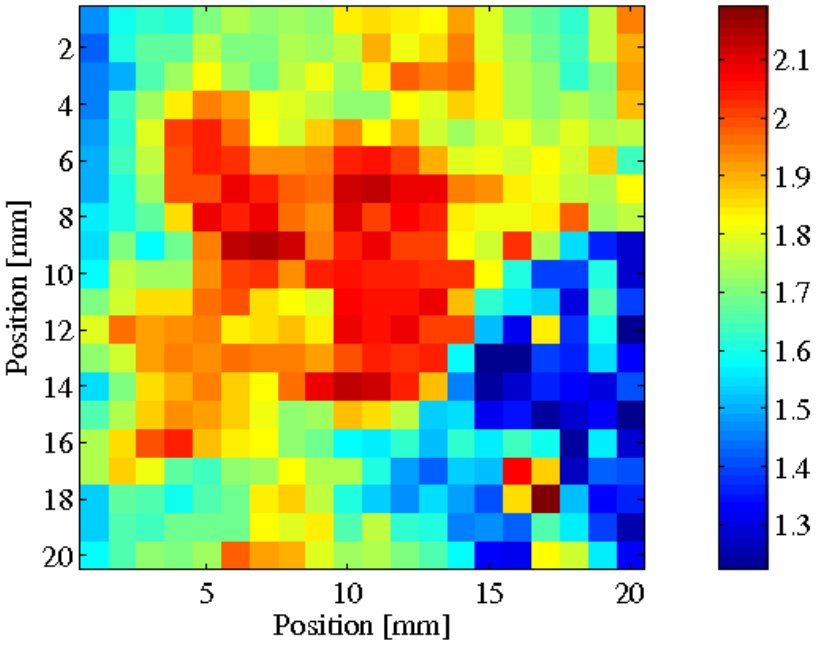

Figure 4.23: THz Image, 11A

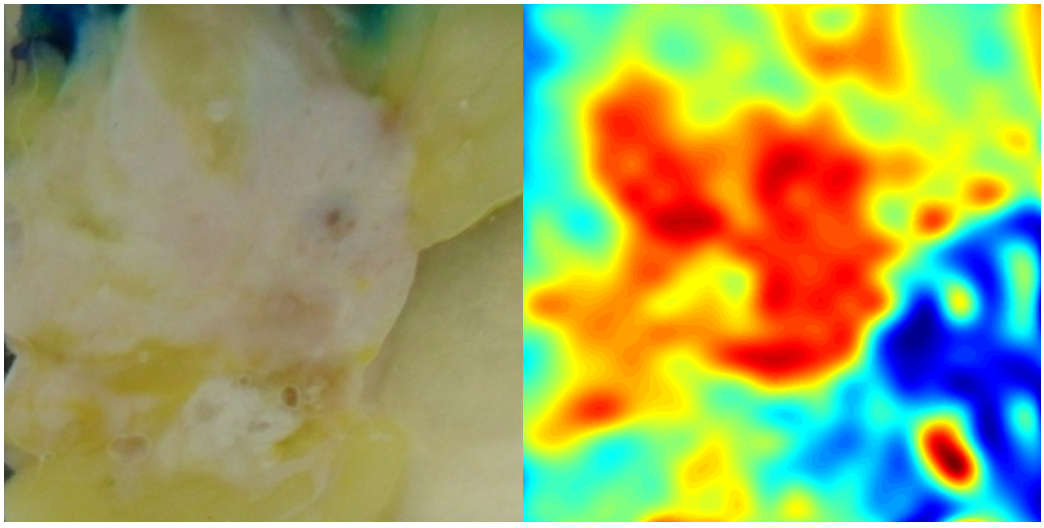

Figure 4.24: Optical and THz Comparison, 11A

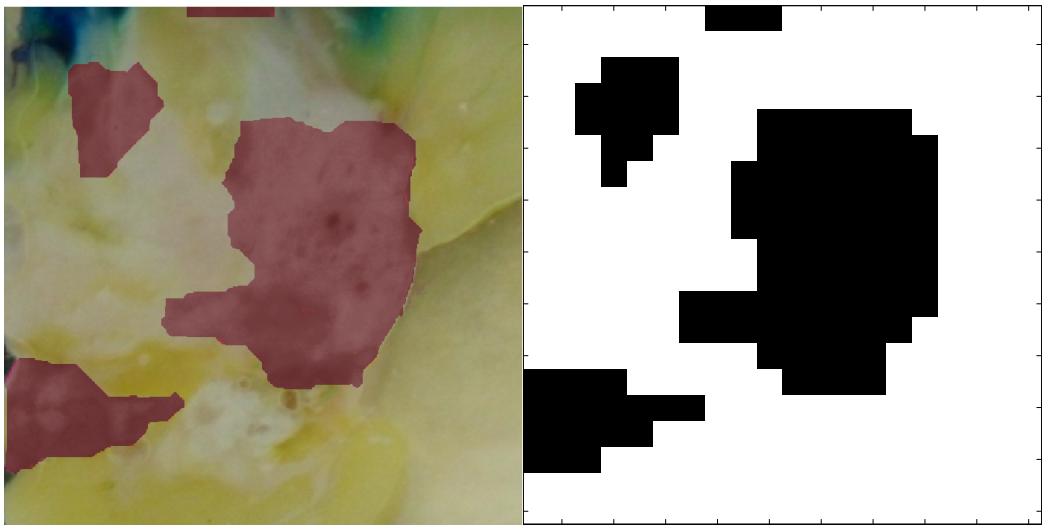

(a) Histology Map (b) Cancer Mask

Figure 4.25: Cancer Locations, 11A

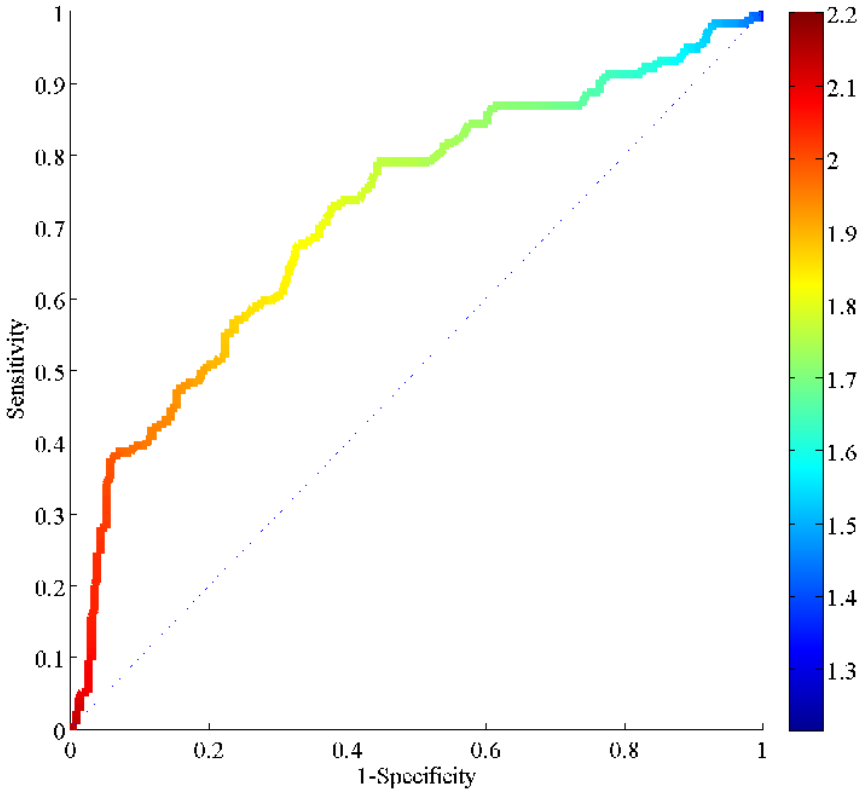

Figure 4.26: ROC colored by $n_{threshold}$, 11A

4.2.7 Sample 12A

The THz image, optical and THz comparison, histology map and cancer mask, and ROC for Sample 12A are shown in Figures 4.27, 4.28, 4.29, and 4.30, respectively.

The discrimination of the ROC plot of Figure 4.30 is 73%.

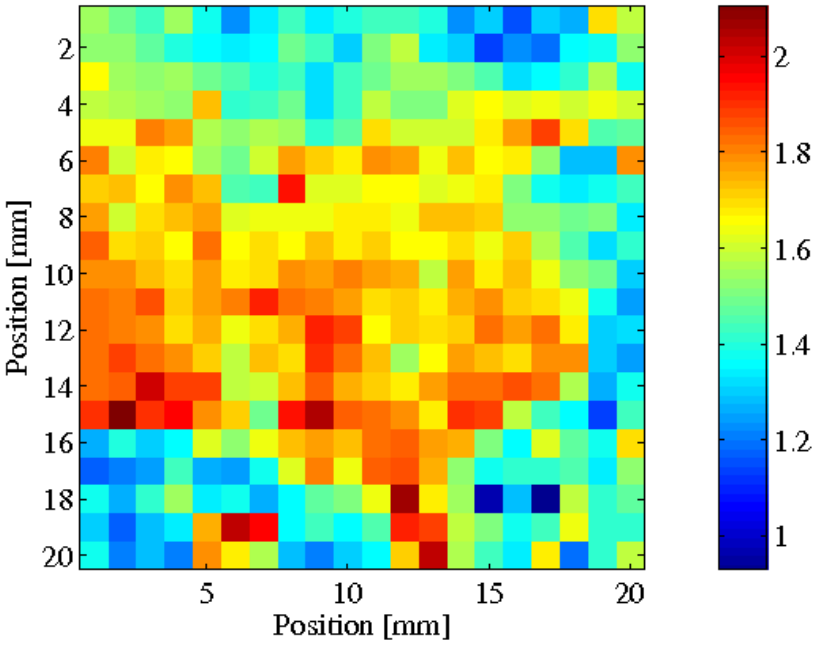

Figure 4.27: THz Image, 12A

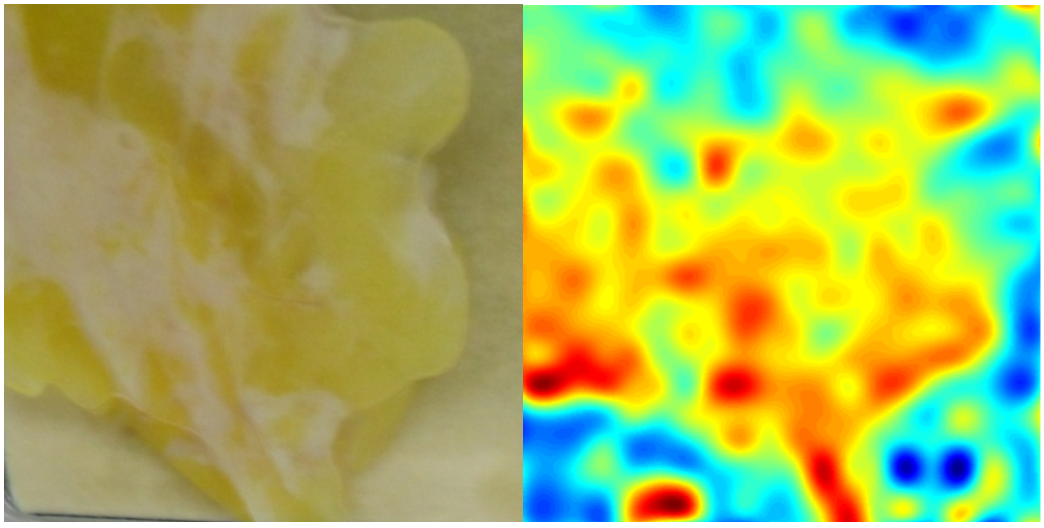

Figure 4.28: Optical and THz Comparison, 12A

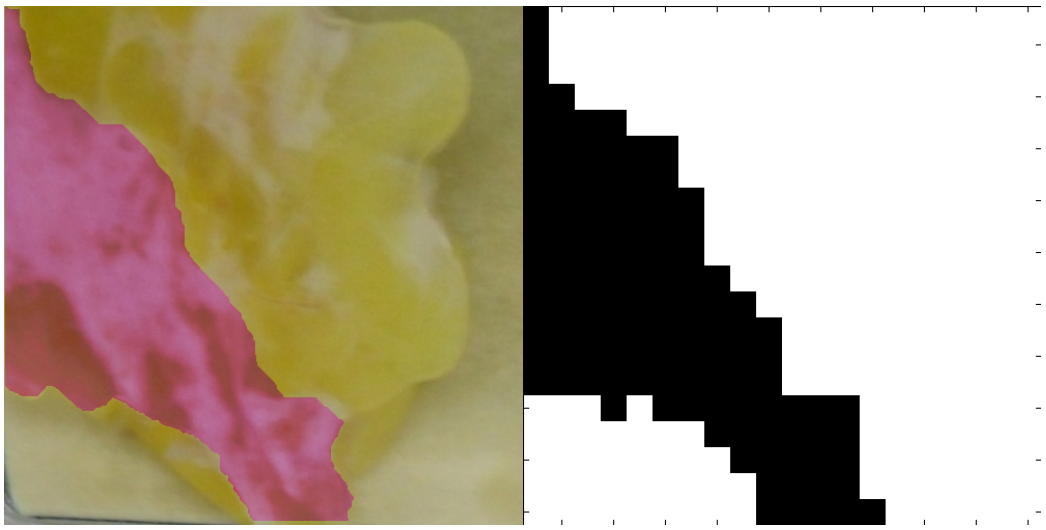

(a) Histology Map (b) Cancer Mask

Figure 4.29: Cancer Locations, 12A

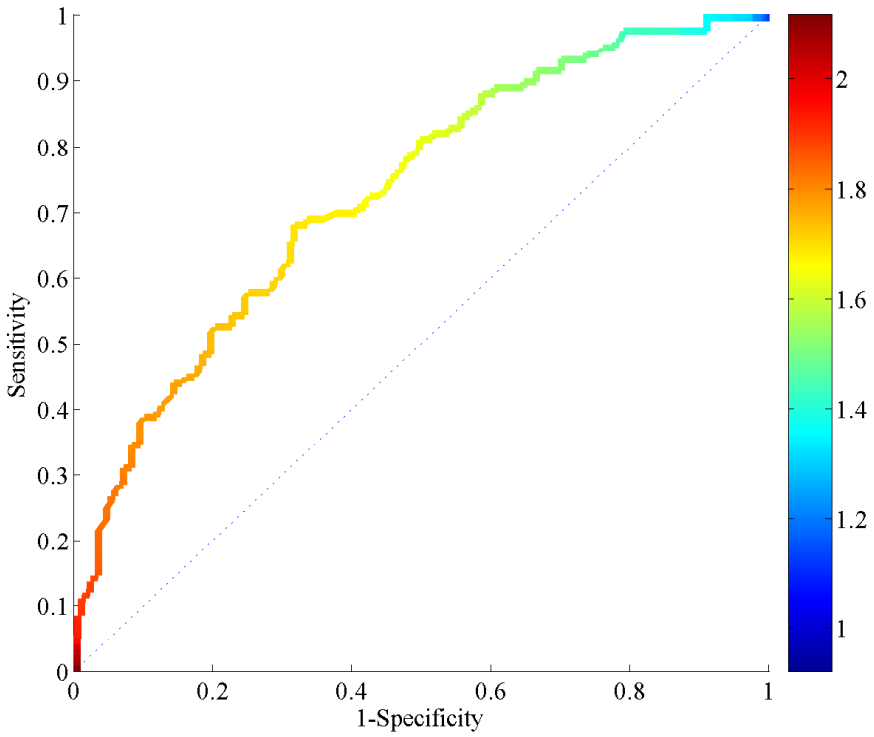

Figure 4.30: ROC colored by $n_{threshold}$, 12A

4.3 Combined Medical Sample Results

A compound ROC was made by using compound refractive index images and masks as shown in Figure 4.31, then using the same post-processing technique for those files as for the individual sample files of the previous section. All medical samples of the previous section were used, excluding the preliminary Sample 2B.

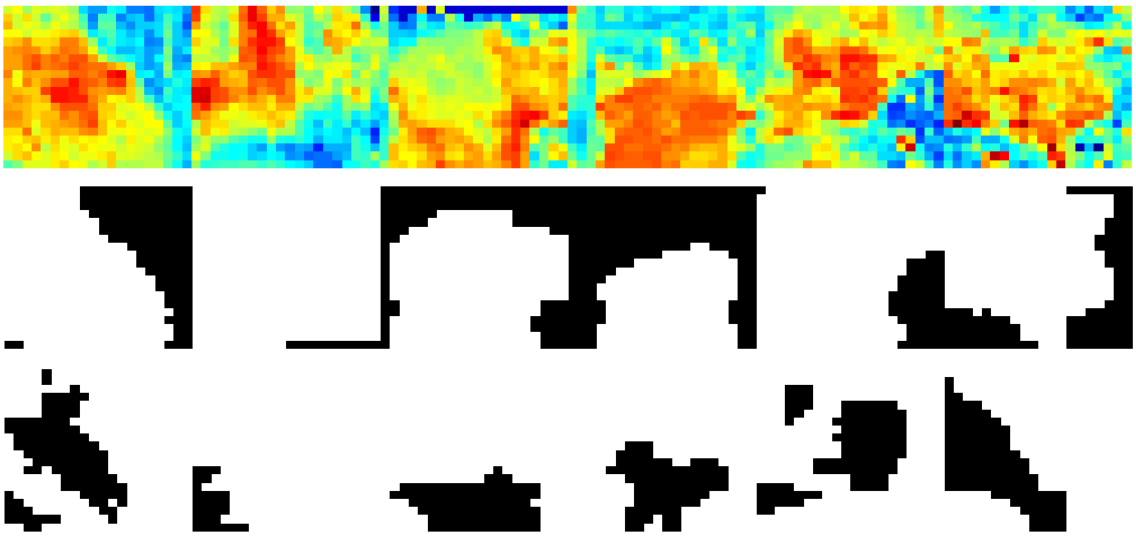

Figure 4.31: Compound Normalized Refractive Index, Off-Sample Mask, and Cancer Mask for Samples 7A, 8A, 9A, 10A, 11A, and 12A

Refractive index was normalized across samples by subtracting respective means and dividing by respective standard deviations. Consequentially, there is no valid refractive index color mapping in the ROC of Figure 4.32. Lack of valid refractive index thresholds across multiple samples is a problem that remains to be solved, as discussed in the Conclusions section.

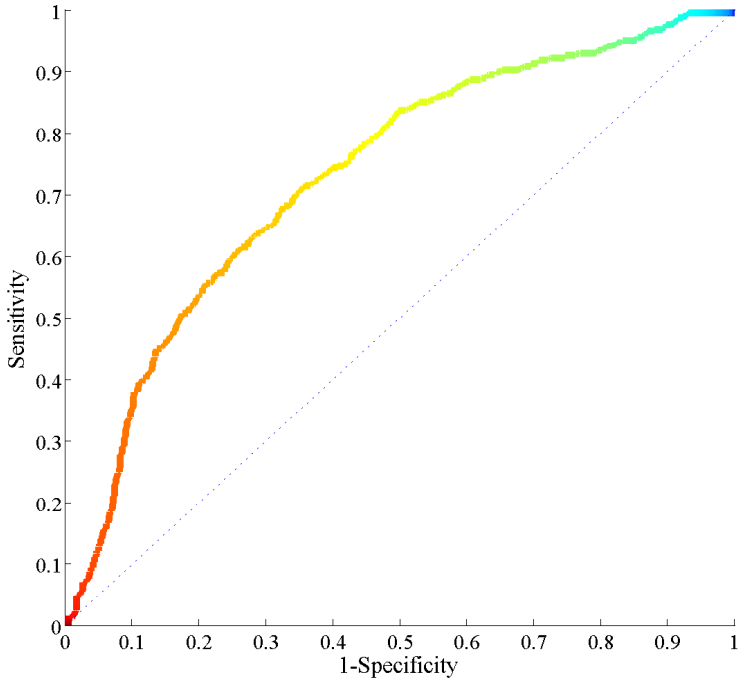

Figure 4.32: Compound ROC (72% Discrimination)

Figure 4.33 illustrates the refractive index range inconsistency by showing the six medical samples and their isolated cancerous regions on the same color scale.

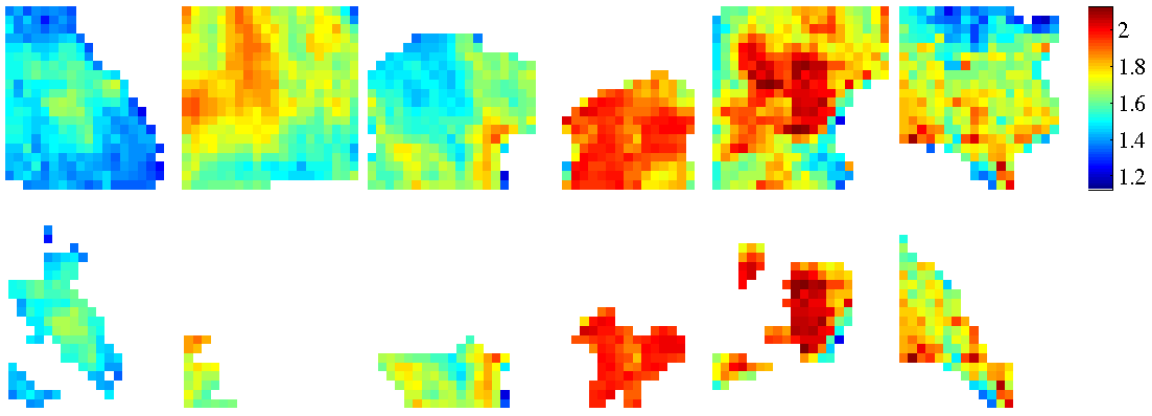

Figure 4.33: Refractive Index Range Inconsistency Across Samples 7A, 8A, 9A, 10A, 11A and 12A (Left to Right)

By collecting the cancerous and non-cancerous pixels from the six normalized images, distributions can be plotted to illustrate the difficulty level with which each pixel may be classified. The probability mass function (PMF) of the combined result is shown in Figure 4.34 and PMF for individual samples are available in Appendix C. Mean values for pixel distributions are in Table 4.1

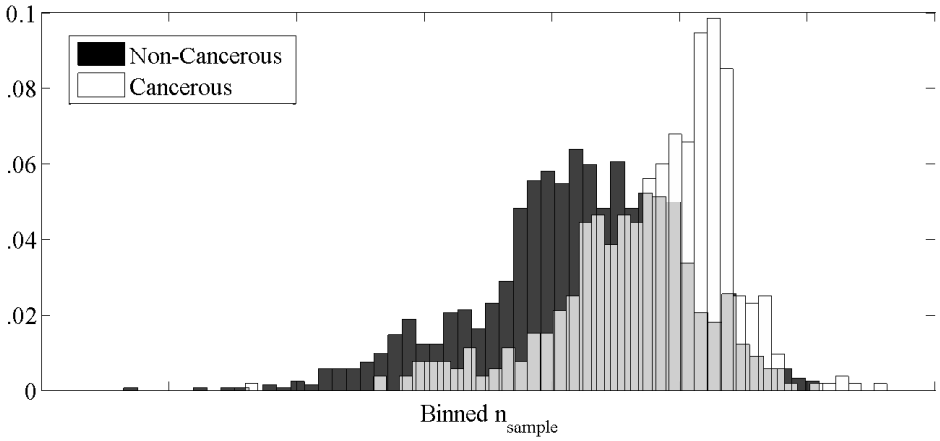

Figure 4.34: Distribution of Cancerous and Non-Cancerous Pixels

Sample	Mean of Cancerous Pixels	Mean of Non-Cancerous Pixels
7A	1.523	1.452
8A	1.705	1.717
9A	1.674	1.572
10A	1.956	1.882
11A	1.912	1.772
12A	1.740	1.614

Table 4.1: Mean Values of Cancerous and Non-Cancerous Pixel Refractive Indices

CHAPTER 5

CONCLUSIONS

5.1 Contributions of this Project

An apparatus has been designed and built which uses power reflectivity measurements at 1.89THz to locate cancer in excised human tissue samples. Using original techniques, this system is able to provide absolute refractive index values of medical specimens. It is hoped that this work will contribute to the long-term goal of helping patients.

5.2 Evaluation of System Capability

One way of summarizing the effectiveness of this imaging setup is with discrimination values from the receiver operating characteristic (ROC) curves as presented in the results section and as summarized in Table 5.1. These values are comparable to the THz imaging results of other researchers [FPP+12]. For clinical usage, our collaborators at the University of Massachusetts Medical School recommend specificity and sensitivity values of at least 90%. This requirement is roughly equivalent to a 90% discrimination value as could be demonstrated with an ROC plot composed of two line segments.

Sample	Discrimination
7A	72%
8A	45%
9A	78%
10A	76%
11A	71%
12A	73%

Table 5.1: ROC Discrimination

Other conclusions that may be drawn from the results section include the following:

1. Refractive index thresholds vary between samples, possibly because the samples weren't handled and prepared identically. However, n_{thresh} was different for 9A and 10A although they were excised together and imaged consecutively. For a 90% sensitivity level, n_{thresh} would be 1.55 for Sample 9A but 1.9 for 10A.

2. The system has trouble identifying cancer in the surface of adipose tissue, as evident from analysis of Sample 7. The solution for this problem is not clear, although making the beam width smaller to find small embedded cancerous regions could be helpful.

3. The system has trouble differentiating carcinoma from benign dense fibrous tissue, as implied by Sample 8 results. This is because, as can be seen in Table 2.3, these tissues have refractive index differences of only a few percent. A solution to this problem might be to increase the signal-to-noise ratio of the system, for which some ideas are presented in Section 5.3.

4. Another complication, evident from analysis of Sample 9, is the false identification of needle biopsy necrotic fat as cancer tissue.

5.3 Future Work Suggestions

Seven suggestions for future work include additional continuous-velocity measurements, quartz surface normalization, polarization measurements, additional phantom experiments, additional measurements of ethanol solutions, measurements at multiple discrete frequencies, and normalization of hydration differences between samples.

1. There are filtering techniques that can use the point spread function (PSF) to improve the THz images, two of which are the Wiener-Kolmogorov and Richardson-Lucy algorithms. These would be especially useful if the current setup were adapted to use the continuous-velocity measurement technique, which could collect thousands of points rather than the current discrete-position measurement grid of 400 points for a 20mm by 20mm sample.

   With the modulation frequency set to 10Hz, there is some doubt as to whether continuous-velocity measurements could be accomplished in a practical amount of time. However, modulation frequency, platform velocity, and time constant could be experimentally adjusted in the mature setup. If necessary, the pyroelectric detector could be replaced with a detector having a faster response. Another possibility is a double modulation scheme in which low and high modulation frequencies, for accommodation of both detectors, would be simultanously present.

2. A technique could be devised for the normalization of potential quartz surface aberrations. Figure 2.10 shows that, at our operating point, a difference of only a few tens of micrometers could significantly effect measurements. Unfortunately, sample cover position and orientation have not been consistent and so this could not easily be retroactively applied.

3. The system might be modified to measure polarization of the reflected beam. This type of work was done at optical frequencies by Patel et al. [PKW+12].

4. It is possible that the TX-151 recipes did not work because the system was in an immature state. This could be revisited.

5. Ethanol and water solutions, each having a known dielectric constant as explained in Section 2.8.2, could be measured for verification or enhancement of the refractive index mapping in Section 2.4.2. Multiple measurements could be made within the medical sample ranges.

6. Measuring samples at multiple discrete frequencies might improve tissue characterisation. Such a multiple parameter space might be conceptually similar to the work of Fitzgerald et al. [FPP+12].

7. The system combines two calibration techniques. Absolute values are found by calibration with a piece of silicon and fluctuations of the laser source are normalized by using two detectors simultaneously. A third calibration scheme might be included to account for hydration differences across samples. This might involve timing various sample preparation phases or somehow measuring sample hydration immediately before THz measurement.

APPENDIX A

MECHANICAL DEFLECTION OF THE SAMPLE COVER

A simple way of providing a value of deflection for the quartz sample cover is to use the 3-point deflection model as illustrated in Figure A.1.

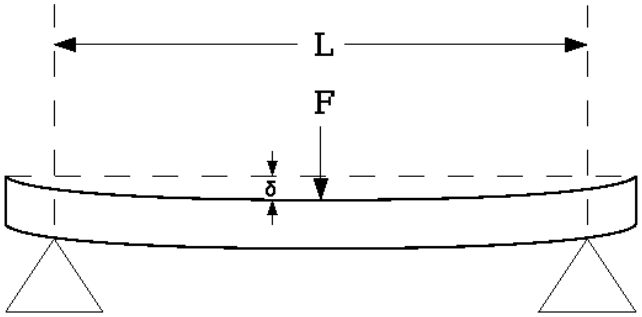

Figure A.1: Three-Point Beam Deflection

The deflection, δ, is

$$\frac{FL^3}{48EI}, \tag{A.1}$$

where F is the applied force, L is the span length of the beam, E is Young's modulus, and I is the beam's moment of inertia [GG11]. The moment of inertia is dependent only upon the dimensions of the beam. For a rectangular beam

$$I = \frac{bh^3}{12}, \tag{A.2}$$

where b is the length of the cross-sectional dimension which is perpendicular to the plane of Figure A.1 and h is the length of the cross-sectional dimension which is vertical in the plane of Figure A.1 [GG11].

For a quartz window of 3cm by 3cm by 2mm, the moment of inertia is $3\text{cm}(2\text{mm})^3/12 = 2.00 \cdot 10^{-11}\text{m}^4$. The Young's modulus of quartz is roughly $70 \cdot 10^9 \text{kgm}^{-1}\text{s}^{-2}$. Equation A.1 can be rearranged to express the applied force which would be required for a deflection of 1μm:

$$F = \frac{\delta 48EI}{L^3} = \frac{(1\mu\text{m})48(70 \cdot 10^9 \text{kgm}^{-1}\text{s}^{-2})(2 \cdot 10^{-11}\text{m}^4)}{(3\text{cm})^3} = 2.5\text{N}. \tag{A.3}$$

APPENDIX B

PRELIMINARY SIMULATOR

To calculate attenuation as a function of distance below a surface, a model based on transmission line equations was created. Figure B.1 can be considered as a transmission line with the input at the bottom and a load at the top. Whether the input is considered to be at the top or bottom is inconsequential because of the reciprocity theorem [Har01].

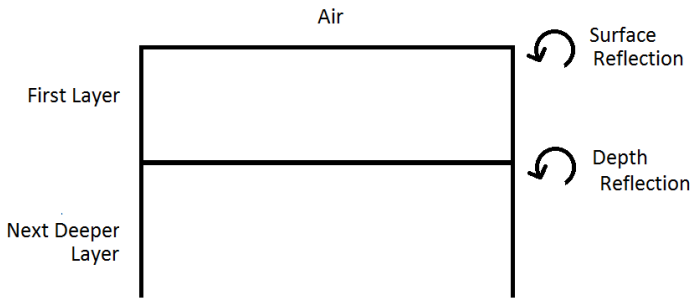

Figure B.1: Transmission Line Model

The characteristic impedance, Z, of the load and each layer must be calculated from material parameters:

$$Z = \frac{\mathrm{j}\omega\mu}{\gamma}[\text{Poz05, eqn 1.102}], \tag{B.1}$$

$$\gamma = \mathrm{j}\omega\sqrt{\mu\varepsilon}\sqrt{1 - \mathrm{j}\frac{\sigma}{\varepsilon\omega}}[\text{Poz05, eqn 1.60}]. \tag{B.2}$$

If conductance can be approximated as zero, impedance is

$$Z = \sqrt{\frac{\mu}{\varepsilon}}. \tag{B.3}$$

Since the load is at the top, Z_{L} is the impedance of air, which is approximately the impedance of free space:

$$Z_{\mathrm{L}} = \sqrt{\frac{\mu_0}{\varepsilon_0}}. \tag{B.4}$$

The impedance of the first layer, Z_0, can be calculated from (B.3). Knowing Z_{L} and Z_0, field reflection coefficient for the *Surface Reflection* is

$$\Gamma_{\mathrm{surface}} = \frac{Z_{\mathrm{L}} - Z_0}{Z_{\mathrm{L}} + Z_0}. \tag{B.5}$$

Field reflection coefficient can be expressed as a function of distance, z, below the surface:

$$\Gamma(z) = \Gamma_{\mathrm{surface}} e^{-2\gamma z} [\mathrm{Poz05, eqn\,2.90}]. \tag{B.6}$$

Using (B.6), input power may also be expressed as a function of z:

$$P_{\mathrm{in}} = \frac{|V_0^+|^2}{2Z_0} \left(1 - |\Gamma(z)|^2\right) e^{2\alpha z} [\mathrm{Poz05, eqn\,2.92}]. \tag{B.7}$$

Power gain is the ratio of input power at the surface to input power at any particular depth. For example, if thickness of the first layer were ℓ, power gain at the interface between the first and second layers would be

$$G_{\mathrm{power}} = \frac{\frac{|V_0^+|^2}{2Z_0}\left(1 - |\Gamma(0)|^2\right) e^{2\alpha 0}}{\frac{|V_0^+|^2}{2Z_0}\left(1 - |\Gamma(\ell)|^2\right) e^{2\alpha \ell}} = \left(\frac{1 - |\Gamma_{\mathrm{surface}}|^2}{1 - |\Gamma(\ell)|^2}\right) e^{-2\alpha\ell}. \tag{B.8}$$

Input impedance at the interface of the first and second layers would become the new load impedance. Impedance of the second layer would become the new Z_0:

$$Z_{\mathrm{LnextIteration}} = Z_{\mathrm{in}} = Z_0 \left(\frac{Z_{\mathrm{L}} + Z_0 \tanh(\gamma\ell)}{Z_0 + Z_{\mathrm{L}} \tanh(\gamma\ell)}\right), \tag{B.9}$$

$$Z_{0\mathrm{nextIteration}} = \sqrt{\frac{\mu_{\mathrm{nextDeeperLayer}}}{\varepsilon_{\mathrm{nextDeeperLayer}}}}. \tag{B.10}$$

This process could iterate for any number of layers.

APPENDIX C

REFRACTIVE INDEX DISTRIBUTIONS

This section contains probability mass functions (PMF) for the cancerous and non-cancerous refractive indices of each medical result.

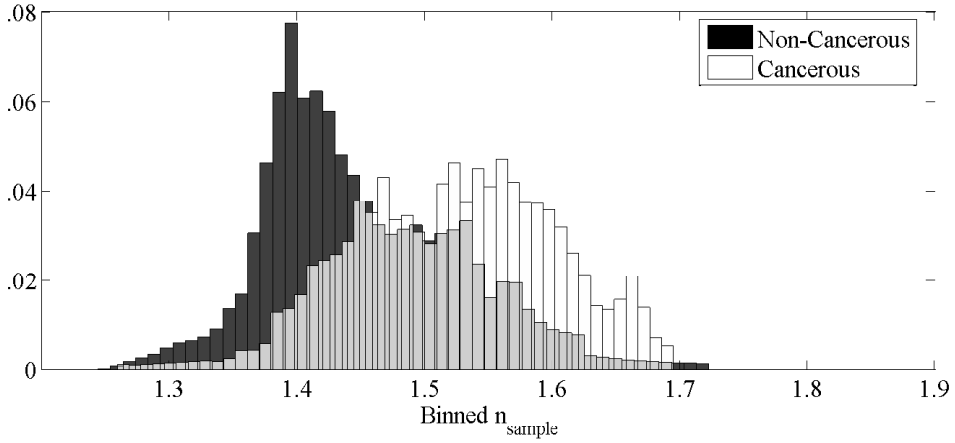

Figure C.1: Probability Mass Function, 7A

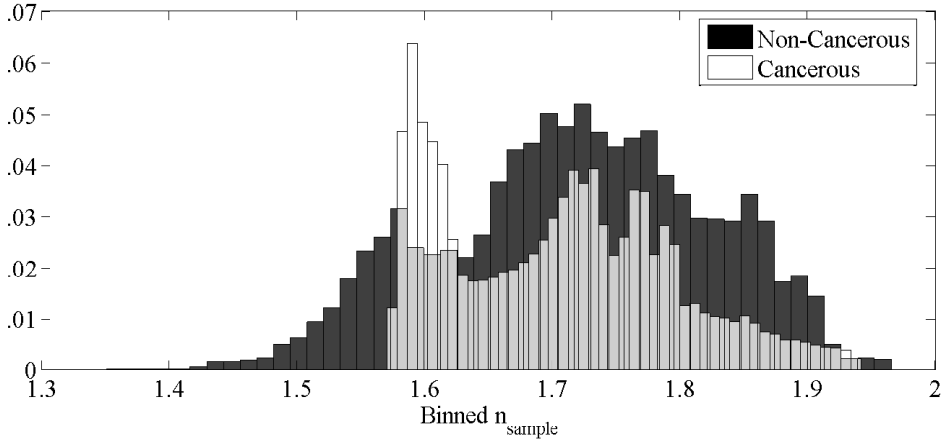

Figure C.2: Probability Mass Function, 8A

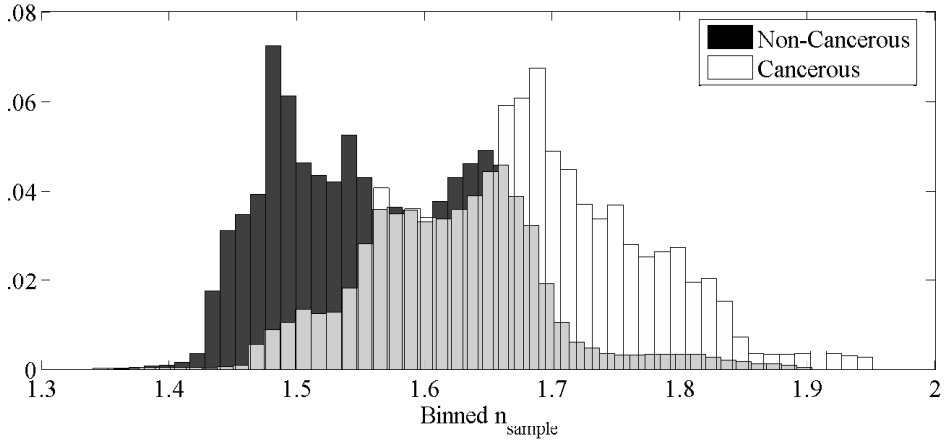

Figure C.3: Probability Mass Function, 9A

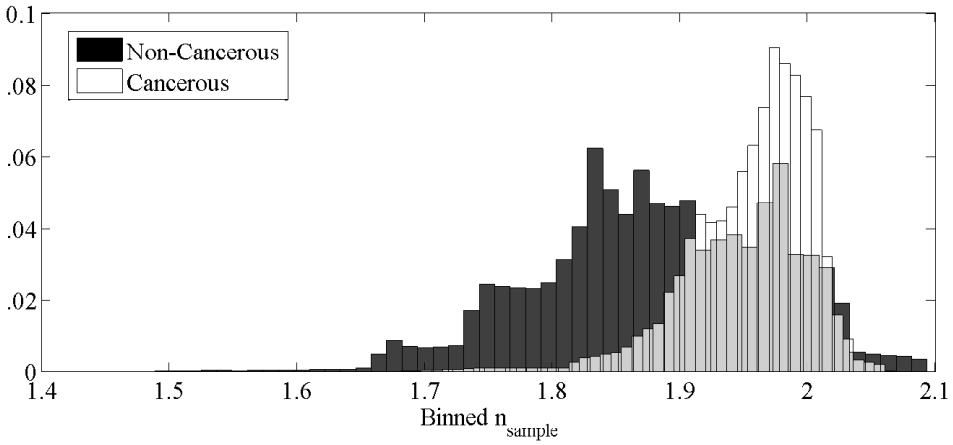

Figure C.4: Probability Mass Function, 10A

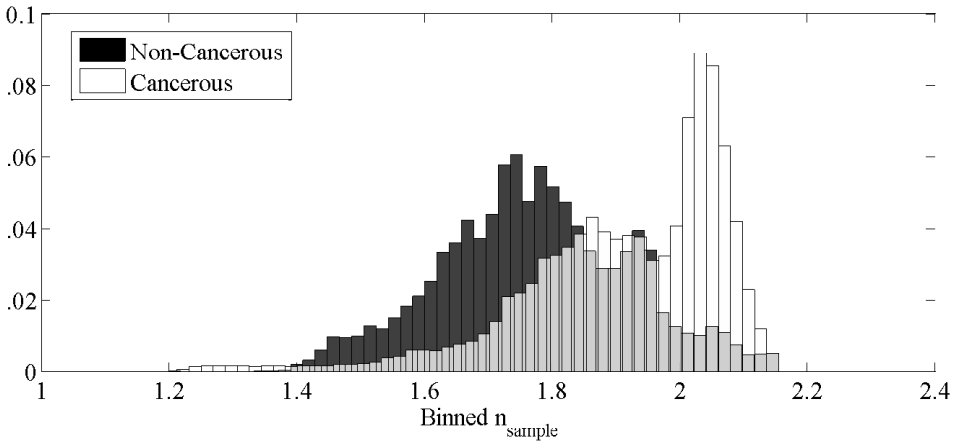

Figure C.5: Probability Mass Function, 11A

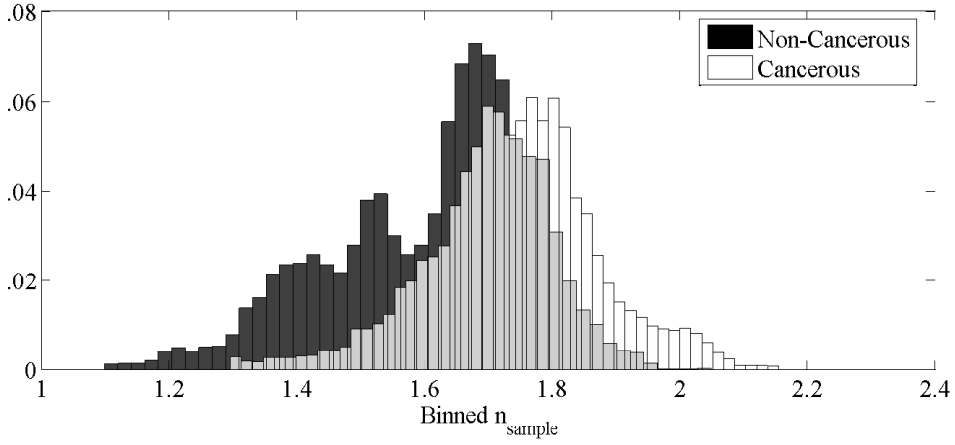

Figure C.6: Probability Mass Function, 12A

APPENDIX D

HISTOLOGY SLIDES

This section contains large-scale histology slides. White areas generally indicate fatty regions. Cancer cells are blue as a result of a process incorporating hematoxylin and eosin dyes, which bind based on tissue pH levels [Hol12]. Traces of green dye are remnants of marker ink and have nothing to do with tissue type. Each of these samples contains carcinoma which is outlined in the marked images. Some slides also have outlines around the entire sample, which are meant to mark the sample boundary and not a cancerous region.

Figure D.1: 7A Histology Slide

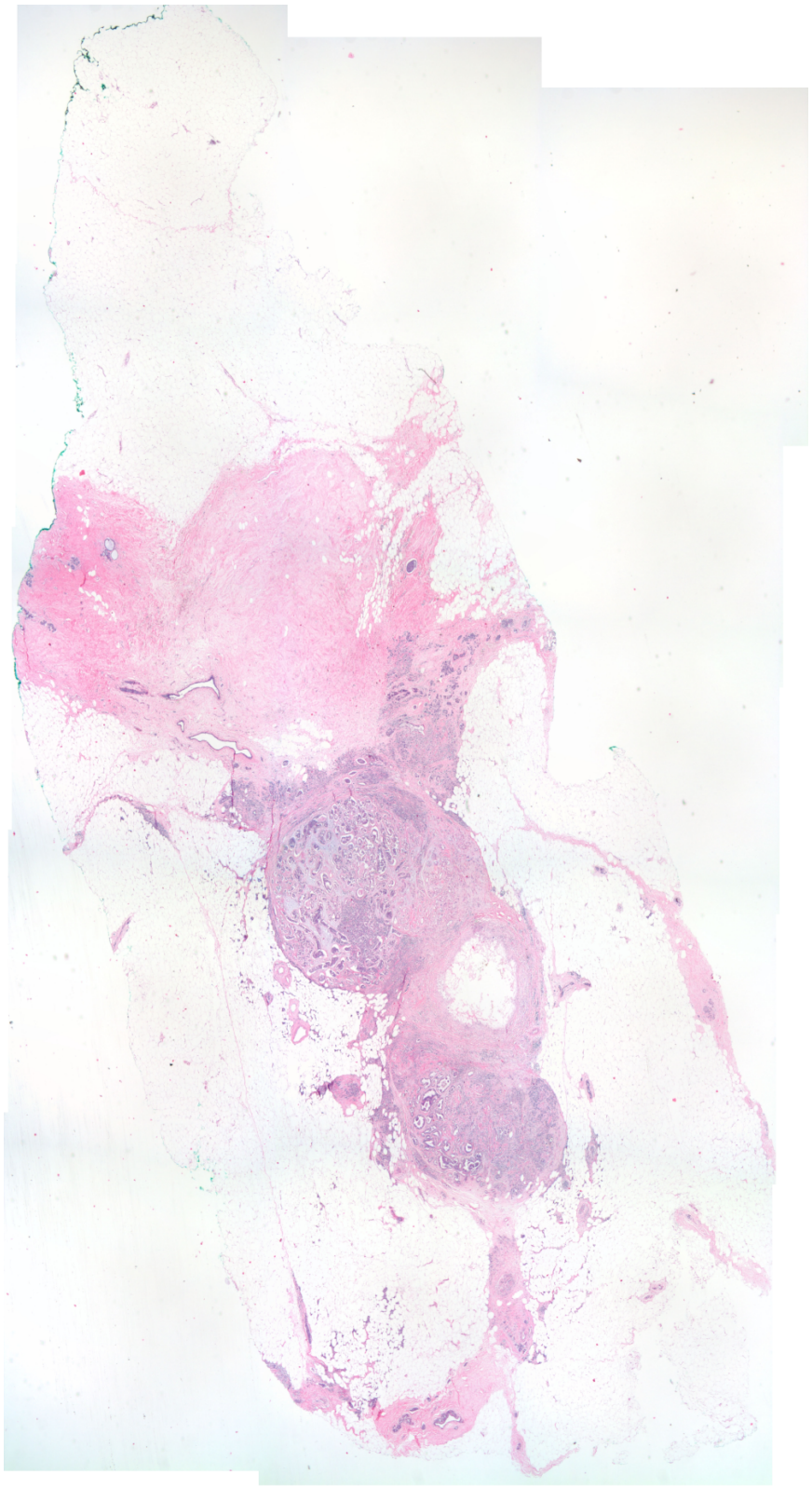

Figure D.2: 7A Marked Histology Slide

Figure D.3: 8A Histology Slide

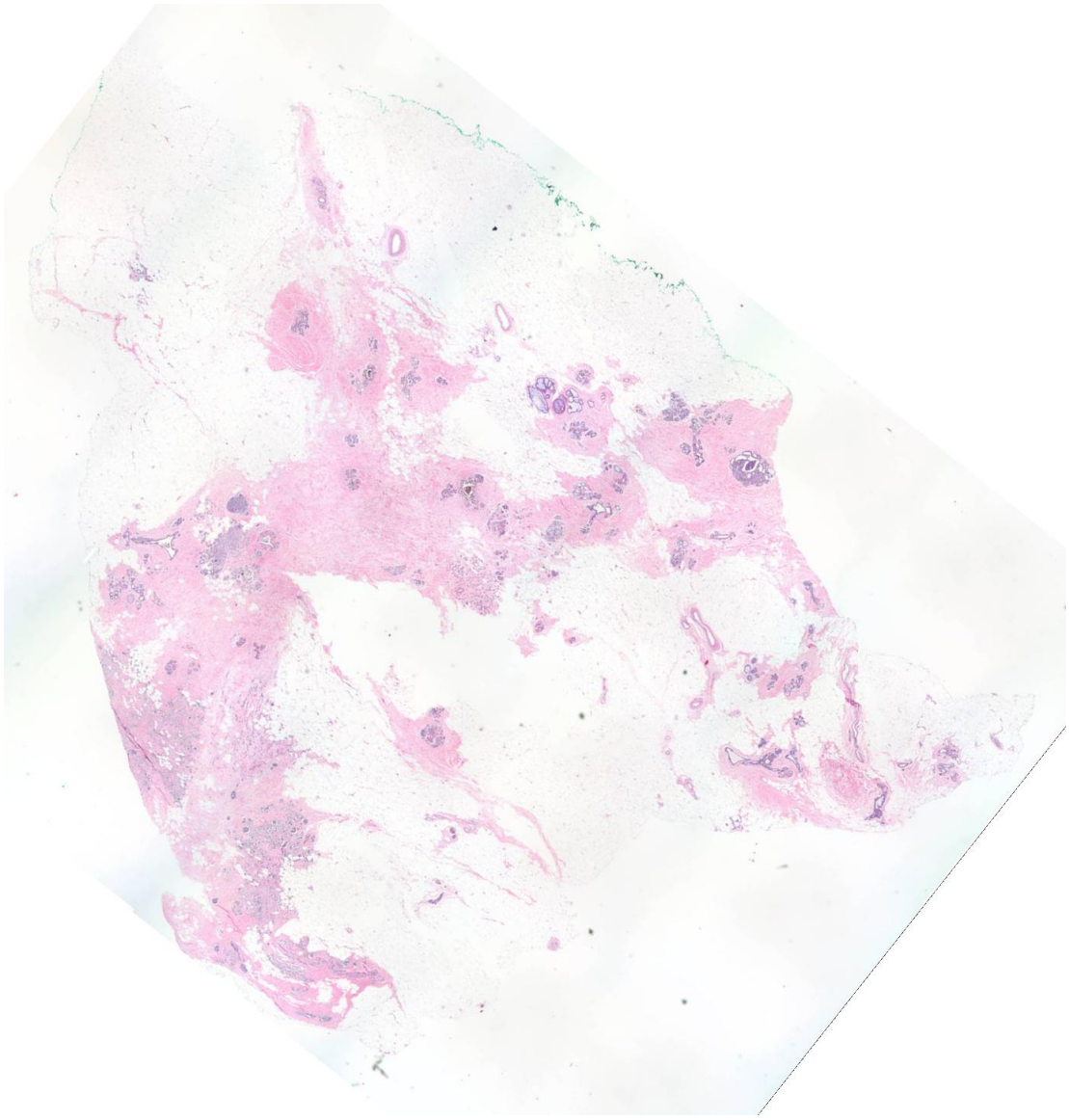

Figure D.4: 8A Marked Histology Slide

Figure D.5: 9A Histology Slide

Figure D.6: 9A Marked Histology Slide

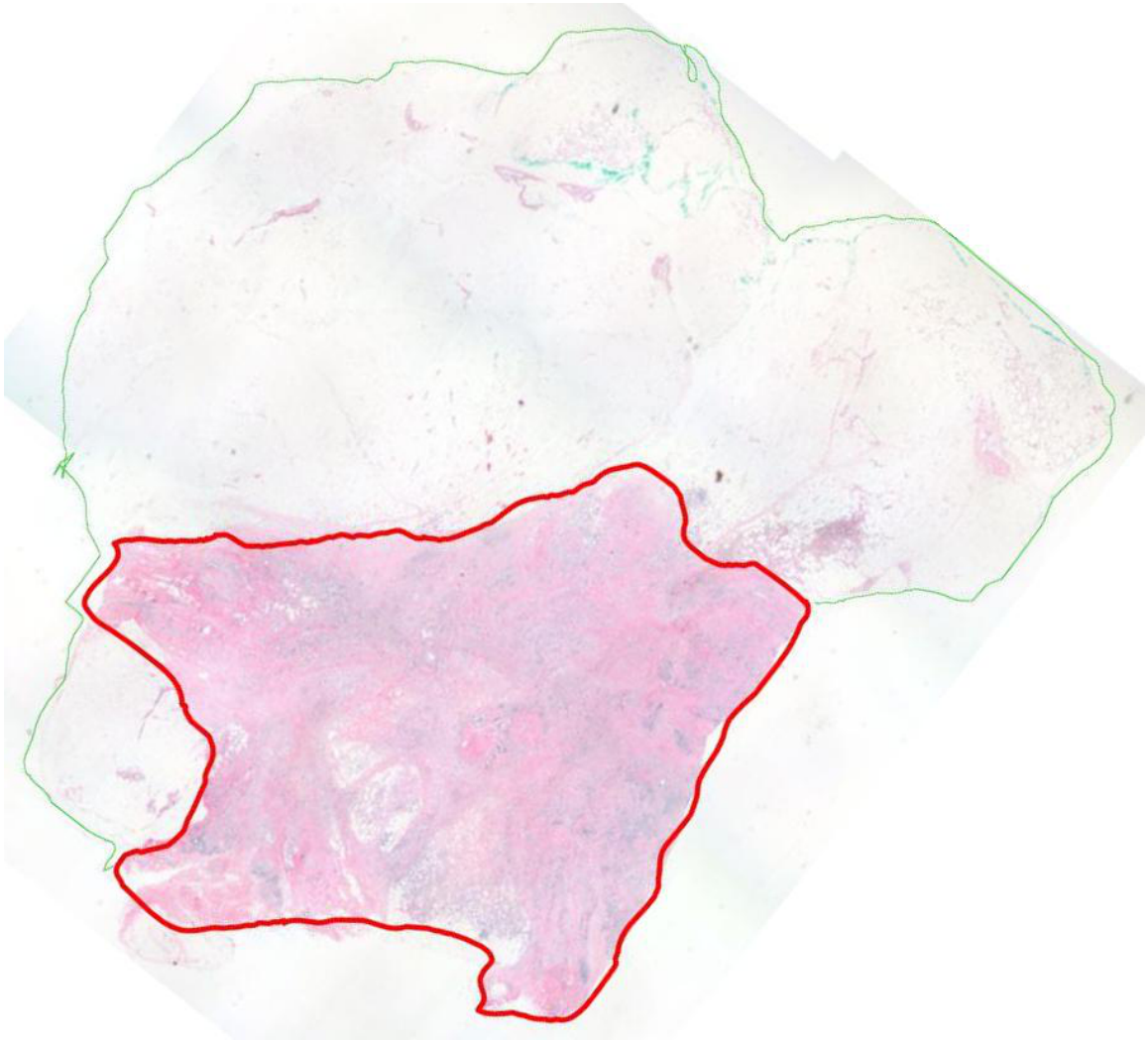

Figure D.7: 10A Histology Slide

Figure D.8: 10A Marked Histology Slide

Figure D.9: 11A Histology Slide

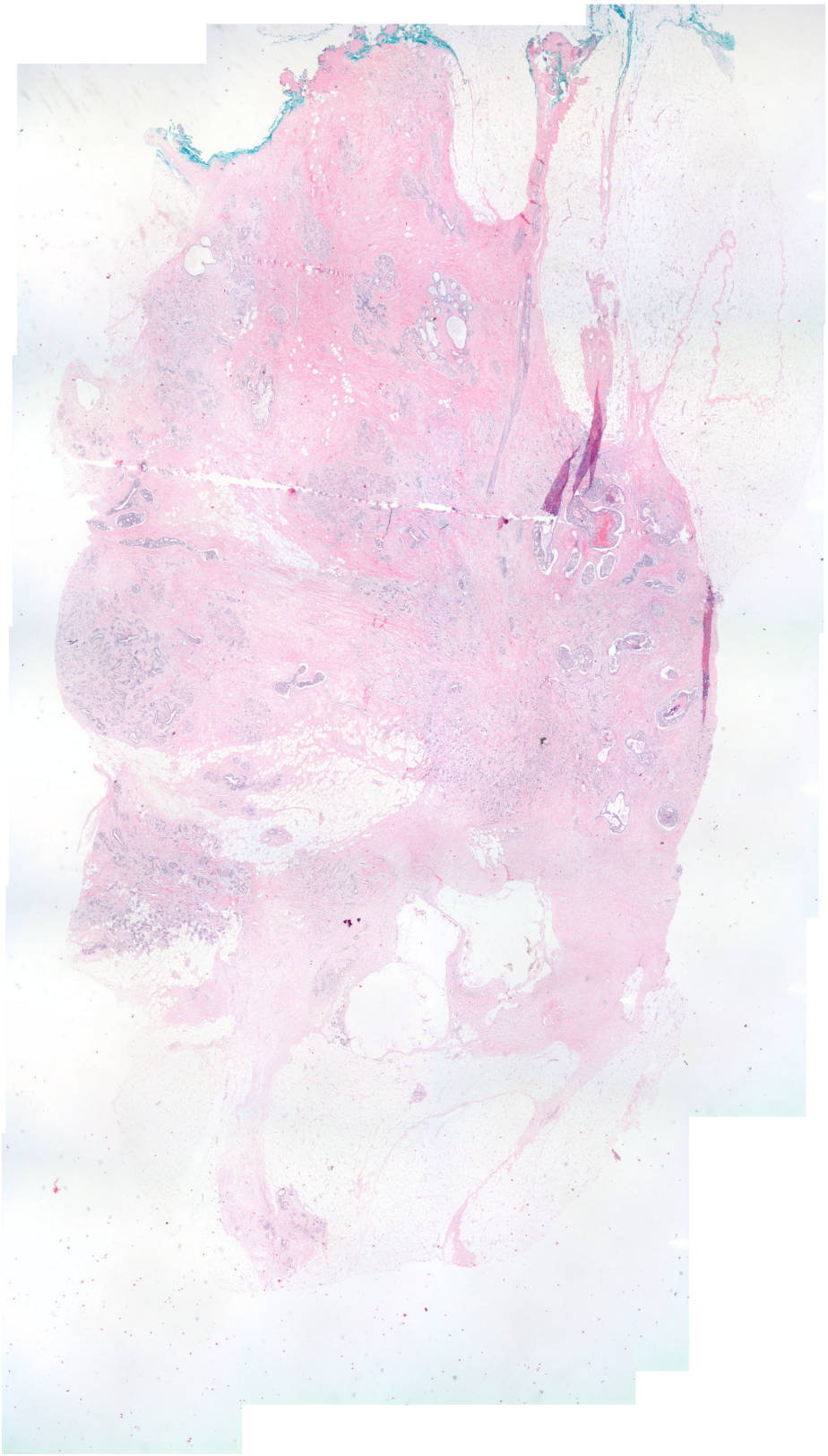

Figure D.10: 11A Marked Histology Slide

Figure D.11: 12A Histology Slide

Figure D.12: 12A Marked Histology Slide

BIBLIOGRAPHY

[APMP+09] Philip C. Ashworth, E. Pickwell-MacPherson, Elena Provenzano, Sarah E. Pinder, Anand D. Purushotham, Michael Pepper, and Vincent P. Wallace. Terahertz pulsed spectroscopy of freshly excised human breast cancer. *Optics Express*, 17(15):12444–12454, July 2009.

[Bel10] Benjamin Bell. Topography and roughness testing of sandpaper surface. *Nanovea Inc*, 2010.

[BG] J. Bruce-Gregorios. *Histopathologic Techniques*. Goodwill Trading Co., Inc.

[BW97] F. Bréhat and B. Wyncke. Measurement of the optical constants of crystal quartz at 10K and 300K in the far infrared spectral range: 10-600 [1/cm]. *International Journal of Infrared and Millimeter Waves*, 18(9), 1997.

[CFSPM12] Yu Calvin, Shuting Fan, Yiwen Sun, and Emma Pickwell-MacPherson. The potential of terahertz imaging for cancer diagnosis: A review of investigations to date. *Quant Imaging Med Surg*, 2:33–45, 2012.

[CMG94] Germán Cortés-Medellín and Paul F. Goldsmith. Analysis of active surface reflector antenna for a large millimeter wave radio telescope. *IEEE Transactions on Antennas and Propagation*, 42(2), February 1994.

[Coo49] J. L. Coolidge. The story of the binomial theorem. *The American Mathematical Monthly*, 56(3):147–157, March 1949.

[Dem03] Wolfgang Demtröder. *Laser Spectroscopy: Basic Concepts and Instrumentation*. Springer, third edition, 2003.

[Dou89] Nigel G. Douglas. *Millimetre and Submillimetre Wavelength Lasers: A Handbook of CW Measurements*. Springer-Verlag, 1989.

[FPP+12] A. Fitzgerald, Sarah Pinder, Anand D. Purushotham, Padraig O'Kelly, Philip C. Ashworth, and Vincent P. Wallace. Classification of terahertz-pulsed imaging data from excised breast tissue. *Journal of Biomedical Optics*, 17(1), January 2012.

[FWJL+06] Anthony J. Fitzgerald, Vincent P. Wallace, Mercedes Jimenez-Linan, Lynda Bobrow, Richard J. Pye, Anand D. Purushotham, and Donald D. Arnone. Terahertz pulsed imaging of human breast tumors. *Radiology*, 239(2):533–540, May 2006.

[GG11] J.M. Gere and B.J. Goodno. *Mechanics of Materials*. Cengage Learning, 2011.

[Gol98] Paul F. Goldsmith. *Quasioptical Systems: Gaussian Beam Quasioptical Propagation and Applications*. IEEE Press, 1998.

[GYN+03] E. Gerecht, S. Yngvesson, J. Nicholson, Y. Zhuang, F. Rodriguez Morales, X. Zhao, D. Gu, R. Zannoni, M. Coulombe, J. Dickinson, T. Goyette, W. Gorveatt, J. Waldman, P. Khosropanah, C. Groppi, A. Hedden, D. Golish, C. Walker, J. Kooi, R. Chamberlin, A. Stark, C. Martin, R. Stupak, N. Tothill, and A. Lane. Deployment of TREND - a low noise receiver user instrument at 1.25THz to 1.5THz for AST/RO at the south pole. *14th Intern. Symp. Space THz Technology, Tucson, Az*, April 2003.

[Har01] Roger F. Harrington. *Time-Harmonic Electromagnetic Fields*. IEEE Press, 2001.

[Hol12] Tom Hollinger. Histological Stains. http://medinfo.ufl.edu/~dental/denhisto/stains.html, 2012.

[Int] IntraAction. *Model AG-406B21 Infrared Acousto-Optic Modulator Instruction Manual*.

[Jac08] Lisa Jacobs. Positive margins: The challenge continues for breast surgeons. *Annals of Surgical Oncology*, 15(5):1271–1272, March 2008.

[JGG09] Arunkumar Jagannathan, Andrew J. Gatesman, and Robert H. Giles. Characterization of roughness parameters of metallic surfaces using terahertz reflection spectra. *Optics Letters*, 34(13):1927–1929, July 2009.

[JMM07] P.U. Jepsen, U. Møller, and H. Merbold. Investigation of aqueous alcohol and sugar solutions with reflection terahertz time-domain spectroscopy. *Optics Express*, 15(22):14717–14737, 2007.

[JMY+00] M. Ji, C. Musante, S. Yngvesson, A.J. Gatesman, and J. Waldman. Study of parylene as anti-reflection coating for silicon optics at THz frequencies. In *Proceedings of the 11th International Symposium on Space Terahertz Technology (ISSTT)*, pages 398–406, Ann Arbor, Michigan, May 2000.

[KSKO+02] P. Knobloch, C. Schildknecht, T. Kleine-Ostmann, M. Koch, S. Hoffmann, M. Hofmann, E. Rehberg, M. Sperling, K. Donhuijsen, and G. Hein. Medical THz imaging: an investigation of histo-pathological samples. *Physics in Medicine and Biology*, 47:3875, 2002.

[Lab11] RIKEN Tera-Photonics Laboratory. Pdc000000887 : Quartz, www.thzdb.org, 2011.

[Mol] Molectron. *P4-30/P4-40 Low Noise Instruments.*

[Mut11] Martin M. Muthee. Terahertz radiation from single walled carbon nanotubes. Master's thesis, The University of Massachusetts Amherst, 2011.

[Nye57] J.F. Nye. *Physical Properties of Crystals: Their Representation by Tensors and Matrices.* Oxford at the Clarendon Press, 1957.

[OPLR09] E. Öjefors, U.R. Pfeiffer, A. Lisauskas, and H.G. Roskos. A 0.65 THz focal-plane array in a quarter-micron CMOS process technology. *IEEE Journal of Solid-State Circuits*, 44(7):1968–1976, July 2009.

[Opt] Almaz Optics. http://www.almazoptics.com/quartz.htm.

[PCN+08] GM Png, JW Choi, B.W.H. Ng, S.P. Mickan, D. Abbott, and XC Zhang. The impact of hydration changes in fresh bio-tissue on THz spectroscopic measurements. *Physics in Medicine and Biology*, 53:3501, 2008.

[PKW+12] Rakesh Patel, Ashraf Khan, Dennis Wirth, Michal Kamionek, Dina Kandil, Robert Quinlan, and Anna N. Yaroslavsky. Multimodal optical imaging for detecting breast cancer. *Journal of Biomedical Optics*, 17(6), June 2012.

[PMLF+07] E. Pickwell-MacPherson, T. Lo, A. Fitzgerald, E. Provenzano, S. Pinder, A. Purushotham, and V.P. Wallace. Application of finite difference time domain methods to terahertz spectroscopy measurements of breast cancer. *IEEE MTT Symp., Honolulu*, pages 1379–1381, 2007.

[Poz05] David M. Pozar. *Microwave Engineering.* John Wiley And Sons, Inc., third edition, 2005.

[Ruz66] John Ruze. Antenna tolerance theory: A review. *Proceedings of the IEEE*, 54(4), April 1966.

[Sie86] Anthony E. Siegman. *Lasers.* University Science Books, 1986.

[SNTT09] Rosalind J. Sadleir, Farida Neralwala, Tang Te, and Aaron Tucker. A controllably anisotropic conductivity or diffusion phantom constructed from isotropic layers. *Annals of Biomedical Engineering*, 37(12):2522–2531, December 2009.

[Sta] Stanford Research Systems. *About Lock-In Amplifiers (Application Note 3).*

[Ula01] Fawwaz T. Ulaby. *Fundamentals of Applied Electromagnetics.* Prentice Hall, media edition, 2001.

[Zha05] Xin Zhao. Integrated antennas for THz hot electron bolometer mixers. Master's thesis, The University of Massachusetts Amherst, 2005.

[ZX09] X.C. Zhang and J. Xu. *Introduction to THz Wave Photonics*. Springer, 2009.